Doctoral Dissertation

博士論文

Nuclear structure at the border of the island of inversion: in-beam γ-ray spectroscopy of ^{30}Mg

（反転の島境界での核構造：^{30}Mgのインビーム核分光）

A Dissertation Submitted for the Degree of Doctor of Philosophy
December 2019

令和元年12月 博士（理学）申請

Department of Physics, Graduate School of Science
The University of Tokyo

東京大学大学院 理学系研究科 物理学専攻

Noritaka Kitamura

北村 徳隆

Abstract

In unstable neutron-rich nuclei, changes in the shell structure and the magic numbers compared to the known structures in the valley of stability have been observed. In the so-called "island of inversion", ground states of neutron-rich sd-shell nuclei are dominated by intruder fp configurations which cannot be explained by the normal filling scheme in the spherical independent-particle shell model. The theoretical modeling of nuclei inside or around this region and identification of the driving forces behind the structural changes have been a formidable challenge for the nuclear theories and of great interest since the discovery of the island of inversion in 1975. In the interacting shell-model approach, the effective reduction of the $N = 20$ shell gap and the promotion of cross-shell excitations are considered to be responsible for these changes, and these are actively discussed in terms of both theory and experiment.

In the present work, the nuclear structure of ^{30}Mg ($N = 18$ and $Z = 12$), lying at the border of the island of inversion, was studied in detail. The main goal of this study is to investigate structural evolution approaching the island of inversion. Therefore, firm spin and parity assignments for excited states are crucial. Prior to this work, levels in ^{30}Mg were studied by γ-ray spectroscopy following β decay of neutron-rich Na isotopes. In-beam γ-ray spectroscopy using the ^{14}C(^{18}O,2p) fusion-evaporation reaction and the one-neutron knockout reaction from ^{31}Mg was also reported. These studies indicated the presence of negative-parity states lying significantly lower in excitation energy than predicted by shell-model calculations. As the negative-parity states are formed by cross-shell excitations, the excitation energies of these states are related to the effective size of the $N = 20$ gap. These experimental results were interpreted as the structural change taking place in a wider region than previously thought, and posed questions concerning the theoretical description of ^{30}Mg.

To establish the spin and parity of the levels, including candidates for negative-parity states, in-beam γ-ray spectroscopy of ^{30}Mg was performed at the National Superconducting Cyclotron Laboratory at Michigan State University. Radioactive beams of ^{31}Mg, ^{32}Mg, ^{34}Si, and ^{35}P were produced by projectile fragmentation reactions of an intense ^{48}Ca primary beam. The radioactive beams were directed onto a reaction target to induce nucleon removal reactions populating states in ^{30}Mg. The γ rays emitted from excited states were detected by the γ-ray tracking array GRETINA in coincidence with residual ^{30}Mg nuclei identified by the S800 spectrograph. The high statistics were in particular beneficial for a γ-γ coincidence analysis, allowing for the construction of an updated level scheme. In the one-neutron knockout reaction from ^{31}Mg, the parallel momentum distribution of the reaction residue provided indications for the angular momentum of the removed neutron and thus the spin-parity assignments of states.

The location of the negative-parity states was firmly established for the first time. It was found that the lowest negative-parity state in ^{30}Mg lies at 3.3 MeV. Other negative-parity states were observed at 3.5 MeV and above. A state at 2.5 MeV, previously interpreted as a candidate for a negative-parity state, was assigned as a positive-parity state. With the new ^{30}Mg level

scheme obtained in this work, the drop of the excitation energy of the negative-parity states when going from Si ($Z = 14$) to Mg ($Z = 12$) was confirmed. Even though the drop is not as steep as those proposed in previous studies, this is interpreted as a manifestation of the reduction of the $N = 20$ gap and thus a precursory structural change approaching the island of inversion. Spectroscopic factors were obtained from the one-neutron knockout reaction from ^{31}Mg. The spectroscopic factors for populating the negative-parity states in ^{30}Mg were found to be large. In particular, the neutron knockout from the $p_{3/2}$ orbital showed significant spectroscopic factors. This corroborates the intruder-dominated configuration in the ground state of ^{31}Mg.

To get more insight into the nuclear structure of ^{30}Mg, the experimental level scheme and spectroscopic factors were compared with large-scale shell-model calculations. The level structure was remarkably well reproduced by the calculations without much sensitivity to the shell-model interactions, providing a benchmark towards future spectroscopic studies in this region. On the other hand, none of calculations succeeded in reproducing the spectroscopic factors for all states. These findings imply that the transition into the island of inversion is not yet fully captured in the present shell-model calculations, posing a further challenge to nuclear theories towards the complete description of this region.

Contents

Chapter 1

Introduction

1.1 Magic numbers

One of the most fundamental concepts in nuclear physics is the existence of magic numbers. The origin of this concept dates back to the 1930s; Elsasser remarked on special numbers of neutrons and protons where atomic nuclei acquire particular stability [1]. Experimentally, several observables are used to speak of magicity and thus a shell closure [2]. The two-neutron separation energy, which is the energy required to remove two neutrons from a nucleus, is defined based on nuclear masses. This observable provides hints for a shell closure, because the closed-shell nuclei are more bound (see Figure 1.1). The excitation energy of the first 2^+ state, $E(2^+)$, in even-even nuclei is another example. A high $E(2^+)$ is associated with particular stability or the "stiffness", as excitation from the ground state involves large energy gaps (see Figure 1.2), The reduced electromagnetic transition strength between the ground state and the first 2^+ state, $B(E2; 0_1^+ \rightarrow 2_1^+)$, in even-even nuclei is a direct measure of the nuclear collectivity that quantifies the motion of many nucleons, and this can also be used to discuss a shell closure. With a certain assumption, $B(E2)$ can be related to the nuclear deformation. A small $B(E2)$ means a small collectivity and sphericity, and provides an additional indication of a shell closure.

Attempts to microscopically explain the existence of the magic numbers have been made since the 1940s. The first successful approach was the independent-particle shell model. In this model, instead of treating nuclear forces acting between nucleons explicitly, a mean-field potential is assumed to be generated by all nucleons constituting the nucleus and each nucleon is allowed to independently move inside the potential. In the simplest approach, a harmonic oscillator

$$V(r) = \frac{1}{2} m\omega^2 r^2 \tag{1.1}$$

can be used to mimic the one-body mean-field potential. By solving the one-body Schrödinger equation, shell structure and levels characterized by the quantum numbers n, l, and m appear. To make the mean-field potential more realistic, one may assume a Woods-Saxon potential of the form

$$V(r) = -V_0 f_{\mathrm{WS}}(r) \tag{1.2}$$

where

$$f_{\mathrm{WS}}(r) = \frac{1}{1 + e^{(r-r_0)/a_0}}. \tag{1.3}$$

Usually, the potential depth V_0 is set to about 50 MeV, the radius r_0 is parameterized by

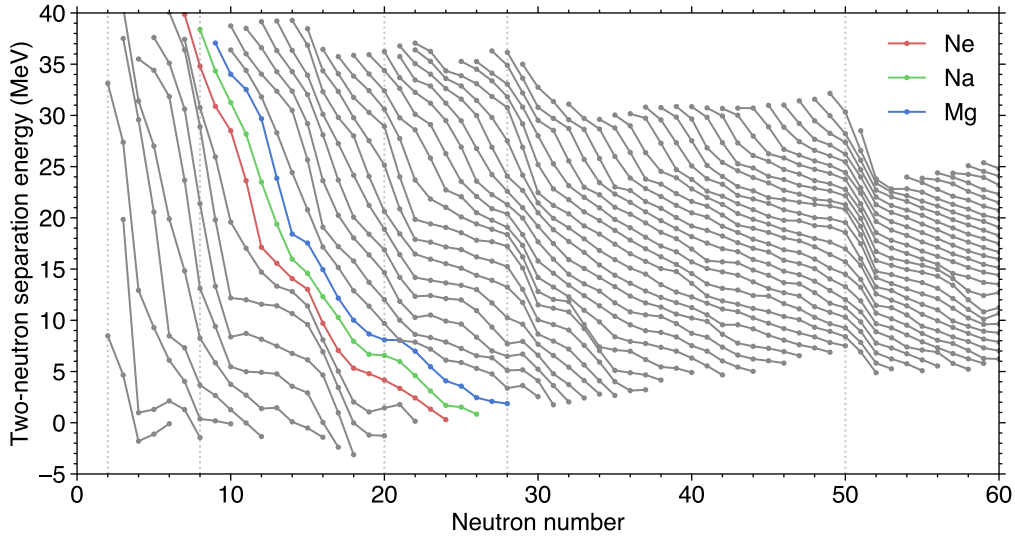

Figure 1.1: Two-neutron separation energies S_{2n}. Ne, Na, and Mg isotopes are highlighted. Data taken from the Atomic Mass Evaluation 2016 [3].

$1.2A^{1/3}$ fm, and the diffuseness a_0 is typically 0.7 fm. In this case, the degeneracy with respect to the principal quantum number is removed, but only the magic numbers up to $N = 20$ are reproduced. In 1949, Mayer and Jensen introduced a phenomenological spin-orbit interaction acting on nucleons residing in a potential well, and they successfully reproduced known magic numbers, 2, 8, 20, 28, 50, 82, and 126 [5,6]. The total potential has the form

$$V(r) = -V_0 f_{\mathrm{WS}}(r) + (\boldsymbol{l} \cdot \boldsymbol{s}) V_{ls} \frac{d}{dr} f_{\mathrm{WS}}(r) \tag{1.4}$$

where V_{ls} is the spin-orbit strength. This expression means that the potential depends on the relative orientation of the orbital angular momentum $\boldsymbol{l}$ and the spin $\boldsymbol{s}$ of the nucleon. The orbital angular momentum and the spin can be coupled to give the total angular momentum of $j_> = l + 1/2$ or $j_< = l - 1/2$ according to the triangle relation. As can be seen in Figure 1.3, the levels with the same l are split into two different energies depending on the total angular momentum. The magic numbers established in studies of stable nuclei are well reproduced by this model.

Figure 1.2 visualizes magic numbers through the excitation energies of 2_1^+ states. Nuclei with magic numbers and particularly doubly-magic ones, ^{40}Ca as an example, stand out in the plot. With the advent of facilities that provide radioactive ion beams, unstable nuclei far away from stability have been studied during the last four decades. In the course of such studies, it has been revealed that the classical magic numbers and level structure can be altered when going away from the β-stability line, and this has become an established notion [7]. For instance, the disappearance of the magic number at $N = 8$ around ^{12}Be [8,9], the weakening of the $N = 28$ gap around ^{42}Si [10], and the emergence of a new magic number at $N = 16$ in ^{24}O [11] have been reported. Among them, the collapse of the shell gap at $N = 20$, which is detailed in the next section, is an archetypical example of structural changes taking place in unstable nuclei.

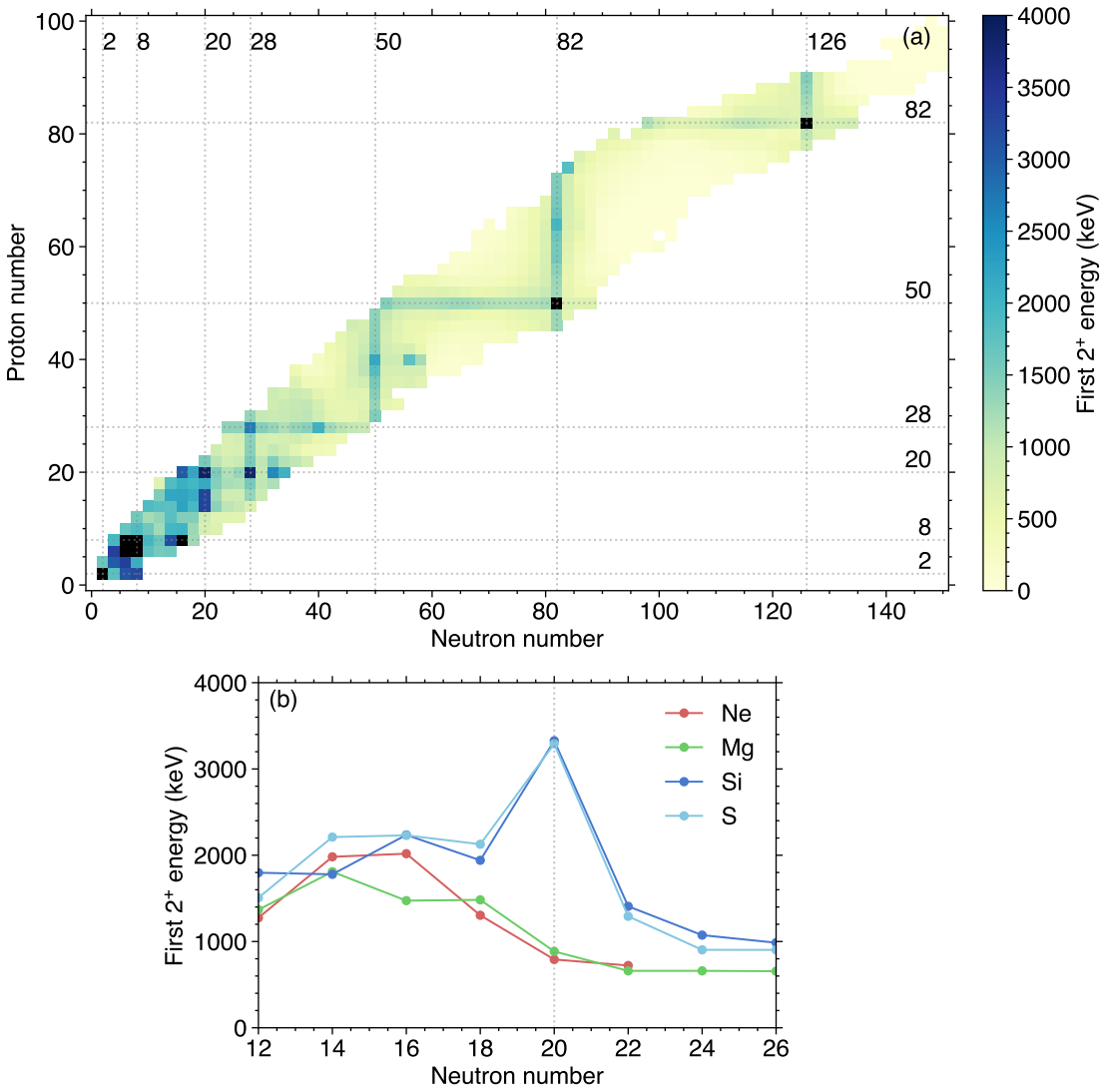

Figure 1.2: (a) Systematics of the first excited 2^+ energies as a function of proton and neutron numbers. (b) One-dimensional projection around the island of inversion. Data taken from the latest ENSDF database [4].

1.2 The island of inversion

It was observed that unexpected sudden changes of nuclear structure take place in the unstable neutron-rich nuclei around $N = 20$ [7]. This finding implied that nucleon-nucleon correlations, which are not present in the independent-particle shell model, play a pivotal role in changing the nuclear shell structure. Before going into theoretical details, a review of the structural changes around $N = 20$ is presented below.

First, anomalies in the biding energies, namely masses, of the neutron-rich Na isotopes were found in the pioneering work of Klapisch and Thibault [15, 16]. The authors measured nuclear masses of $^{27-32}$Na and revealed that ^{31,32}Na are more bound than expected (see Figure 1.1). Mass measurements were extended to neutron-rich Mg and Ne isotopes around $N = 20$, and the anomalous binding energies were also found [17, 18]. β-delayed γ-ray spectroscopy of ^{32}Mg

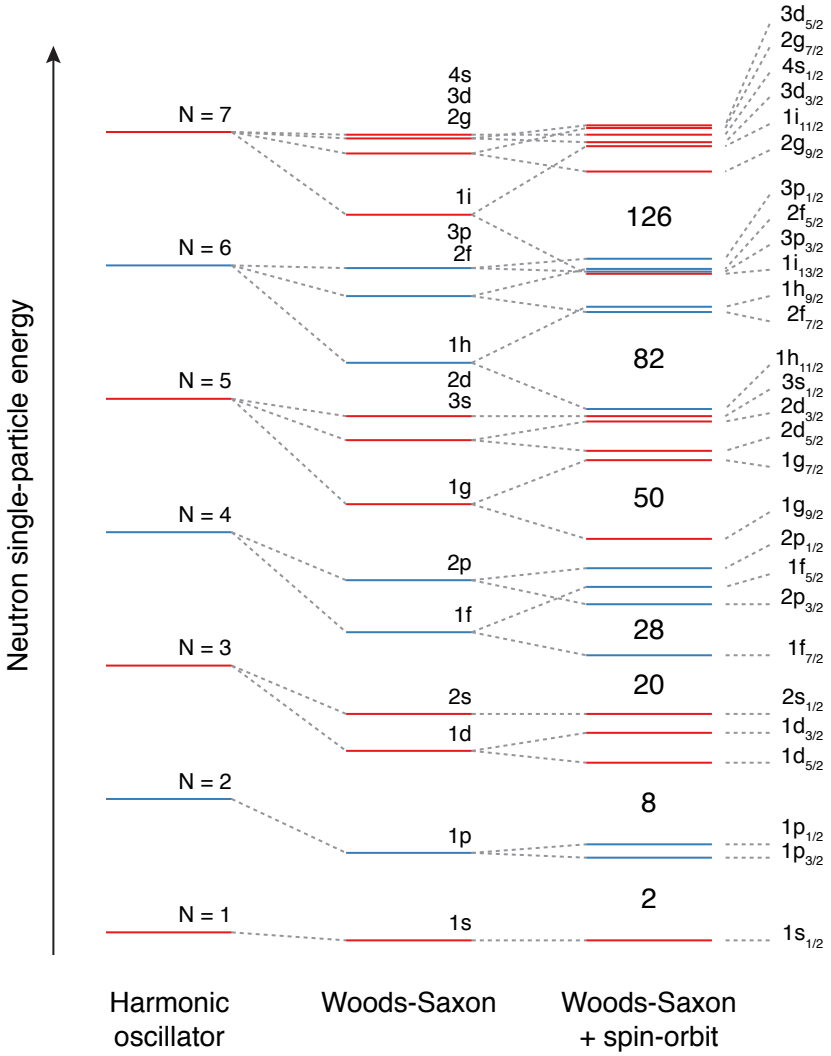

Figure 1.3: Schematic illustration of single-particle energies in harmonic oscillator, Woods-Saxon, and Woods-Saxon plus spin-orbit potentials for neutrons in ^{208}Pb. Positive- (negative-) parity orbitals are represented by red (blue) horizontal lines. Note that the ordering of single-particle orbitals (sub-shells) within a major shell can be slightly altered in different mass regions depending on the parameters of the Woods-Saxon and spin-orbit potentials.

showed that the first 2^+ state lies at a very low excitation energy of 885 keV and provided a clear indication of deformation [19]. Low excitation energies of the first 2^+ state were also found in ^{34}Mg [20], ^{30}Ne [21] and so on (see Figure 1.2). Additionally, a $B(E2; 0^+_1 \rightarrow 2^+_1)$ value for ^{32}Mg measured by Motobayashi *et al.* [22] put the anomalously high collectivity of ^{32}Mg and thus the strong deformation on a firm footing.

Theoretically, constrained Hartree-Fock calculations [23] showed that the unusual flattening in the two-neutron separation energies of the Na isotopes at the magic number can be traced back to nuclear deformation. From the viewpoint of the shell model (see also Section 1.3), Wildental and Chung showed that the binding energies of Na and Mg at $N = 20$ cannot be reproduced by calculations with a *sd*-shell model space only [24]. Shell-model calculations

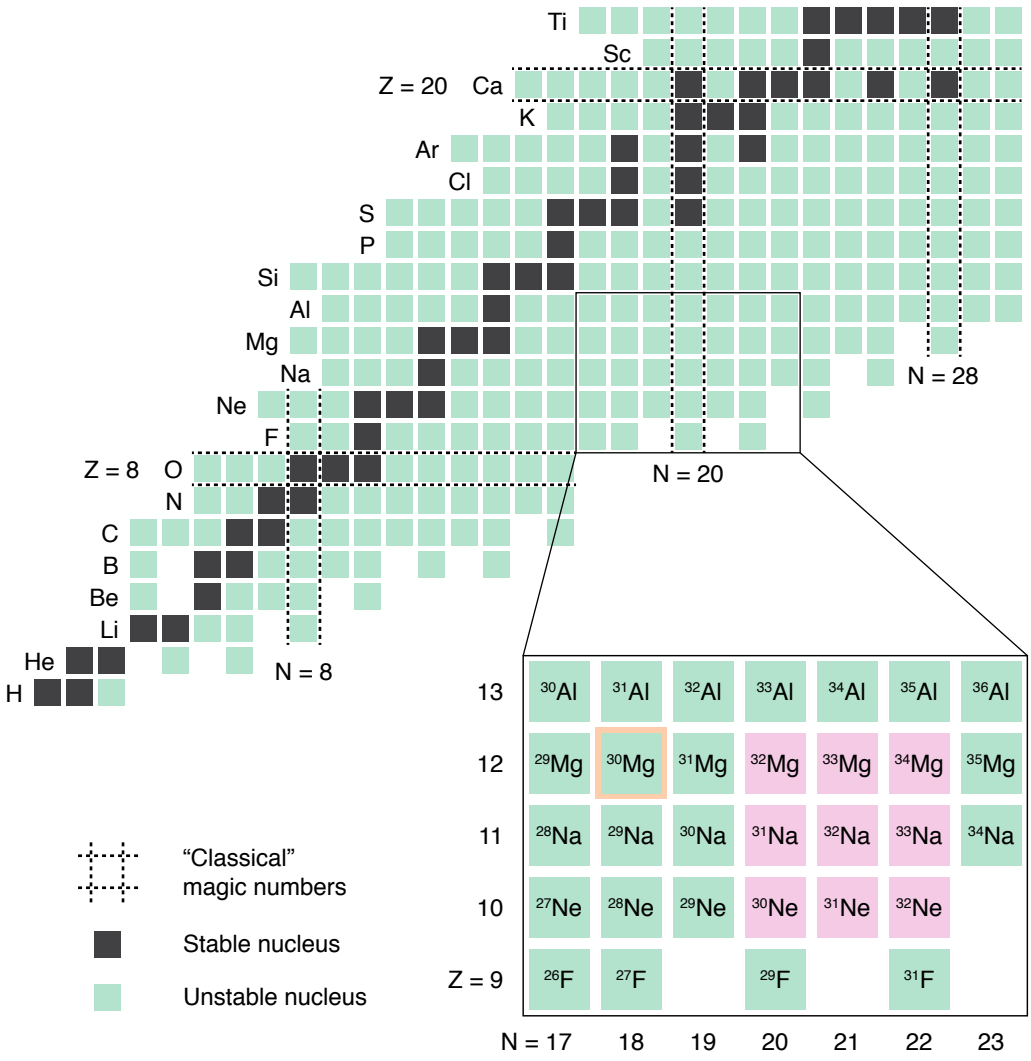

Figure 1.4: Partial nuclear chart from hydrogen ($Z = 1$) to titanium ($Z = 22$). Black and green boxes denote stable and unstable nuclides, respectively. The traditional magic numbers are also indicated. The original island of inversion proposed by Warburton *et al.* [12] is highlighted in the inset. Note that the island has extended further up to now [13]. The nucleus of interest in this work, ^{30}Mg, is also highlighted. Note that ^{31}Mg, in which one neutron is knocked out to populate states in ^{30}Mg, is now considered to be located exactly at the boundary of the island of inversion [14].

with an extended model space incorporating a part of the fp shell, which lies above the $N = 20$ gap, were performed by Warburton *et al.* [12]. The main finding was that the excitations across the $N = 20$ gap, or the two-particle-two-hole (2p2h) excitations, play a pivotal role in reproducing the existence of this anomalous region. Thus, this region was named the "island of inversion". Since the ground states of these nuclei are characterized by configurations involving higher-lying orbitals which are reduced in excitation energy due to the residual interaction, such states are said to be dominated by "intruder" configurations. In Figure 1.4, part of the nuclear chart is shown together with the island of inversion originally proposed by Warburton *et al.* [12]. In this region, the ground states are thought to be dominated by intruder configurations which are energetically favored, while the nuclei outside the island are characterized by normal configurations. Schematic illustrations of normal and intruder configurations are shown in Figure 1.5.

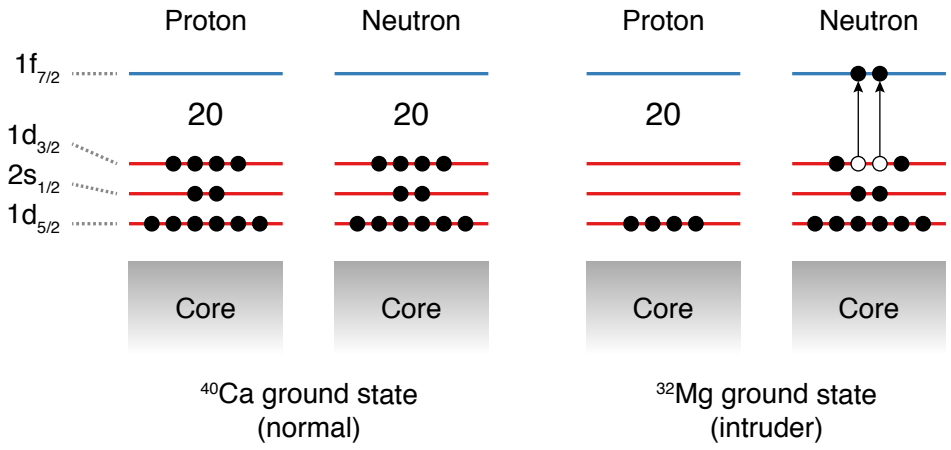

Figure 1.5: Simplified illustration of proton and neutron configurations in ^{40}Ca ($N = 20$ and $Z = 20$) and ^{32}Mg ($N = 20$ and $Z = 12$). The ground state of ^{40}Ca is characterized by shell closures of the proton and neutron sides, leading to the doubly-magic nature of this nucleus. Valance neutrons in the ground state of ^{32}Mg are excited across the $N = 20$ gap, resulting in the disappearance of magicity. For simplicity, a pure 2p2h excitation formed by promoting two neutrons from the $1d_{3/2}$ orbital to $1f_{7/2}$ is illustrated in this figure. The neutrons can also be promoted from the $1d_{5/2}$ and $2s_{1/2}$ orbitals. The $2p_{3/2}$ orbital located just above $1f_{7/2}$ is not shown, but this orbital also plays a role in the formation of cross-shell excitations.

Experimental studies to track the evolution of nuclear structure are now being extended to other nuclei around, or even beyond the original island of inversion. For the Mg isotopes, the properties of the ground state of ^{31}Mg ($N = 19$) were investigated by combining hyperfine-structure and β-NMR measurements in 2005 [14]. The ground-state spin-parity was determined to be $1/2^+$ for the first time, and it was suggested that this state is strongly prolate deformed and dominated by an intruder configuration. From these findings, ^{31}Mg was placed exactly on the border of the island of inversion. The onset of intruder configurations in Mg isotopes was also investigated by in-beam γ-ray spectroscopy. The one-neutron knockout reactions on ^{30}Mg and ^{32}Mg populating states in ^{29}Mg and ^{31}Mg were measured [25]. Negative-parity states were identified in these nuclei, and spectroscopic factors for the $1f_{7/2}$ and $2p_{3/2}$ orbitals were deduced. It was observed that the strength associated with the pf shell suddenly increases at $N = 20$ as compared to $N = 18$. A large spectroscopic factor means a significant occupation

of the corresponding orbital. Therefore, this experimental result is interpreted as a dramatic structural change occurring in between $N = 20$ and 18.

Another important aspect of the island of inversion is shape coexistence where nuclei exhibit different shapes coexisting in near degenerate states. Shape coexistence is considered to be driven by the delicate balance between two opposing ingredients: one is residual interactions that invoke deformed configurations consisting of many particle-hole excitations and the other is shell closures that favor sphericity. Shape coexistence has been extensively studied in various mass regions [26], and nowadays the region around ^{32}Mg is considered to be a monumental example of shape coexistence. In fact, evidence for spherical-prolate shape coexistence has been found in ^{30}Mg [27], ^{32}Mg [28], and ^{34}Si [29]. The first two cases are detailed in Section 1.4.1.

1.3 Shell-model approach to the island of inversion

As reviewed in the previous sections, changes in shell structure as a function of proton or neutron number in unstable nuclei have been observed. These are called shell evolution in the context of the interacting shell model. The primary goal of this section is to present the basics of the interacting shell model and the description of the shell evolution with a special emphasis on the island of inversion.

In the interacting shell model, a nucleus is described as composed of an inert core and active nucleons moving in orbitals in the valence space interacting with each other. The nuclear wave function is expressed as a superposition of configurations, namely many-body Slater determinants. This approach is also called configuration interaction in the context of atomic physics or quantum chemistry. For simplicity, the interacting shell model is often referred to as just the shell model.

The shell-model Hamiltonian in the second quantized form takes the form

$$H = \sum_i \epsilon_i a_i^\dagger a_i + \frac{1}{4} \sum_{ijkl} V_{ijkl} a_i^\dagger a_j^\dagger a_l a_k, \tag{1.5}$$

where $a_i^\dagger$ and a_i are the creation and annihilation operators of a nucleon in a single-particle orbital i. Here, the input parameters are the Single-Particle Energies (SPEs) ϵ_i and the two-body interaction V_{ijkl}, the Two-Body Matrix Elements (TBMEs). Usually, the single-particle energies are determined such that experimental excitation energies of systems with one nucleon outside a doubly-magic core are reproduced.

In principle, the diagonalization of the shell-model Hamiltonian of the many-body states gives the eigenenergies and the wave functions. In the M-scheme, the many-body wave function $|\Phi\rangle$ is represented by a linear combination

$$|\Phi\rangle = \sum_i v_i \, |M_i\rangle \tag{1.6}$$

where $|M_i\rangle$ is a many-body Slater determinant written as

$$|M_i\rangle = a_{b_i,1}^\dagger a_{b_i,2}^\dagger \cdots a_{b_i,A}^\dagger \, |0\rangle \, . \tag{1.7}$$

Here, A stands for the number of active orbitals and $|0\rangle$ represents the inert core. By solving the eigenvalue problem in a matrix representation

$$\sum_j \langle M_i|H|M_j\rangle \, v_j = E v_i \tag{1.8}$$

the eigenvector v_i and the eigenenergy E are obtained. The actual computation is performed with a fast algorithm of matrix diagonalization, such as the Lanczos method. Note that when the model space is expanded the exact diagonalization becomes quickly intractable, so that the shell-model calculations can only be performed with a truncation of the model space or excitations. For instance, an inert core of ^{16}O ($N, Z = 8$) and active orbitals of the full sd shell, i.e. $1d_{5/2}$, $2s_{1/2}$, and $1d_{3/2}$ orbitals, are the standard model space for shell-model calculations of sd-shell nuclei. Owing to the increased computational power, it has become possible to perform shell-model calculations with an extended model space. For the theoretical description of the island of inversion in the shell-model framework, an extended model space including neutron fp-shell orbitals, such as $1f_{7/2}$ and $2p_{3/2}$, was found to be an essential ingredient [12]. Even though a truncation in the number of cross-shell excitations ($n\hbar\omega$ truncation) is required, shell-model calculations involving the full sd and pf shells are now feasible.

1.3.1 Monopole effects

As a driving force of the shell evolution, the effects of different components of the nucleon-nucleon interaction in the medium have been widely discussed [7, 30]. In order to describe the shell evolution, the angle-averaged component, or the monopole component, of the two-body shell-model interaction is first considered. For two nucleons in orbitals i and j with quantum numbers $i = (n_i, l_i, j_i)$ and $j = (n_j, l_j, j_j)$, the monopole interaction is defined as

$$\bar{V}_{ij}^{\rho\rho'} = \frac{\sum_J (2J+1) \langle ij; JM|V|ij; JM\rangle}{\sum_J (2J+1)} \tag{1.9}$$

where ρ and ρ' stand for π (proton) or ν (neutron), and the sum runs over all allowed J values. $|ij; JM\rangle$ means that the two nucleons in i and j are coupled to angular momentum J with projection M. The Hamiltonian for the monopole component is given by

$$\hat{H}_{\mathrm{mon}} = \sum_i \epsilon_i^\nu \hat{N}_i^\nu + \sum_i \epsilon_i^\pi \hat{N}_i^\pi + \sum_{ij} \bar{V}_{ij}^{\nu\pi} \hat{N}_i^\nu \hat{N}_j^\pi + \sum_{i\le j} \bar{V}_{ij}^{\nu\nu} \frac{\hat{N}_i^\nu (\hat{N}_j^\nu - \delta_{ij})}{1+\delta_{ij}} + \sum_{i\le j} \bar{V}_{ij}^{\pi\pi} \frac{\hat{N}_i^\pi (\hat{N}_j^\pi - \delta_{ij})}{1+\delta_{ij}} \tag{1.10}$$

where ϵ_i^ρ is the bare single-particle energy, $\hat{N}_i^\pi$ ($\hat{N}_i^\nu$) is the proton (neutron) occupation number, and δ is Kronecker delta. In Equation (1.10), one notices that the energy of the monopole part changes as a function of number of neutrons and protons. From this monopole Hamiltonian, the single-particle energy including the monopole effect can be defined [31]. This is called the effective single-particle energy (ESPE). Figure 1.6 shows effective single-particle energies derived from the SDPF-M interaction for $N = 20$. A reduction of the $N = 20$ gap is seen below Si ($Z = 14$).

Effects of the central force

In 2001, Otsuka *et al.* suggested the particular importance of the spin-isospin-dependent interaction in the shell evolution [33]. The spin-isospin central component of the nuclear force has the form

$$V_{\sigma\sigma\tau\tau} = (\sigma_1 \cdot \sigma_2)(\tau_1 \cdot \tau_2) f(r) \tag{1.11}$$

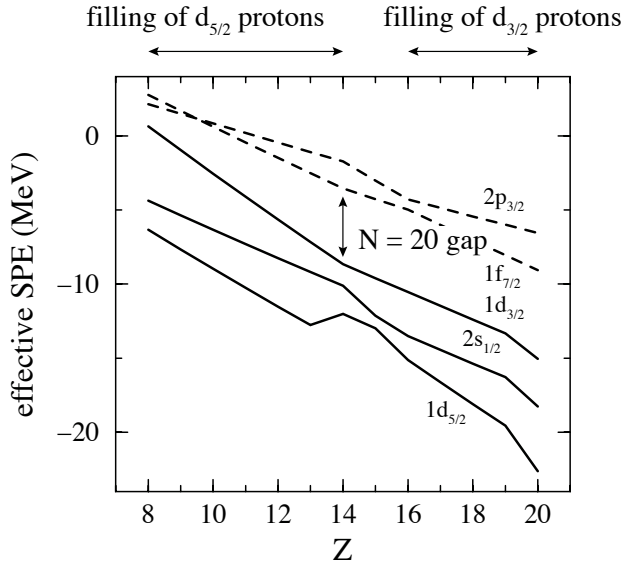

Figure 1.6: Evolution of effective single-particle energies for $N = 20$ isotopes calculated with the SDPF-M interaction. The reduction of the $N = 20$ gap between the $1d_{3/2}$ and $1f_{7/2}$ orbitals is seen below ^{34}Si ($Z = 14$). This is driven by the removal of protons from the $1d_{5/2}$ orbital. Taken from [32] with modifications.

where σ and τ are respectively spin and isospin operators, and $f(r)$ represents the relative-distance dependence. The numbers 1 and 2 label the two nucleons. The monopole interaction originating from this spin-isospin central force gives rise to attractive matrix elements between $l + 1/2$ and $l - 1/2$ orbitals. This notion has been applied to explain the appearance of the new shell gap at $N = 16$ in ^{24}O ($Z = 8$).

Effects of the tensor force

In 2005, Otsuka *et al.* also suggested that the tensor component of the nuclear force is also essential in explaining the shell evolution in addition to the contribution from the central force [34]. The origin of the long-range part of the bare nuclear force between two nucleons, i.e. outside the region of the repulsive core, is explained by the exchange of pions, and the corresponding potential has the form [32]

$$V_\pi(r) = f_\pi(\tau_1 \cdot \tau_2)(\sigma_1 \cdot \nabla_1)(\sigma_2 \cdot \nabla_2)\frac{e^{-m_\pi r}}{r} \tag{1.12}$$

where f_π is the coupling parameter, and $m_\pi \approx 140\,\mathrm{MeV}/c^2$ is the pion mass. This can also be written as the sum of scalar and tensor parts as

$$V_\pi(r) = \frac{f_\pi m_\pi^2}{3}(\tau_1 \cdot \tau_2)\left[(\sigma_1 \cdot \sigma_2)\left(\frac{e^{-m_\pi r}}{r} - \frac{4\pi}{3}\delta^3(r)\right) + S_{12}\left(\frac{1}{r} + \frac{3}{m_\pi r} + \frac{3}{(m_\pi r)^2}\right)\frac{e^{-m_\pi r}}{r}\right] \tag{1.13}$$

where the tensor operator S_{12} is defined as

$$S_{12} = (\sigma_1 \cdot \boldsymbol{r})(\sigma_2 \cdot \boldsymbol{r}) - \frac{1}{3}\sigma_1 \cdot \sigma_2 = \sqrt{24\pi}[\sigma_1, \sigma_2]^{(2)} \cdot Y^{(2)}. \tag{1.14}$$

In the last expression, σ_1 and σ_2 are coupled to form a tensor of rank-2 (the number in parentheses indicates the rank), and the scaler product of this rank-2 tensor and the rank-2 spherical harmonic $Y^{(2)}$ is taken. It has been shown that the tensor component of the nuclear force is persistent in the medium [34], and it also plays an important role in the evolution of shells. In general, the tensor force can be written as

$$V_{\text{tensor}} = (\tau_1 \cdot \tau_2) S_{12} f_{\text{tensor}}(r) \tag{1.15}$$

where $f_{\text{tensor}}(r)$ represents the dependence on the relative distance r of two nucleons.

By setting $a = j_< = l - 1/2$ and $b = j_> = l + 1/2$ in Equation (1.9), it can be shown that $\bar{V}_{j_< j'_>}$ and $\bar{V}_{j_> j'_<}$ are attractive, $\bar{V}_{j_< j'_<}$ and $\bar{V}_{j_> j'_>}$ are repulsive for the tensor force. This is one of the most important features of the monopole component originating from the tensor force. The effects of the tensor force are schematically shown in Figure 1.7. Another important feature worth noting is that the following sum rule holds:

$$(2j_< + 1)\bar{V}^{\pi\nu}_{j_< j'} + (2j_> + 1)\bar{V}^{\pi\nu}_{j_> j'} = 0 \tag{1.16}$$

where j' can be either $j'_<$ or $j'_>$. This sum rule implies that the net effect of the monopole component cancels when $j_<$ and $j_>$ are fully occupied. Conversely, in the situation where one of the two orbitals is completely empty and the other is fully occupied, the effect of the monopole component is maximized.

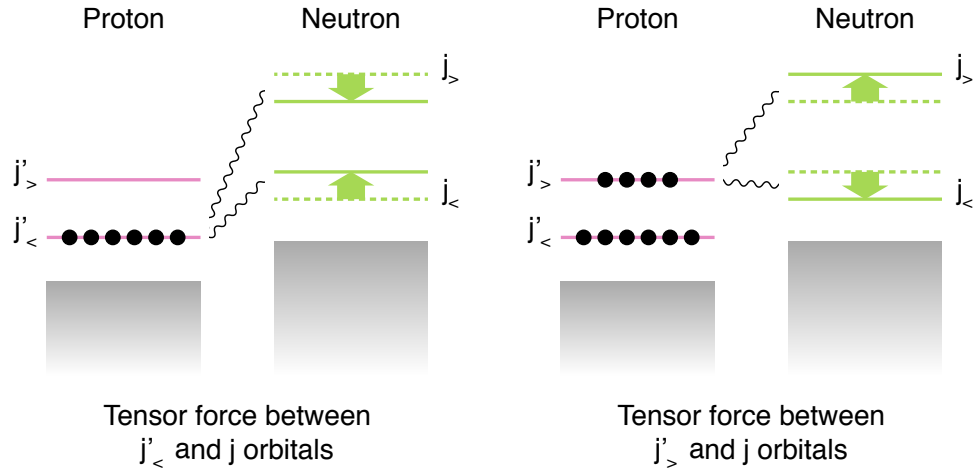

Figure 1.7: Effects of the monopole interaction originating from the tensor force acting between a neutron in $j_{>,<} = l \pm 1/2$ and a proton in $j'_{>,<} = l' \pm 1/2$.

The shell evolution along the $N = 20$ chain is described by the cooperative effects due to the central and tensor components in the monopole interaction. In the stable nucleus ^{40}Ca ($Z = 20$), the neutron $1d_{3/2}$ orbital is lowered with respect to the remainder of the sd shell and the $N = 20$ gap is created as proton $1d_{5/2}$ and $1d_{3/2}$ are both fully occupied. Starting after ^{34}Si ($Z = 14$), protons are removed from the $1d_{5/2}$ orbital, and then the coupling to the neutron $1d_{3/2}$ orbital is weakened. This leads to an increased slope of the effective single-particle energy for $1d_{3/2}$ as a function of decreasing Z. In ^{32}Mg and ^{30}Ne ($Z = 12$ and $Z = 10$), the neutron $1d_{3/2}$ and $1f_{7/2}$ orbitals come closer in energy, and thus the $N = 20$ gap is reduced. This reduction

leads to particle-hole excitations that enhance quadrupole deformation and pairing correlations, and results in low-lying collective excitations and well-deformed ground states, triggering the appearance of the island of inversion.

1.3.2 Shell-model interactions

With the increase in computational power, it became possible to fit TBME and SPE to reproduce experimental observables. The universal *sd*-shell interaction, or USD, developed by Wildenthal and Brown is a standard interaction of this approach [35, 36]. Although the direct connection to the nucleon-nucleon interactions is not (fully) preserved, this interaction can reproduce experimental energy levels of *sd*-shell nuclei very well, and the accuracy is even better than effective interactions based on the nucleon-nucleon interactions.

As already pointed out by Warburton *et al.* [12], for the shell-model description of island-of-inversion nuclei, the inclusion of the *fp*-shell is indispensable. In 1999, Utsuno *et al.* developed a new interaction [37] that incorporates the neutron $1f_{7/2}$ and $2p_{3/2}$ orbitals in addition to the full *sd* shell ($1d_{5/2}$, $2s_{1/2}$, and $1d_{3/2}$) for neutrons and protons outside a ^{16}O core. The *sd*-shell part is identical to the USD interaction. The *pf*-shell part is taken from the Kuo-Brown interaction, which is obtained from the renormalized *G* matrix [38]. The cross-shell part is constructed based on the Millener-Kurath interaction with phenomenological adjustments [39]. The reduction of the $N = 20$ shell gap below $Z = 14$ could be explained by this interaction, as can be seen in Figure 1.6.

The SDPF-M interaction has been traditionally used and tested for nuclei in and around the island of inversion. In particular, this interaction reproduces the transition into the island of inversion in a quantitative manner. The measured spectroscopic factors for negative-parity states in ^{29}Mg and ^{31}Mg populated in one-neutron knockout reactions were in good agreement with SDPF-M calculations [25]. It should be noted that these calculations suggested the existence of a transitional region approaching the island of inversion, as opposed to a sharp transition proposed in early studies [12].

Other interactions for large-scale shell-model calculations in this mass region have also been developed. One example is the SDPF-U-MIX interaction [13]. This interaction is an extended version of the SDPF-U interaction [40], which was originally designed for $0\hbar\omega$ calculations of neutron-rich nuclei around $N = 28$. This interaction is similar to the SDPF-M interaction, where TBMEs and SPEs are empirically adjusted to reproduce selected experimental observables. The neutron configuration space is extended with respect to the SDPF-M interaction. In addition to the full *sd* shell, all of the *fp*-shell orbitals ($1f_{7/2}$, $2p_{3/2}$, $2p_{1/2}$, and $1f_{5/2}$) are included.

The EEdf1 interaction [41] is the latest interaction designed for large-scale shell-model calculations with the valence space of the full *sd* and *pf* shells for both protons and neutrons. The construction of this interaction is different from the SDPF-M and SDPF-U-MIX interactions. The TBMEs of this interaction were microscopically derived from the extended Kuo-Krenciglowa method and the Entem-Machleidt QCD-based nucleon-nucleon interaction. Even though the SPEs were fitted to reproduce selected experimental observables, no adjustments of the TBMEs were performed.

From the experimental side, detailed spectroscopy of nuclei in and around the island of inversion serves as a stringent test of these shell-model calculations and provides hints for further refinements of interactions. Moreover, experimental data of nuclei lying at the transitional region are of particular importance, as the shell-model calculations are expected to be sensitive to details

of interactions.

1.4 Current understanding of ^{30}Mg

1.4.1 Conventional picture of the inversion at ^{30}Mg and ^{32}Mg

As sketched in Section 1.2, ^{32}Mg is a monumental example of the island-of-inversion nucleus, while ^{30}Mg, the nucleus of interest of this study, is considered to be located just outside the island of inversion. In a simplified picture, the nuclear structure of these nuclei and the transition into the island can be outlined as follows [27, 28].

The ground state of ^{30}Mg is described by a normal configuration where all the active neutrons are confined to the *sd* shell and there are no cross-shell excitations across the $N = 20$ gap (0p0h configuration). On the other hand, the ground state of ^{32}Mg is described by two neutrons promoted across the $N = 20$ gap, giving rise to a 2p2h intruder configuration. The situation is inverted for the excited 0^+ states: the structure of the 0^+_2 state in ^{30}Mg is characterized by a 2p2h configuration, while the 0^+_2 state in ^{32}Mg is dominated by a 0p0h configuration. This "inversion" picture is often explained together with the notion of the shape coexistence: an almost spherical configuration and a prolate-deformed configuration are coexisting in ^{30}Mg, the spherical ground state of ^{30}Mg corresponds to the excited 0^+ state in ^{32}Mg, and vice versa. The firm identification of the first excited 0^+ states in ^{30}Mg and ^{32}Mg respectively reported by Schwerdtfeger *et al.* and Wimmer *et al.* has added evidence on this picture [27, 28]. In addition, the moderate electric monopole strength $\rho^2(E0; 0^+_2 \rightarrow 0^+_1) = 26.2(75) \times 10^{-3}$ [27] observed in ^{30}Mg is consistent with a weak mixing of the two 0^+ states with largely different intrinsic quadrupole deformation. To summarize, it has been conjectured that the crossing of two configurations with largely different shapes occurs between ^{30}Mg and ^{32}Mg, as schematically shown in Figure 1.8. This is the current, simplified picture of the underlying configurations in ^{30}Mg and ^{32}Mg.

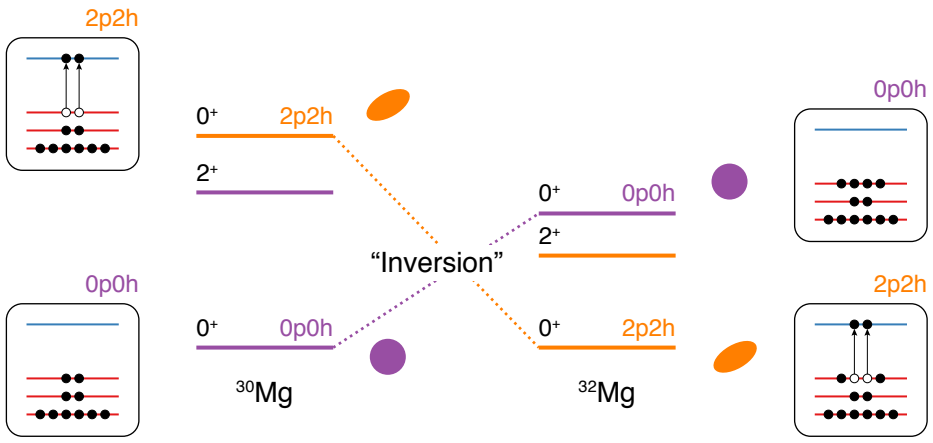

Figure 1.8: Schematic illustration for the simplified picture of the inversion of the low-lying 0^+ states in ^{30}Mg and ^{32}Mg. Neutron configurations are depicted in the boxes. As noted in the caption of Figure 1.5, not only the $1d_{3/2}$ and $1f_{7/2}$ orbitals, but also the other orbitals can contribute to cross-shell excitations.

The shape coexistence in ^{30}Mg and ^{32}Mg is theoretically supported by beyond-mean-field calculations by the angular momentum projected generator coordinate method with the Gogny

interaction using the D1S parameterization [42–44]. This calculation is built on top of the mean-field approximation (Hartree-Fock-Bogoliubov approximation). In order to incorporate additional many-body correlations, prescriptions such as the restoration of the broken rotational symmetry are included in the calculation. The results of the calculations are shown in Figure 1.9. The points in the figure show the intrinsic quadrupole deformations of the ground and excited 0^+ states. It can be seen that the ground state of ^{30}Mg is almost spherical on average, while the excited 0^+ is prolate-deformed. It should be noted that the picture presented above may be too simplified, as the ground-state collective wave function of ^{30}Mg shown in Figure 1.9 has, within this model, substantial mixing of oblate and prolate deformations. The situation is clearly inverted in ^{32}Mg with less shape fluctuations. The ground state is characterized by a prolate-deformed shape, while the excited 0^+ is spherical. The interpretation of spherical and deformed shapes and their coexistence in ^{30}Mg is also supported by beyond-mean-field calculations using the five-dimensional quadrupole collective Hamiltonian derived from the Hartree-Fock-Bogoliubov method and the local quasiparticle random phase approximation [45]. In the calculations, the picture in which the deformed 0^+ state coexists with the spherical 0^+ state approximately holds for ^{30}Mg, although large-amplitude quadrupole fluctuations are dominating in both 0^+ states in ^{32}Mg.

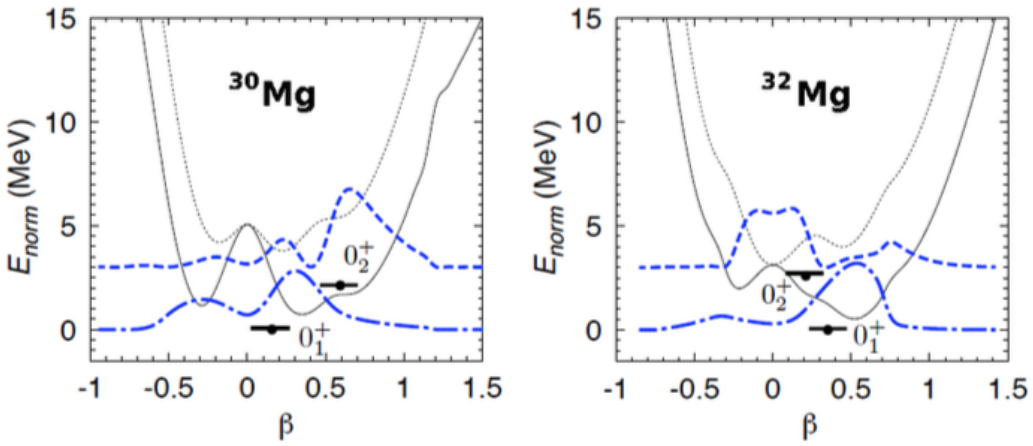

Figure 1.9: Potential energy surfaces and collective wave functions calculated for ^{30}Mg and ^{32}Mg [44]. The black lines are the results of particle number projected calculations (solid) and the angular momentum projected energy surfaces (dotted). The blue lines are the collective wave functions that express the probability of having a deformation of β for the ground (dashed-dotted) and the excited (dashed) 0^+ states. Note that a positive (negative) value of β represents prolate (oblate) deformation.

1.4.2 Negative-parity states

In *sd*-shell nuclei, negative-parity states are formed by promoting an odd number of particles from the *sd* to the *fp* shell. This is because the $N = 20$ shell gap originates from the two major shells with opposite parities. Therefore, if one assumes a pure 1p1h excitation, the excitation energy of negative-parity states is related to the size of the $N = 20$ shell gap. Here, it is instructive to show that negative-parity states have been used to discuss the evolution of the $N = 8$ gap around the neutron-rich nucleus ^{12}Be [7, 46], where the gap is formed between the $1p_{1/2}$ and the $1d_{5/2}$ or $2s_{1/2}$ orbitals. Analogous to the region around ^{32}Mg, the disappearance

of the $N = 8$ magic number was observed in neutron-rich nuclei around ^{12}Be [8, 9]. Excitation energies of the lowest 1^- state in $N = 8$ isotones are shown in Figure 1.10 (a). The sudden lowering of the excitation energies of the 1^- state could be interpreted in terms of the shell evolution in a qualitative manner. Starting at $Z = 6$, protons are removed from the $1p_{3/2}$ orbital, and the gap between the neutron $1p_{1/2}$ and $2s_{1/2}$ orbitals could be reduced by the monopole effects. In this way, the weakening of the $N = 8$ gap was discussed based on the negative-parity states [46].

Recent experimental results on ^{30}Mg questioned the current understanding of the structure of this nucleus. Measurements of the ^{14}C(^{18}O,2p)^{30}Mg fusion-evaporation reaction [47] and the one-neutron knockout reaction from ^{31}Mg [48] proposed candidates for negative-parity states at around 2.5 MeV. However, these excitation energies are in contradiction to the expectations from shell-model calculations, which predicted negative-parity states occurring only above 3.5 MeV. In Figure 1.10 (b), the systematics of exciitation energies of the lowest negative-parity state prior to this work are shown. As can be seen in the figure, candidates for the negative-parity states in ^{30}Mg are lying even lower than those in ^{32}Mg [49], which is located inside the island of inversion. The low excitation energy of these states could be interpreted in terms of the significant reduction of the $N = 20$ gap. It may also imply a substantial structural change taking place at ^{30}Mg.

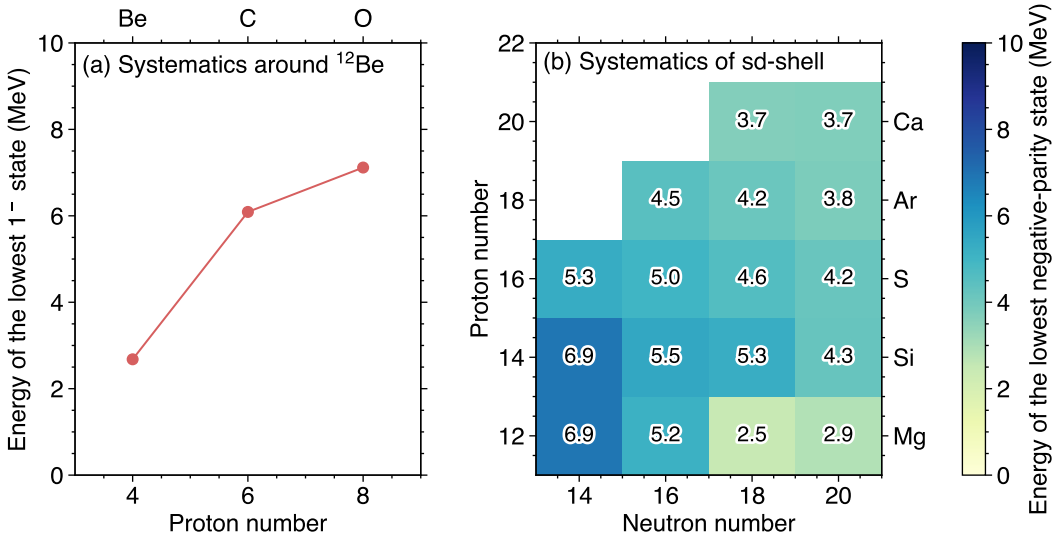

Figure 1.10: (a) Excitation energies of the lowest 1^- state in the $N = 8$ isotones. The values are taken from [46] (^{16}O: 7.1 MeV, ^{14}C: 6.1 MeV, ^{12}Be: 2.68 MeV). (b) Systematics of the lowest negative-parity states in *sd*-shell nuclei (including candidates) prior to this study. Level data are taken from the latest ENSDF database [4].

1.4.3 Previous experimental studies on ^{30}Mg

The nuclear structure of ^{30}Mg has been studied by β decay and β-delayed neutron emission from Na isotopes [19, 27, 50–55], Coulomb excitation [56–58], the two-neutron removal reaction from ^{32}Mg [59], the ^{14}C(^{18}O,2p)^{30}Mg fusion-evaporation reaction [47], and the one-neutron knockout reaction from ^{31}Mg [48]. Some selected experimental level schemes of ^{30}Mg constructed by

these previous studies are shown in Figures 1.11 and 1.12, together with the level scheme presented in the latest compilation where all of the experimental data collected before 2010 are combined [60]. In the following, a comprehensive, chronological review of the previous studies on ^{30}Mg is presented.

The neutron-rich unstable nucleus ^{30}Mg was first observed in a measurement of heavy-ion induced reactions [61]. A few years later, ^{30}Mg was also identified by a β-decay measurement of neutron-rich Na isotopes performed at CERN [62]. Following the first measurement of the nuclear mass in 1978 [63], Détraz *et al.* reported the first β-γ spectroscopy of ^{30}Na in 1979 [19]. An intense 1484-keV γ ray observed in this measurement was assumed to correspond to the $2^+_1 \rightarrow 0^+_1$ transition in ^{30}Mg from the systematics. This study was followed by more detailed β-γ measurements at CERN [50, 51]. Ten excited states were first reported by Guillemaud-Mueller *et al.*, and a new level and transitions were added later by Baumann *et al.* In addition to the measurements of β decay of ^{30}Na, states in ^{30}Mg were populated by β-delayed one-neutron emission from ^{31}Na and two-neutron emission from ^{32}Na [50, 52–54].

Since 1999, three measurements of Coulomb excitation on ^{30}Mg have been reported. The first two measurements reported transition strengths in contradiction to each other: $B(E2; 0^+_1 \rightarrow 2^+_1) = 295(26)\, e^2\mathrm{fm}^4$ [56] and $435(58)\, e^2\mathrm{fm}^4$ [57]. An experiment employing "safe" Coulomb excitation, where the reaction was performed at beam energies well below the Coulomb barrier, was reported by Niedermaier *et al.* in 2005 [58]. The extracted $B(E2; 0^+_1 \rightarrow 2^+_1)$ was $241(31)\, e^2\mathrm{fm}^4$. This moderately small $B(E2)$ is in line with shell-model calculations with a *sd*-shell model space, and it was concluded that ^{30}Mg is located outside the island of inversion.

In the early β-γ studies [50–52], the 1820-keV and 1789-keV γ rays were assigned as decays directly going to the ground state. Mach *et al.* reported a new placement of these transitions, revealing a cascade of 1789-keV, 1820-keV, and 1482-keV γ rays [53]. In the same experiment, the lifetimes of the states were measured using a fast-timing technique. The long lifetime of 3.9(4) ns suggested that the 1789-keV state is a candidate for the first excited, intruder 0^+ state. Additionally, the 2467-keV state was tentatively assigned as 2^+_2, and an upper limit of the lifetime for this state was determined to be 5 ps.

In 2009, the $E0$ transition from the first excited 0^+ candidate at 1789 keV to the ground state was directly measured by Schwerdtfeger *et al.* [27], putting the spin-parity assignment of 0^+ on a firm footing. This finding agrees with the picture where the ground state of ^{30}Mg is characterized by a (nearly) spherical, normal configuration, while the first excited 0^+ state is a manifestation of a deformed, shape-coexisting configuration dominated by fp intruder orbitals. The measured monopole transition strength of $\rho^2(E0; 0^+_2 \rightarrow 0^+_1) = (26.2 \pm 7.5) \times 10^{-3}$ was moderate, implying a small mixing of configurations.

States in ^{30}Mg were also populated by the two-neutron removal reaction from ^{32}Mg [59]. A spin-parity of 4^+ was proposed for the 3302-keV state, based on the large cross section to populate this state. Note that the γ-ray energies were not constrained in the analysis due to the limited energy resolution.

An in-beam γ-ray measurement using the ^{14}C(^{18}O,2p)^{30}Mg fusion-evaporation reaction, performed at Argonne National Laboratory, was reported by Deacon *et al.* in 2010 [47]. The main advantage of using the fusion-evaporation reaction was that states of higher energy and spin are more efficiently populated than β decay. States at 2541 keV, 3379 keV, 4181 keV, 4258 keV, 4357 keV, and 5311 keV were reported for the first time. Owing to a high degree of spin alignment, γ-ray angular distributions allowed spin-parity assignments to be made for several states. The spin-parity assignments of 4^+, 4^+, and 5 were respectively given to the

3379-keV, 3455-keV, and 4181-keV states. In addition, a tentative $(2,3)^-$ assignment was made for the 2541 keV, guided by non-observation of this state in β decay.

In 2014, a β-decay measurement employing a spin-polarized beam of ^{30}Na was reported Shimoda *et al.* [55]. The states at 4683 keV, 4694 keV, 5897 keV and 6064 keV were newly placed in the level scheme. By measuring the β-decay asymmetry inherent to the polarized parent nucleus, the 4967-keV, 5022-keV, 5095-keV, 5414-keV, and 6064-keV states were assigned as positive parity states, respectively 1^+, 1^+, 2^+, 2^+, and 2^+. Moreover, tentative spin-parity assignments were made for the other excited states based on γ-ray multipolarities and β-decay branching ratios.

Recently, Fernández-Domínguez *et al.* reported the results of in-beam γ-ray spectroscopy using the one-neutron knockout reaction from ^{31}Mg performed at GANIL [48]. Although the statistics were limited, based on the parallel momentum distribution of the knockout residue, the states at 2467 keV, 3298 keV, 3534 keV, and 4252 keV were suggested as candidates for negative parity. The interpretation of the states at 2467 keV is contradicting with the earlier β-decay study by Mach *et al.* in which the 2_2^+ assignment is proposed [53]. The excitation energy of this negative-parity level is lower than expected, and it could not be reproduced by shell-model calculations. Spectroscopic factors for one-neutron removal from ^{31}Mg were also extracted, and a small spectroscopic factor associated with the 0_2^+ state was reported.

To summarize, much experimental effort has been devoted to study ^{30}Mg. However, spins and parities of excited states higher than 2 MeV, except for the states strongly populated in ^{30}Na β decay, are not yet well established. Moreover, as mentioned in Section 1.4.1, the recent in-beam experiments [47, 48] questioned the current understanding of the structure of ^{30}Mg. These remaining challenges were addressed within this work.

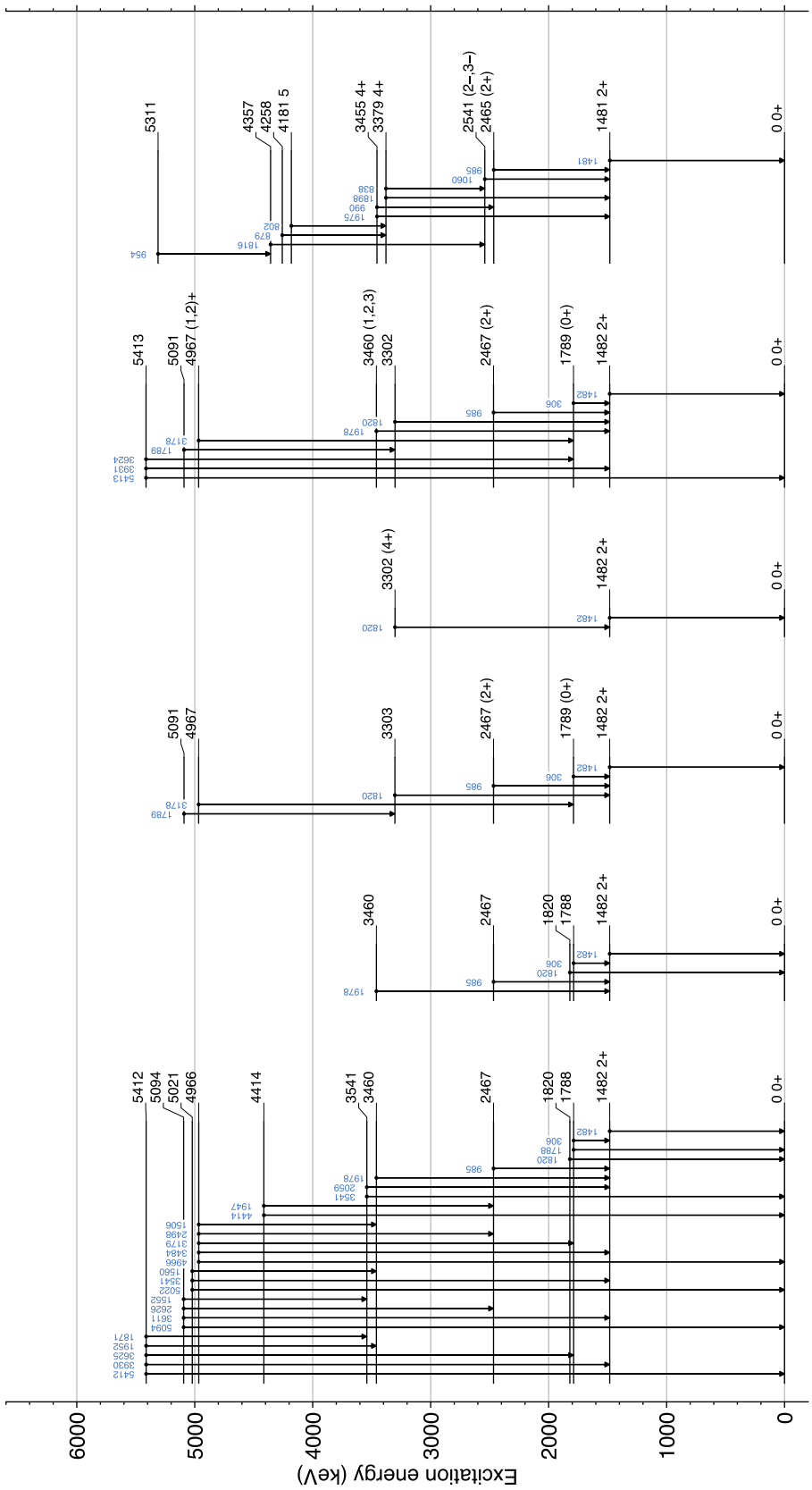

Figure 1.11: Level schemes of ^{30}Mg constructed by previous experiments [27, 47, 51–53, 59]. Energies and spin-parity assignments including parentheses are presented without modifications.

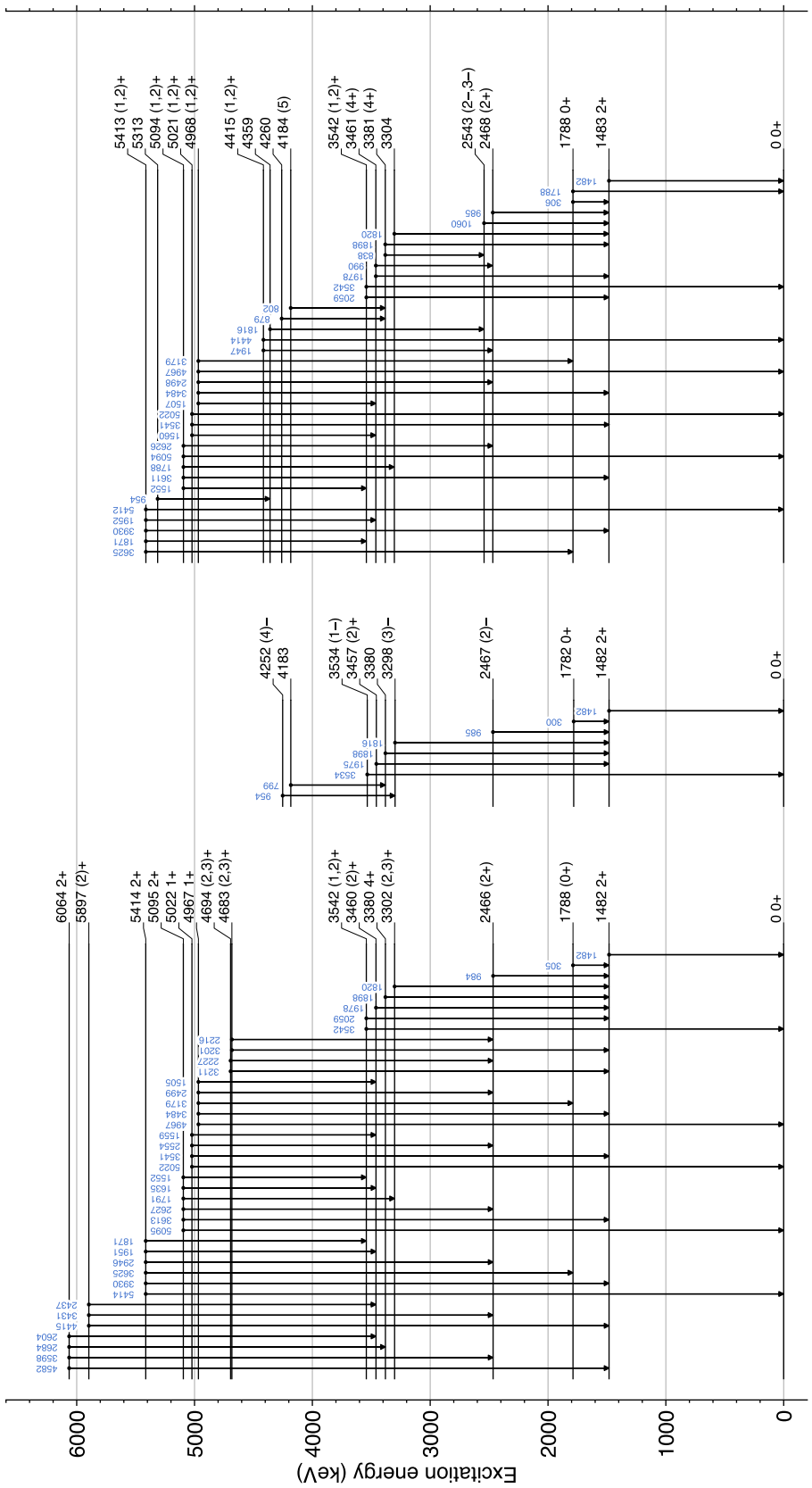

Figure 1.12: Continuation of Figure 1.11. Level schemes constructed by [48, 55, 60] are shown.

1.5 Thesis objectives and outline

This thesis presents detailed in-beam γ-ray spectroscopy of ^{30}Mg located at the boundary of the island of inversion. The primary goal of the present experiment is to provide new experimental data to track structural evolution approaching the island of inversion. Detailed spectroscopic information on ^{30}Mg offers a rich testing ground for nuclear theories and our understanding of the transition into the island of inversion. Of particular importance is the location of negative-parity states. As explained in Section 1.4.2, the excitation energy of these states is expected to reflect the size of the $N = 20$ gap. The sensitivity of negative-parity states to the gap size has already been demonstrated for $N = 8$ isotones. Therefore, it is important to firmly assign spins and parities to excited states in ^{30}Mg. Recent in-beam studies [47, 48] proposed negative-parity states lying at unnaturally low energy. These negative-parity states located at 2.5 MeV could not be reproduced by shell-model calculations, where predictions are 3.5 MeV or higher. Moreover, the excitation energy is even lower than negative-parity candidates in ^{32}Mg which is firmly placed inside the island of inversion. These experimental results were interpreted as an unusual structural change in ^{30}Mg and posed questions concerning the current theoretical description. This further demands a detailed spectroscopic study for conclusive spin-parity assignments.

In the present experiment, nucleon removal reactions were employed to populate states in ^{30}Mg. In particular, in the one-neutron knockout reaction from ^{31}Mg, the well-studied reaction mechanism for the knockout reactions allowed for the determination of the angular momentum of the removed neutron and the extraction of spectroscopic factors. As mentioned above, the excitation energy of negative-parity states is expected to reflect the shell-gap size, and it also serves as a key test to the shell model along with the spectroscopic factors. To populate states in ^{30}Mg, the two-neutron removal reaction from a ^{32}Mg beam was also employed. As this reaction does not proceed as direct knockout, the states are populated rather statistically. Similarly, multi-nucleon removal reactions from ^{34}Si and ^{35}P are also exploited. High-spin yrast states (states with minimum energy for a given spin) could be preferentially populated when multiple nucleons are removed. In addition to the main reaction channel of this study, i.e. one-neutron knockout from ^{31}Mg, analyses of these reaction channels were used to provide complimentary information particularly useful for the construction of an updated, reliable level scheme and spin-parity assignments.

This thesis consists of seven chapters. The details of in-beam γ-ray spectroscopy and one-nucleon knockout reactions are outlined in Chapter 2. The formalism of the reaction theory based on the eikonal approximation and the way of extracting key quantities, spin-parities and spectroscopic factors, are covered in this chapter. The experimental setup, the detector systems, and the electronics used in this work are detailed in Chapter 3. The data analysis steps, including calibration and correction procedures, Monte Carlo simulations, the extraction of cross sections and momentum distributions are described in Chapter 4. The results obtained in this work, including an updated level scheme of ^{30}Mg with spin-parity assignments and spectroscopic factors, are presented in Chapter 5. The nuclear structure of ^{30}Mg is discussed in Chapter 6 by comparing the present result with shell-model calculations and systematics of neighboring nuclei. Finally, the experimental findings obtained in the present experiment and future perspectives are summarized in Chapter 7.

Chapter 2

In-beam spectroscopy with radioactive beams

In this chapter, details on the experimental method adopted in this work are described. Section 2.1 reviews in-beam γ-ray spectroscopy. Section 2.2 illustrates the theory for nucleon knockout reactions used to analyze and interpret the experimental observables.

2.1 Overview of in-beam γ-ray spectroscopy

In-beam γ-ray spectroscopy is a powerful method to study excited states in nuclei. The effectiveness of this approach was first demonstrated by Morinaga and Gugelot [64], where rotational bands in the Gd isotopes were observed by measuring in-flight γ rays emitted following (α, xn) fusion-evaporation reactions. This pioneering work triggered many studies employing in-beam γ-ray spectroscopy, and nowadays it is widely used as a major spectroscopic tool that complements other spectroscopic approaches such as β-delayed γ-ray spectroscopy.

To study nuclear structure far from stability, in-beam γ-ray spectroscopy is often utilized in combination with fast radioactive beams. This is because unstable nuclei are efficiently produced by fragmentation of stable beams at an intermediate energy, typically more than 100 MeV/nucleon, and the resulting unstable nuclei are available for experiments in the form of fast radioactive beams. In-beam γ-ray spectroscopy following various reactions can be used to populate excited states in the nucleus of interest. Each type of reaction has specific sensitivities to observables that reflect nuclear structure. One example is a one-nucleon knockout reaction, the method of choice for the present study. This reaction is characterized by its high selectivity and sensitivity to the shell structure, as detailed in Section 2.2. Another example is a multi-nucleon removal reaction, or fragmentation-like reaction, where multiple nucleons are removed from the projectile nucleus. This reaction does not proceed as a direct, single-step process, and the population of excited states in the reaction residue is less sensitive to the nuclear structure. In-beam γ-ray spectroscopy with heavy-ion reactions that involve removal of many nucleons was first studied in 1978 [65]. Later, it was observed that multi-nucleon removal reactions favor the population of high-spin yrast states [66] in a pioneering experiment [67]. This feature is similar to that of fusion-evaporation reactions. In the present study, multi-nucleon removal reactions were also employed for the detailed spectroscopy of ^{30}Mg.

Firm identification of the reaction products and efficient detection of γ rays emitted in flight are essential in in-beam γ-ray spectroscopy, and a dedicated system is required for this

purpose. Details on the particle and γ detection systems used in the present study are described in Section 3.2 and 3.3.

2.2 Reaction mechanism

Nucleon knockout reactions are a well-suited spectroscopic tool for fast beams of unstable nuclei [68]. In the present experiment, the one-neutron knockout reaction on ^{31}Mg induced by a ^{9}Be target was performed to get insight into the nuclear structure of ^{30}Mg. In this section, the theory of one-neutron knockout reactions using the eikonal approximation is described, together with explanations on how one connects the experimental observables to the structural information. The discussions presented here are based on [69–73].

2.2.1 One-nucleon knockout reactions

Direct reactions are characterized by a simple reaction mechanism, and are powerful tools for studying nuclear structure experimentally. Historically, nucleon transfer reactions performed at energies around 10 MeV/nucleon have been widely used as a standard direct reaction, and these reactions are well established for studies of both stable and unstable nuclei. Since the 1990s nucleon knockout reactions on intermediate-energy beams of unstable nuclei have also been used as an alternative direct reaction for spectroscopic studies of exotic nuclei. In typical nucleon knockout reactions, a projectile nucleus of mass A with a velocity $\beta = 0.3$ or higher impinges on a nuclear target, most often ^{9}Be or ^{12}C, and the $A - 1$ residual nucleus after the single nucleon removal is detected. The residue moves at nearly the same velocity as the projectile, and the longitudinal component of the residue's momentum can be used to determine the angular momentum of the single-particle orbital from which the nucleon has been removed. The cross sections to populate states in the residue give information about the overlap in the wave functions describing the projectile and residual nuclei. The reaction is advantageous over classical nucleon-transfer reactions as it can produce excited states of the nucleus of interest with relatively high cross sections. In addition, the combination of fast radioactive beams and thick targets enables one to perform measurements on exotic nuclei whose beam intensities are limited. It should be noted that electron-induced proton knockout reactions, namely $(e, e'p)$, are used to study stable nuclei. However, these reactions cannot be applied to exotic nuclei as these reactions are only possible in normal kinematics, and thus the scope has been limited to stable or very long-lived nuclei. Another drawback is that they are only sensitive to proton orbitals and one cannot probe neutron orbitals. The use of nucleon knockout reactions induced by a nuclear target can overcome these difficulties.

The main observables in nucleon knockout reactions are the cross sections and the momentum distributions. These observables are compared with reaction calculations to extract the structural information. In the theory developed by Tostevin *et al.* [69], the reactions are modeled based on the eikonal approximation. This theory also assumes the sudden approximation where the internal reconfiguration of the core (^{30}Mg in the present case) is neglected, so the core is assumed to be a spectator during the reaction. This formalism is widely used in the analyses of nucleon knockout reactions, and the present work also adopts this theoretical framework. The basic procedure of the reaction calculations is outlined in the flowchart shown in Figure 2.1. The calculations are detailed in the following sections.

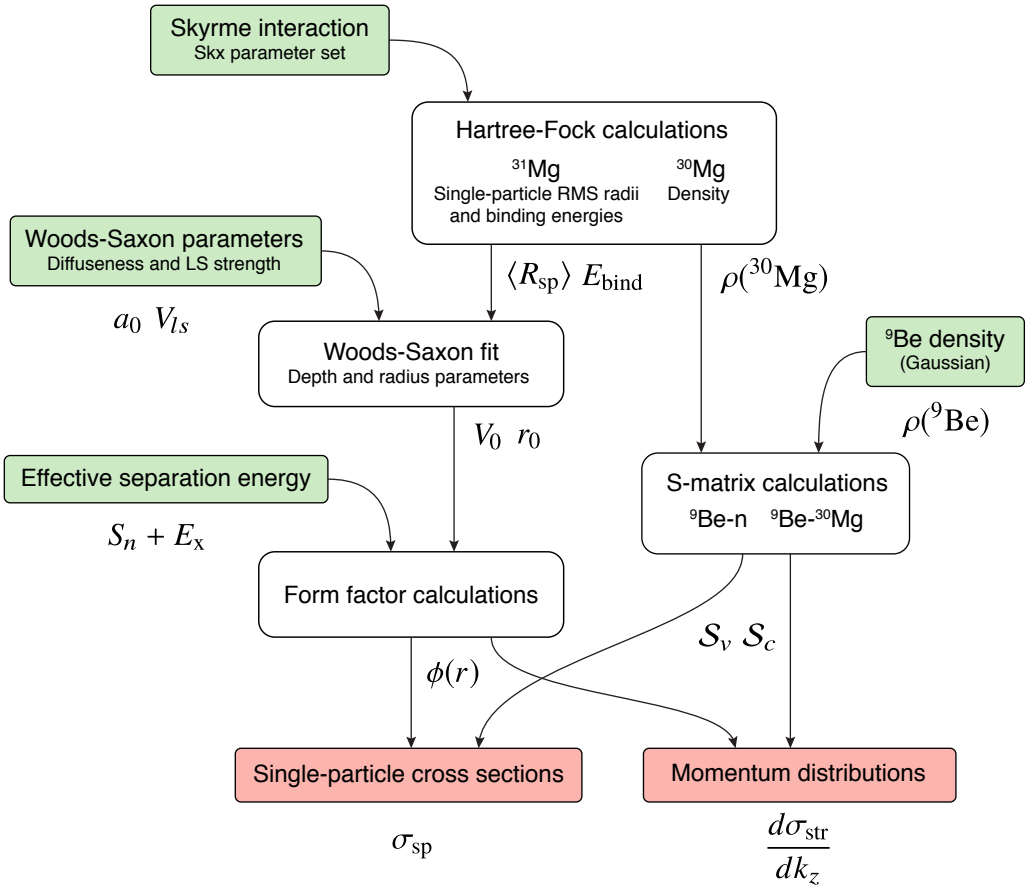

Figure 2.1: Flowchart of the knockout reaction calculations performed in this work. The input parameters are shown in green. The outputs, single-particle cross sections and momentum distributions, are indicated in red.

2.2.2 Single-particle cross sections

Two reaction processes contribute to the cross sections of the one-nucleon knockout reaction. As schematically shown in Figure 2.2, the two processes are called stripping and diffraction. Note that the stripping and diffraction processes are sometimes called inelastic and elastic breakup, respectively. Strictly speaking, elastic breakup caused by the Coulomb interaction, called Coulomb dissociation, also contributes to the cross sections. For light targets such as ^{9}Be, its contribution can be neglected.

In the stripping process, the valence nucleon is absorbed by the target nucleus that behaves like a black disk. On the other hand, the nucleon is elastically removed from the projectile in the diffraction process. The target nucleus is excited in the stripping process, while it remains in the ground state in the diffraction process. In principle, the two processes are distinguishable by looking at the final state of the target nucleus. However, this is not the case in situations where only the residual nucleus is detected, like in the present experiment. The one-nucleon knockout cross section is thus given by the direct sum of these processes:

$$\sigma_{\mathrm{ko}} = \sigma_{\mathrm{str}} + \sigma_{\mathrm{diff}}. \tag{2.1}$$

For deeply-bound nucleons, the stripping cross section is larger than the diffraction cross section.

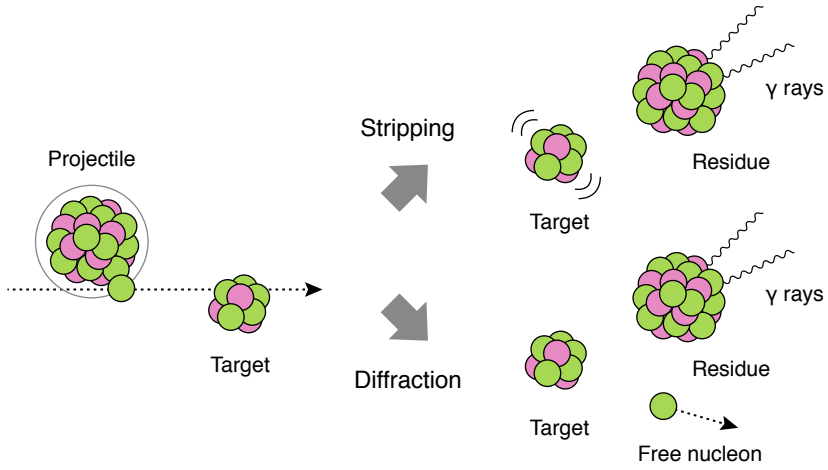

Figure 2.2: Schematic illustration of the two processes in the one-nucleon knockout reaction, stripping and diffraction. In the stripping process, the target nucleus absorbs the valence nucleon and gets excited. In the diffraction process, the target nucleus is a spectator, and the valence nucleon is elastically scattered.

The absorption in the stripping process can be modeled based on the probability concepts associated with the eikonal S matrices. In a reaction where the two-body projectile composed of c (core) and v (valence) incident on a target, the stripping cross sections can be calculated by

$$\sigma_{\mathrm{str}} = \frac{1}{2J+1} \sum_{m} \int d^2\boldsymbol{b} \left\langle \phi_0^m \right| |\mathcal{S}_c|^2 \left(1 - |\mathcal{S}_v|^2\right) \left| \phi_0^m \right\rangle \tag{2.2}$$

where $\boldsymbol{b}$ is the impact parameter between the core and target, J is the angular momentum of the projectile, $\mathcal{S}_v$ and $\mathcal{S}_c$ are respectively the eikonal S matrices of the valence-target and core-target systems, and ϕ_0^m is the core-valance wave function. $|\mathcal{S}_c|^2$ corresponds to the survival of the core, while $1 - |\mathcal{S}_v|^2$ describes the absorption of the valence nucleon.

The diffraction cross section is given by

$$\sigma_{\mathrm{diff}} = \frac{1}{2J+1} \sum_{mm'} \int d^2\boldsymbol{b} \int d^3\boldsymbol{k} \left| \left\langle \phi_k^{m'} \right| \mathcal{S}_c \mathcal{S}_v \left| \phi_0^m \right\rangle \right|^2 . \tag{2.3}$$

This process is further decomposed into two components: the refraction component originating from the imaginary part of the potential and the diffraction component originating from the real part. In the above expression, these two components are added coherently. For simplicity, it is common to refer to them as the diffraction process. This expression describes the excitation of the core and target into the continuum. Using the completeness relation

$$\sum_{m'} \int d^3\boldsymbol{k} \left| \phi_k^{m'} \right\rangle \left\langle \phi_k^{m'} \right| = 1 - \sum_{m'i} \left| \phi_i^{m'} \right\rangle \left\langle \phi_i^{m'} \right| \tag{2.4}$$

Equation (2.3) can be reformulated as

$$\sigma_{\mathrm{diff}} = \frac{1}{2J+1} \sum_{mm'} \int d^2\boldsymbol{b} \left(\left\langle \phi_0^{m'} \right| |\mathcal{S}_c \mathcal{S}_v|^2 \left| \phi_0^m \right\rangle - \sum_i \left| \left\langle \phi_i^{m'} \right| \mathcal{S}_c \mathcal{S}_v \left| \phi_0^m \right\rangle \right|^2 \right) \tag{2.5}$$

where i labels the bound states in the core-valence system. The first term of Equation (2.5) corresponds to the case where both the target and core survive. The sum in the second term is often neglected and only the ground state $\left\langle \phi_0^{m'} \right| |\mathcal{S}_c\mathcal{S}_v|^2 \left| \phi_0^m \right\rangle$ is considered. This approximation is valid if one assumes the ground state is the only bound state, $\left\langle \phi_i^{m'} \right| |\mathcal{S}_c\mathcal{S}_v|^2 \left| \phi_0^m \right\rangle \approx 0$ for $i \neq 0$. Although this assumption is not realistic, it is known that this is still a good approximation [69].

In the calculation of the stripping and diffraction cross sections, the generation of the eikonal S matrices for the core- and valence-target systems is essential. The core-target (valence-target) S matrix can be calculated using the double-folding (single-folding) optical limit of Glauber's multiple scattering theory. To carry out these calculations, the core and target densities are required. In the standard approach of the knockout calculations, the core density is obtained from a Hartree-Fock calculation, while the target density is approximated by a Gaussian with an RMS radius of 2.36 fm for ^{9}Be. The densities are illustrated in Figure 2.3. For the Hartree-Fock calculation, usually the Skyrme force with the Skx parameter set is used [74].

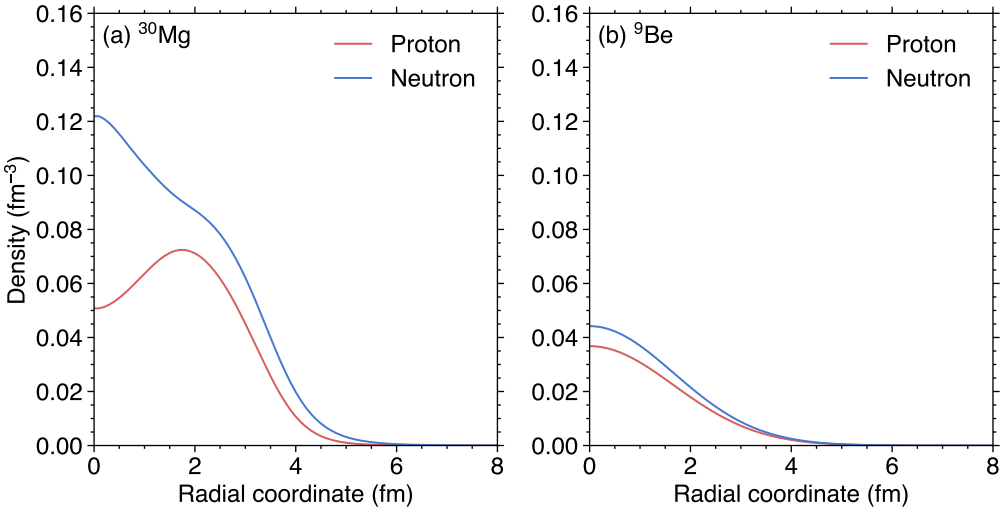

Figure 2.3: Proton and neutron densities for (a) the ^{30}Mg core taken from Skyrme Hartree-Fock calculations with the Skx parameter set, and for (b) ^{9}Be approximated by a Gaussian with an RMS radius of 2.36 fm.

2.2.3 Form factors

The core-valence two-body wave function $\phi(r)$, which is often referred to as the form factor, is also required for the reaction calculations. The form factor is calculated by solving the Schrödinger equation for a nucleon confined in a Woods-Saxon plus spin-orbit potential of Equation (1.4). In this approach, the well depth V_0, the spin-orbit strength V_{ls}, the radius r_0, and the diffuseness a_0 are treated as free parameters. It is found that the spin-orbit strength and the diffuseness have only a small impact on the resulting cross section. The standard values of these parameters are 0.7 fm and 6 MeV, respectively [75]. The radius parameter and the well depth are simultaneously adjusted to reproduce the RMS radius of the single-particle orbital of a Skyrme-Hartree-Fock calculation with a scaling ($r_0 = \sqrt{A/(A-1)}r_{\mathrm{HF}}$) and the single-particle binding energy of the Skyrme-Hartree-Fock calculation. After obtaining the adjusted r_0 and V_0,

the well depth is once again changed to reproduce the experimental effective separation energy defined as $S_N + E_x$, with S_N being the nucleon separation energy between the ground states of nuclei of interest and E_x the energy of the excited state. The approach described here is named the well-depth prescription, which is commonly used in analyses of nucleon knockout reactions. To keep the consistency with previous studies, the well-depth prescription is adopted in this work. In Figure 2.4, some examples of calculated form factors for ^{30}Mg plus one neutron are shown.

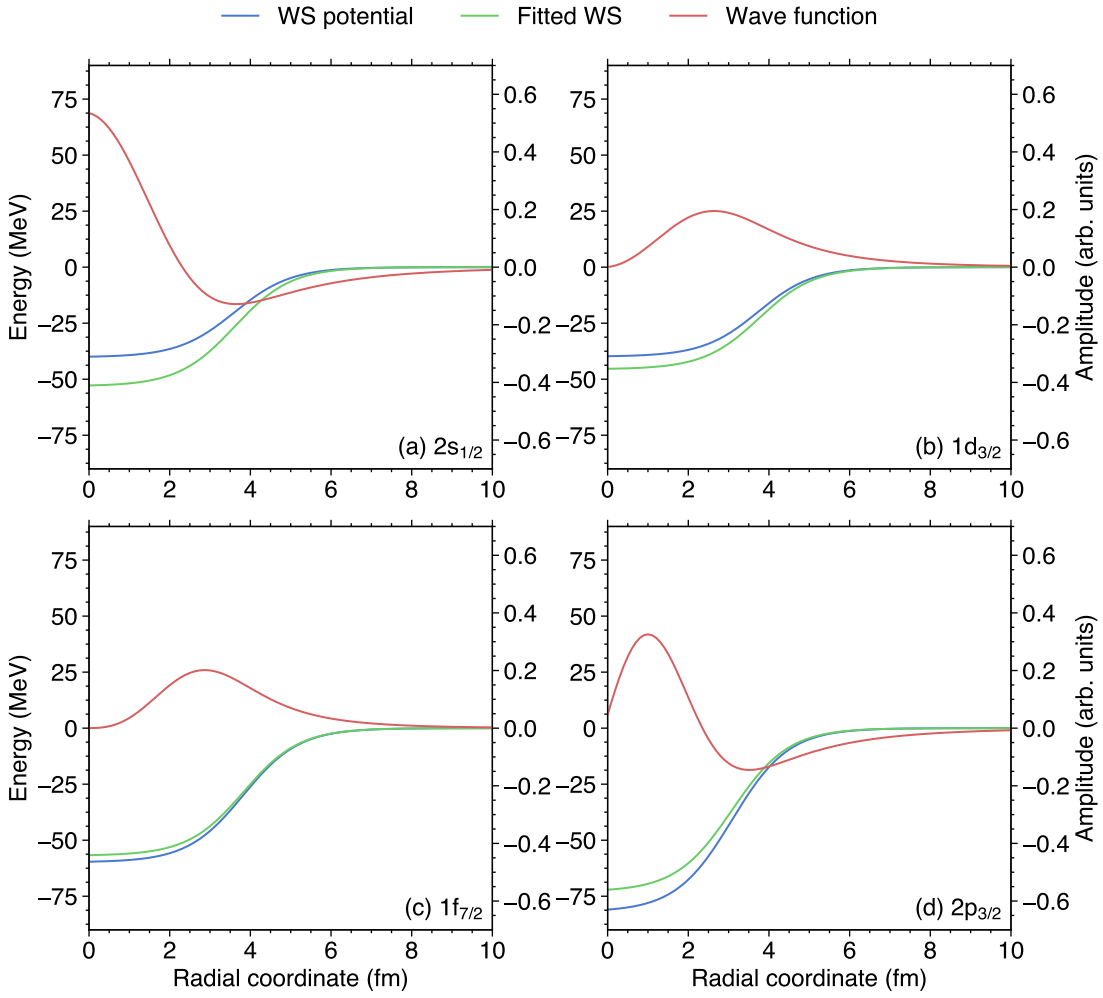

Figure 2.4: Form factors of the ^{30}Mg core and one neutron calculated for (a) $2s_{1/2}$, (b) $1d_{3/2}$, (c) $1f_{7/2}$, and (d) $2p_{3/2}$ orbitals (red solid lines). The calculations were performed with the well-depth prescription. Woods-Saxon plus spin-orbit potentials of Equation (1.4) are also visualized. The blue solid lines show the potentials after adjusting the depths to reproduce the effective separation energies, while the green lines show the potentials "fitted" to the Hartree-Fock results.

2.2.4 Momentum distributions

In the sudden approximation, the following relation between the momenta of the struck nucleon $\boldsymbol{k}_v$, projectile $\boldsymbol{k}_A$, and residue $\boldsymbol{k}_{A-1}$ holds:

$$\boldsymbol{k}_v = \frac{A-1}{A}\boldsymbol{k}_A - \boldsymbol{k}_{A-1}. \tag{2.6}$$

Provided the beam's momentum $\boldsymbol{k}_A$ is known, the momentum of the struck nucleon $\boldsymbol{k}_v$ can be reconstructed by measuring $\boldsymbol{k}_{A-1}$.

To infer the orbital angular momentum of the removed nucleon, the longitudinal (parallel to the projectile's direction) momentum distribution can be utilized. This is because the momentum distribution is given by the Fourier transform of the core-valence wave function from coordinate space to momentum space. This approach is analogous to the angular distributions of ejectiles often employed in transfer reactions. The momentum distribution can be calculated using the core and valence S matrices and the core-valence wave function. Historically, the transverse (perpendicular) momentum distribution had also been utilized as an indicator of the angular momentum. Later, it was found that diffractive effects and Coulomb scattering complicate the transverse momentum distribution, so nowadays the longitudinal momentum distribution is used for this purpose. The longitudinal momentum distribution associated with the stripping process is calculated by [76]

$$\frac{d\sigma_{\mathrm{str}}}{dk_z} = \int d^2\boldsymbol{b}_v(1-|\mathcal{S}_v(\boldsymbol{b}_v)|^2)\int d^2\boldsymbol{r}_\perp|\mathcal{S}_c(|\boldsymbol{b}_v-\boldsymbol{r}_\perp|)|^2\frac{1}{2l+1}\sum_m\left|\int dz\frac{e^{-ik_z z}}{2\pi r}\phi_{jlm}(r)\right|^2 \tag{2.7}$$

where $\boldsymbol{b}_v$ denotes the impact parameter of the valence nucleon, $\boldsymbol{r}$ is the vector between the core and valence nucleon, and $\phi_{jlm}(r)$ is the single-particle wave function (here the total angular momentum j, orbital angular momentum l and its projection m are explicitly indicated). It was found that the shape of the momentum distribution of the diffraction process is almost the same as the one for stripping [71]. Therefore, the momentum distribution of the diffraction process is usually assumed to be identical to the stripping process. A comparison of calculated momentum distributions with experimental distributions allows for the determination of the orbital angular momentum of the struck nucleon. This enables to assign the spin and parity of the populated states, but the orbital angular momentum alone cannot identify the spin (total angular momentum) of the populated state uniquely.

For an illustrative purpose, calculated parallel momentum distributions are shown in Figure 2.5. The calculation assumes neutron knockout reactions from s, p, d, and f orbitals in ^{31}Mg. It is clear that the width of the momentum distribution is indicative of the orbital angular momentum. Note that when comparing these calculations with experimental distributions, the calculated momentum distributions need to be convoluted with the resolution of the measurement system.

2.2.5 Spectroscopic factors

The spectroscopic factor is used to describe the overlap between the initial- and final-state wave functions. In the present case, the structural overlap between the ground state of ^{31}Mg and the final state in ^{30}Mg is quantified. The spectroscopic factor S is related to the amplitude of

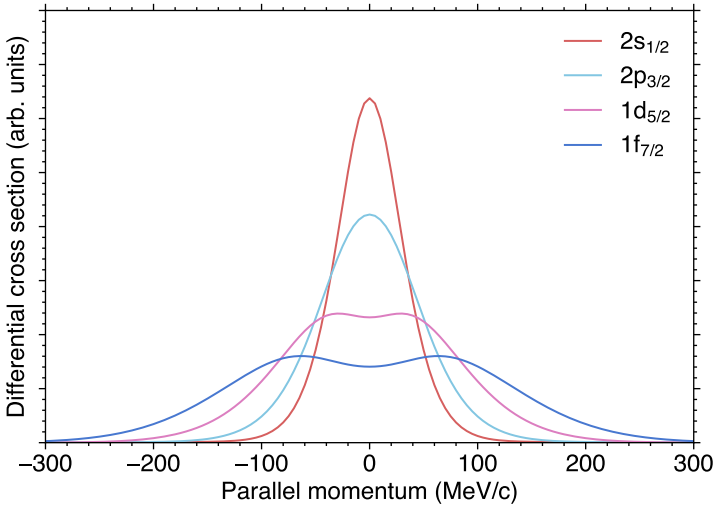

Figure 2.5: Momentum distributions calculated for neutron knockout from $2s_{1/2}$, $1d_{3/2}$, $1f_{7/2}$, and $2p_{3/2}$ orbitals in ^{31}Mg. The calculation assumes a neutron binding energy of 2.310 MeV for the four orbitals.

removing a nucleon from an initial state $|\Phi_i^A\rangle$ to a final state $|\Phi_f^{A-1}\rangle$ and is defined as

$$S = \frac{1}{2J_i+1} \sum_{M_i M_f} \left| \left\langle \Phi_f^{A-1} \left| \tilde{a}_{k,m} \right| \Phi_i^A \right\rangle \right|^2 = \frac{1}{2J_i+1} \left| \left\langle \Phi_f^{A-1} \left\| \tilde{a}_k \right\| \Phi_i^A \right\rangle \right|^2 . \tag{2.8}$$

where J_i means the initial spin, k stands for single-particle quantum numbers nlj, and $\tilde{a}_{k,m}$ is defined using the annihilation operator $a_{k,m}$ as

$$\tilde{a}_{k,m} = (-1)^{j+m} a_{k,-m}. \tag{2.9}$$

In the last expression of Equation (2.8), the Wigner-Eckart theorem has been used. The spectroscopic factor is often calculated in the isospin formalism. In this case, the spectroscopic factor with an explicit isospin label $S(T)$ is related to the one in the proton-neutron formalism by $S = C^2 S(T)$ with C being the isospin Clebsch-Gordan coefficient. This is often simply written as C^2S.

The spectroscopic factor is usually calculated with the shell model. When making comparisons with experimental spectroscopic factors [77], a center-of-mass correction to shell-model spectroscopic factors needs to be applied. The correction is given by

$$C^2S \rightarrow \left(\frac{A}{A-1} \right)^N C^2S \tag{2.10}$$

where $N = 2n + l$ corresponds to the major oscillator quantum number.

The theoretical cross section to populate final states J^π by removing nucleons with single-particle quantum numbers nlj is given by

$$\sigma_{\mathrm{th}} = \sum_{nlj} \left(\frac{A}{A-1} \right)^N C^2S(J^\pi, nlj) \sigma_{\mathrm{sp}}(S_N + E_{\mathrm{x}}(J^\pi), nlj) \tag{2.11}$$

where the first factor is the center-of-mass correction for the shell-model spectroscopic factors already given by Equation (2.10), the second one is the spectroscopic factor taken from the shell-model calculation, and the last one is the single-particle cross section from reaction calculations evaluated at the effective separation energy. The single-particle cross section σ_{sp} should contain both contributions from the stripping and diffractive breakup processes.

2.2.6 Quenching of spectroscopic factors

One-nucleon knockout reactions are an established tool for spectroscopic studies of nuclei far from the stability line. However, a systematic reduction of spectroscopic factors with respect to theoretical predictions has been observed, and it remains an open question regarding the theoretical description of the reaction [75, 78]. The reduction factor, sometimes referred to as the quenching factor, is defined as the ratio of the experimental and theoretical cross sections

$$R_S = \frac{\sigma_{\mathrm{exp}}}{\sigma_{\mathrm{th}}}. \tag{2.12}$$

From extensive studies on electron-induced proton knockout reactions on stable nuclei, it was found that the reduction factor lies between 0.5 and 0.7 [79]. Recent studies on nuclear-target-induced knockout reactions on unstable nuclei with high asymmetry in proton and neutron numbers revealed that the reduction factors are 0.8–0.9 for the knockout of a weakly bound nucleon and 0.3–0.4 for a deeply bound nucleon [78]. The reduction of spectroscopic factors is not unique to knockout reactions. This phenomenon was also observed in "traditional" low-energy transfer reactions such as (p, d) [80]. Much effort has been devoted to this problem, but a complete understanding is not yet obtained. The reduction of the spectroscopic factors is currently considered to be originating from correlations due to short-range interactions as well as longer-range couplings missing in the nuclear structure theories with a truncated model space.

Gade *et al.* have pointed out that the reduction factors show a tight correlation when plotted against the difference in separation energies ΔS. Here the ΔS is defined as $S_n - S_p$ for neutron removal and $S_p - S_n$ for proton removal [75]. Therefore, ΔS is a measure of the asymmetry of the Fermi surfaces for neutrons and protons. In Figure 2.6, R_S is shown as a function of the asymmetry parameter ΔS. In nuclear structure studies employing nucleon knockout reactions, the reduction factor is sometimes treated as an empirical parameter that can be inferred from the systematics. An empirical reduction factor is parameterized as

$$R_S(\Delta S) \approx 0.61 - 0.016\Delta S, \tag{2.13}$$

where ΔS is measured in units of MeV. This empirical formula was taken from a fit to a collection of observed reduction factors. In this work, for instance, the reduction factor for the ground state is taken to be $R_S = 0.87$ for ^{31}Mg ($S_n = 2.310(5)$ MeV and $S_p = 18.86(6)$ MeV [3]).

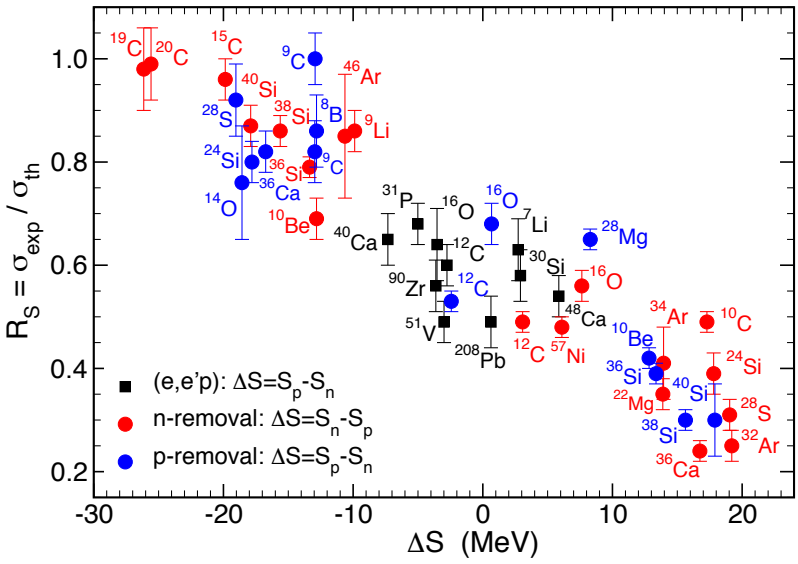

Figure 2.6: Systematics of the ratio R_S of the experimental and theoretical cross sections for one-neutron (red circles) and one-proton (blue circles) removal as a function of the asymmetry parameter ΔS. The black squares are for electron-induced proton knockout reactions. Figure taken from [78].

Chapter 3

Experiment

The present experiment was carried out at the National Superconducting Cyclotron Laboratory (NSCL) at Michigan State University [81]. Secondary beams of ^{31}Mg, ^{32}Mg, ^{34}Si, and ^{35}P were delivered by the A1900 fragment separator and impinged on a beryllium reaction target to induce nucleon removal reactions. A combination of the momentum analysis of knockout residues and the prompt γ-ray detection made it possible to extract cross sections and parallel momentum distributions associated with each state in ^{30}Mg. The momentum analysis of the ^{30}Mg residue was performed with the S800 magnetic spectrograph, by measuring their trajectories using charged-particle detectors at the focal plane of the spectrograph. De-excitation γ rays emitted from ^{30}Mg were detected by an array of high-purity germanium detectors, GRETINA, which surrounded the reaction target. In the first four sections, the beam delivery, devices, detectors, and electronics relevant to the experiment are described in detail. A summary of the data collected during the experiment is also presented in Section 3.5.

3.1 Production of radioactive beams

In the present experiment, excited states in ^{30}Mg are studied via nucleon removal reactions from ^{31}Mg, ^{32}Mg, ^{34}Si, and ^{35}P. Since these nuclei are unstable to β decay and short-lived, they are produced as radioactive ion beams. There are mainly two techniques employed for the production of radioactive ion beams. One is the isotope separation online (ISOL) method [82]. In this approach, a very thick target is irradiated by, in most cases, a high-intensity proton beam, and radioactive isotopes are produced by spallation, fission, and fragmentation reactions of the target nuclei. The radioactive ions are extracted from the target, ionized, separated, and accelerated to perform nuclear reaction studies. The other is the in-flight method [82, 83]. In this approach, a heavy-ion beam at relatively high energy (typically more than 100 MeV/nucleon), impinges on a production target and interacts with the target nuclei. A fast beam of radioactive ions is produced by spallation, fission, and fragmentation reactions of the projectile nuclei. As the beam contains a wide range of radioactive nuclides, the beam is sometimes called a “cocktail”, and this necessitates mass separation online.

The latter approach was adopted in the present experiment. One of the advantages of using in-flight over ISOL technique is that the high velocity of the beam allows for the use of a thicker reaction target as compared to ones used in experiments employing low-energy beams since the fast beam loses very little energy in the target. This means that there are more collision centers available and thus a gain in luminosity.

Note that, in in-beam experiments, sometimes the presence of isomeric states in the beam causes problems. In the case of nucleon knockout reactions, the population of the states changes depending on the initial state of the projectile, and usually it is very difficult to disentangle which state is populated from the ground or isomeric states. There are two known long-lived states in ^{31}Mg, the $3/2^+_1$ and $7/2^-_1$ states. Nevertheless, these states would have decayed over the flight path, as the lifetimes of these states [84] are much shorter than the traveling time in the A1900. Therefore, the incoming ^{31}Mg cannot be in an excited state when the knockout reaction takes place.

The secondary beams were produced by impinging a primary beam of ^{48}Ca on a beryllium production target. To produce the primary beam, first ^{48}Ca has to be ionized and accelerated up to a relativistic energy. A sample of ^{48}Ca was heated and vaporized, and the resulting neutral atoms were then ionized inside an electron cyclotron resonance (ECR) type ion source. The ions were sent to the first stage of the coupled cyclotron facility, namely the K500 superconducting cyclotron [85]. The ions were accelerated up to 12.32 MeV/nucleon inside this cyclotron with a radio-frequency (RF) electric field and a stational magnetic field. The RF matches the cyclotron frequency of the ion, $qB/\gamma m$. The beam was extracted using an electric deflector and transported via the coupling line to another superconducting cyclotron, the K1200. A carbon foil is placed at the entrance of the K1200 so that the electrons are stripped off the ion for a higher charge state. This allows the ion to be further accelerated without increasing the magnetic field or the radius of the cyclotron. The charge state of ^{48}Ca changed to fully stripped (20+) by the carbon stripper. The beam was further accelerated up to 140 MeV/nucleon, corresponding to 50 % of the speed of light.

The primary beam extracted from the K1200 was directed onto a thick beryllium production target, where a cocktail beam of radioactive nuclides is produced by projectile fragmentation [83, 86]. The thickness of the production target used for the present experiment was 846 mg/cm^2. The secondary beam of interest is then selected from the rest of the fragmentation products by the A1900 fragment separator [87, 88], which spans from the production target to the focal plane. This device has a large acceptance to achieve a high collection efficiency of fragments, making it the second-largest acceptance fragment separator currently in operation [81]. As illustrated in Figure 3.1, the A1900 consists of eight triplets of superconducting quadrupole magnets and four 45° dipoles with a maximum magnetic rigidity of 6 Tm. The specifications of the A1900 include a solid-angle acceptance of 8 msr, a momentum acceptance of 5.5 %, and a momentum resolution of 3000. First, the fragments emerging from the production target were selected by a magnetic rigidity of the first half of the A1900 with a combination of slits. The selection is based on the fact that the momentum-to-charge ratio p/q is proportional to the magnetic rigidity $B\rho$. In fragmentation reactions, the velocities of the fragments are almost the same as the projectile. In addition, at intermediate energies, the ions are mostly in the fully-stripped charge state. Therefore, the separator allows ions with a narrow range of A/Z values to be transmitted. An achromatic wedge-shaped degrader of aluminum with a thickness of 300 mg/cm^2 was placed at the intermediate image 2 (see Figure 3.1). The wedge degrader is essential for further purification of the beam. The principle of the purification is referred to as the momentum-loss achromat [89]. Fragments with different atomic numbers experience different energy losses when passing through the degrader since the stopping power is proportional to the atomic number squared, i.e. $-dE/dx \propto Z^2$. Therefore, the use of the degrader leads to different magnetic rigidities depending on the atomic number, while the wedge shape of the degrader recovers the achromatism of the fragment separator. Thus, the second half of the A1900 provides

isotopic separation of fragments. Finally, the fragments were transported to the final focal plane of the A1900 where the dispersion cancels. It has to be noted that the overall momentum acceptance of the A1900 is set by the slits of all the dispersive focal planes. The final focal plane of the A1900 immediately follows the extended focal plane and the transfer line coupled to the S800 spectrograph detailed in the next section. A thin plastic scintillator named XFP is installed at the extended focal plane and the scintillation light is read out by one photomultiplier. In the present experiment, the thickness of the scintillator was chosen to be 163 µm. The signal from this detector provides the timing information for the particle identification of incoming particles. Details on the particle identification are given in the following sections.

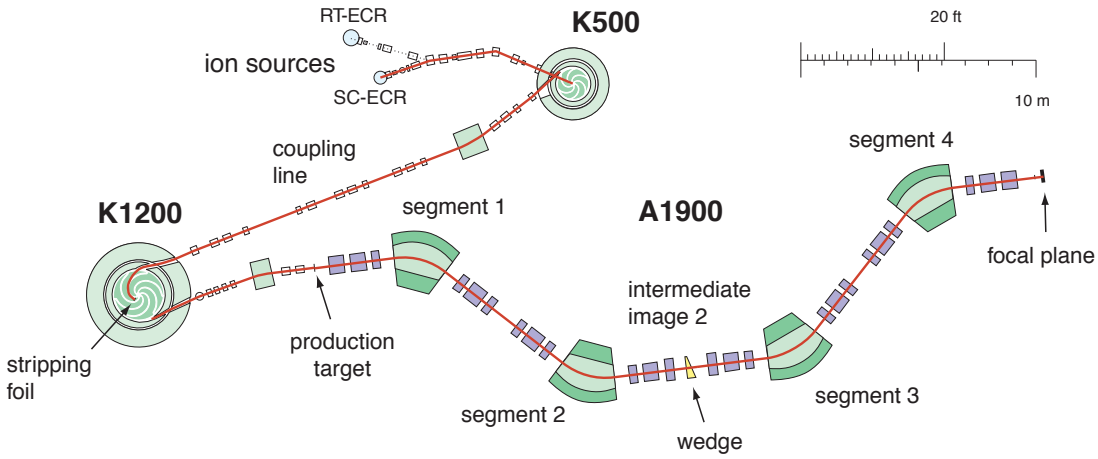

Figure 3.1: Top view of the coupled cyclotrons and the A1900 fragment separator. The secondary beam produced and purified by the A1900 separator is transmitted to the S800 via the transfer line (not shown in this figure) beyond the A1900's focal plane. Figure taken from [88] with modifications.

3.2 The S800 spectograph

The S800 is one of the key devices for experiments involving intermediate-energy radioactive beams, especially in-beam γ-ray spectroscopy at NSCL [90]. An illustration of the S800 is shown in Figure 3.2. The device is composed of two main parts. The first part is called the analysis line, and it refers to the section between the object point and the reaction target. The beam coming from the A1900 fragment separator bends by 45° downward, passes through the intermediate image, then bends by 45° upward, and finally directed onto the reaction target. For the present experiment, a beryllium target with a thickness of 375 mg/cm^2 was chosen. The target assembly consists of a beryllium plate of 5 cm × 5 cm and a plastic frame and cradle to hold the target. The assembly is inserted in the beam pipe using a push stick of a specific length to ensure that the target is placed at the designed target position properly. The other part of the S800 is the spectrograph that provides momentum-analysis of the residuals after reactions. The spectrograph spans from the target to the focal plane. The outgoing particles are first focused by two superconducting quadrupole magnets and then deflected by two dipoles by 150°. According to the relation $B\rho = p/q$, the magnetic rigidity of the dipoles is adjusted to cover the outgoing particles of interest. The spectrograph also has a large acceptance. More specifically, it is

characterized by a solid angle acceptance of 20 msr and a momentum acceptance of ±2 %. Ions with a magnetic rigidity up to 4 Tm can be transported. The spectrograph can rotate around the target to measure the angular distribution of reaction products, but it is not necessary for this kind of experiments, so the rotation is fixed at 0°.

For the operation of the analysis line and the S800, several modes of ion optics are available. In the present experiment, the so-called focused mode was used. In this mode, the analysis line is tuned to be achromatic and the beam is focused on the target. As the momentum spread at the object point propagates to the focal plane, the resolution for the momentum transfer is determined by the momentum acceptance of the A1900 fragment separator. This mode provides a large momentum acceptance of ±2 % in the analysis line and is suitable for experiments where a high momentum resolution is not required. For a better resolution, the beam trajectory in the middle of the analysis line provides momentum tagging, and for this purpose, a set of two Parallel Plate Avalanche Counters (PPACs) at the intermediate image can be utilized. The individual strip readout enables them to function at a relatively high counting rate. However, in the present experiment, the PPACs received a large number of incoming ions that caused damages on them. This resulted in a much lowered detection efficiency, so the beam track information from the PPACs was not used for the in-beam data analysis.

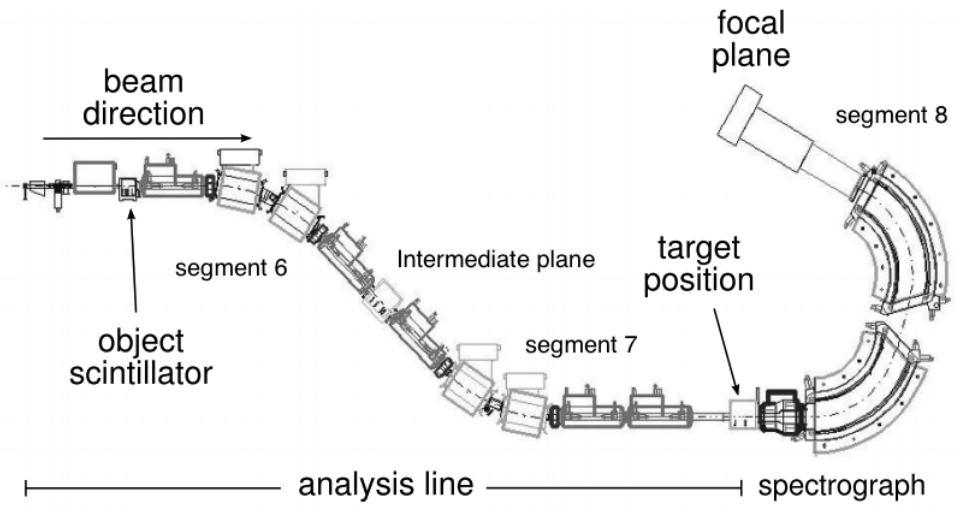

Figure 3.2: Side view of the S800. The radioactive beam is transported through the analysis line and reactions take place at the target position. The reaction residues are analyzed by the S800 spectrograph and detected in the focal plane. Figure taken from [91] with modifications.

3.2.1 Detector setup

The focal plane of the S800 spectrograph is equipped with a pair of cathode-readout drift chambers (CRDC) to track the trajectory of the outgoing particles, an ionization chamber to measure the energy loss for the atomic-number identification, and a plastic scintillator for the time-of-flight (TOF) measurement and triggering of the electronics and data acquisition [92]. The detectors in the focal plane are illustrated in Figure 3.3.

The CRDCs provide a measurement of position and angle in the focal plane. The first CRDC

is placed at the actual focal plane of the ion optics. The second detector is placed downstream and is separated by 1073 mm from the first one. The principle of operation of these detectors is almost identical to that of a (single-wire) drift chamber, except that the signals induced on segmented cathodes are read out so that the detector is sensitive to the position along the wire direction. An outgoing particle passing through the CRDC ionizes the gas filled in the detector, ionization electrons drift toward the anode wire with an electric field, and the induced charges on cathode pads are read out. The cathode pads are arranged with a pitch of 2.54 mm along the vertical direction. The position along the horizontal direction is determined by the drift time of ionization electrons measured relative to the timing signal from the E1 scintillator, which is described later. The resulting position resolution is about 0.5 mm in both directions. The CRDCs are filled with a gas mixture of 80 % tetrafluoromethane and 20 % isobutane typically at a pressure of 40 Torr. The detectors have an active depth of 1.5 cm and an active area of 30 cm × 59 cm.

An ionization chamber is located downstream of the CRDCs. This detector provides a measurement of the energy lost by the outgoing particle while traversing the detector, and this information is used to identify the atomic number, as the energy loss is proportional to the atomic number squared (c.f. the Bethe-Bloch formula). The detector is filled with P10 gas i.e. a mixture of 90 % argon and 10 % methane at a pressure of 300 Torr. The active area of the detector is almost the same as that of the CRDC and the active depth is 406 mm. It consists of 16 pairs of alternating anodes and cathodes perpendicular to the beam direction. The advantage of the segmentation is that electrons and ions are collected quickly and thus pileup and position dependence effects are reduced.

A large plastic scintillator named E1 immediately follows the ionization chamber. This scintillator provides a measurement of the time of flight used for the particle identification and is also used to trigger the S800's electronics and data acquisition. The detector has a thickness of 1 mm and a comparable active area as those of the detectors upstream. The scintillator is coupled with two photomultipliers and the light is read out from both ends. Due to path-length differences of the particles traveling in the S800, the timing depends on the trajectory and is critical for the identification of the outgoing particles. This dependence can be corrected by using the position information provided by the CRCDs, and this correction is demonstrated later in Section 4.1.1.

Another plastic scintillator with a thickness of 254 µm is placed at the object point of the S800. This scintillator is called OBJ for short. As will be described in the section 3.2.3, the time difference between OBJ and E1 provides the TOF information for the identification of outgoing particles, while the time difference between OBJ and the scintillator at the A1900's extended focal plane (XFP) is used for the identification of incoming particles.

3.2.2 Four-momentum reconstruction

As reviewed in 3.2.1, the trajectory of the reaction residue is measured by the CRDCs. The hit positions from the two CRDCs allow for the determination the position and angle at the focal plane. These are represented by four parameters, x_{fp}, a_{fp}, y_{fp}, and b_{fp}. As the S800 has an upright configuration, one has to be careful with the convention of the coordinate system; x_{fp} is the position in the dispersive (vertical) direction and y_{fp} is the position in the non-dispersive (horizontal) direction. a_{fp} and b_{fp} are the angles associated with x_{fp} and y_{fp} respectively, and the z-axis points toward the beam direction. To correctly reconstruct the particle trajectory, the

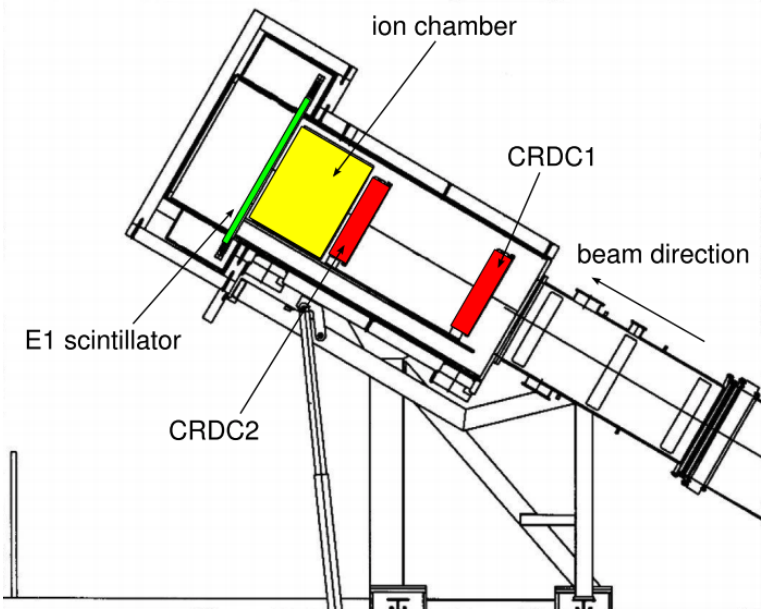

Figure 3.3: Illustration of the detector configuration at the S800 focal plane. Figure taken from [91].

position calibration is required for each CRDC. The calibration is illustrated in Section 4.1.1.

The set of four observables, x_{fp}, a_{fp}, y_{fp}, and b_{fp}, can be transformed into another set of parameters at the target position, a_{ta}, y_{ta}, b_{ta}, and d_{ta} [93]. All the parameters are defined in relation to a central trajectory of the S800 spectrograph, and the associated central momentum is given by $p_0 = qB\rho_0$. The definition of the first three parameters is trivial. The last parameter d_{ta} is defined as the relative (kinetic) energy deviation $(T - T_0)/T_0$ with T_0 being the kinetic energy equivalent to p_0. It should be noted that, when the transformation is performed, the x position at the target, x_{ta}, cannot be calculated and is assumed to be zero. A set of Taylor expansion coefficients that relates the parameters at the focal plane and the target position can be calculated using an ion optics code, and the resulting set of coefficients is called an ion-optic map. Usually, a map gives the propagation of ion trajectories going to the forward direction, but in the present case, an inverse version of the map is needed. The inverse map including aberration effects can be calculated by the code COSY INFINITY [94] by specifying the magnetic settings of the dipoles and quadrupoles. In the present work, coefficients up to fifth order are considered. Since the trajectory of particles depends on the magnetic setting of the spectrograph, an inverse map needs to be prepared for each reaction setting. The advantage of the inverse-map approach is the fast processing of data. Without using the inverse map, event-by-event ray tracing in the magnetic field would be necessary.

Once the parameters a_{ta}, y_{ta}, b_{ta}, and d_{ta} are reconstructed using the inverse map, the four-momentum p^μ can also be deduced. In the following, M, q, $B\rho$, and P respectively denote the particle's mass, charge, magnetic rigidity, and the magnitude of the three-momentum. First, using the relation

$$\gamma\beta = \frac{P}{M} = \frac{B\rho q}{M}, \tag{3.1}$$

the Lorentz factor $\gamma_0 = 1/\sqrt{1-\beta_0^2}$ corresponding to the magnetic rigidity setting of the S800

spectrograph $(B\rho)_0$ is given by

$$\gamma_0 = \sqrt{1 + (\gamma_0\beta_0)^2} = \sqrt{1 + \left(\frac{(B\rho)_0 q}{M}\right)^2}. \tag{3.2}$$

The parameter d_{ta}, defined as the fraction of the kinetic energy difference from the S800's central kinetic energy, is related to γ and γ_0 by

$$d_{\mathrm{ta}} = \frac{T - T_0}{T_0} = \frac{E - E_0}{E_0 - M} = \frac{\gamma - \gamma_0}{\gamma_0 - 1}. \tag{3.3}$$

Using this equality, one obtains

$$\gamma = \gamma_0 + d_{\mathrm{ta}}(\gamma_0 - 1). \tag{3.4}$$

Therefore, the kinetic energy and the magnitude of the momentum can be written as

$$T = M(\gamma - 1) = M[\gamma_0 + d_{\mathrm{ta}}(\gamma_0 - 1) - 1], \tag{3.5}$$

$$P = M\gamma\beta = M\sqrt{[\gamma_0 + d_{\mathrm{ta}}(\gamma_0 - 1)]^2 - 1}. \tag{3.6}$$

The four-momenta are written as

$$p^\mu = (T + M, P\hat{\boldsymbol{p}}) \tag{3.7}$$

where $\hat{\boldsymbol{p}}$ is the normalized momentum vector defined as

$$\hat{\boldsymbol{p}} = (\sin\theta\cos\phi, \sin\theta\sin\phi, \cos\theta). \tag{3.8}$$

The angles of the outgoing particle, θ and ϕ, are calculated from a_{ta} and b_{ta} using the following relations

$$\sin\theta = \sqrt{\sin^2 a_{\mathrm{ta}} + \sin^2 b_{\mathrm{ta}}}, \tag{3.9}$$

$$\tan\phi = \frac{\sin b_{\mathrm{ta}}}{\cos a_{\mathrm{ta}}}. \tag{3.10}$$

The normalized momentum vector can be rewritten as

$$\hat{\boldsymbol{p}} = \left(\sin a_{\mathrm{ta}}, \sin b_{\mathrm{ta}}, \sqrt{1 - (\sin^2 a_{\mathrm{ta}} + \sin^2 b_{\mathrm{ta}})}\right). \tag{3.11}$$

The parallel and transverse components of the momentum vector are then given by

$$p_\parallel = P\cos\theta = P\sqrt{1 - (\sin^2 a_{\mathrm{ta}} + \sin^2 b_{\mathrm{ta}})}, \tag{3.12}$$

$$p_\perp = P\sin\theta = P\sqrt{\sin^2 a_{\mathrm{ta}} + \sin^2 b_{\mathrm{ta}}}. \tag{3.13}$$

3.2.3 Particle identification

As briefly described in Section 3.2.1, three plastic scintillators (XFP, OBJ, and E1) are used to provide TOF measurements for the identification of incoming (secondary beam) and outgoing (reacted) particles. The time difference between the XFP and OBJ scintillators is proportional to the mass-to-charge ratio A/q of incoming particles. This is because the fragments have

been filtered by the A1900 fragment separator so that they have a common magnetic rigidity $B\rho = p/q$ and this implies that the product of the mass-to-charge ratio A/q of the fragment and its velocity stays constant. Provided that there are no other fragments that have almost the same A/q in the section between XFP and OBJ, the species of the incoming particles can be uniquely identified only by this TOF information. Similarly, the time-difference between OBJ and E1 is sensitive to A/q of outgoing particles. Here, one must consider the fact that the flight path inside the S800 spectrograph strongly depends on the momentum and angle of the outgoing particle, resulting in a TOF difference of the order of several nanoseconds. The TOF difference leads to a deteriorated outgoing particle identification, but the flight-path length can be corrected by using the measured position and angle information at the S800's focal plane. There can be drifts in the TOF due to damages on plastic scintillators caused by the beam irradiation. A time-dependent correction needs to be applied in addition to the flight-path correction. Together with the energy loss measured by the ionization chamber, which is proportional to Z^2, the particle identification of outgoing particles is accomplished without ambiguities. It has been observed that the measured energy loss also depends on the x position on the ionization chamber, but this can be easily corrected.

3.3 GRETINA

The high-resolution detection of prompt γ rays emitted from excited states in nuclei of interest was made possible with the Gamma-Ray Energy Tracking In-beam Nuclear Array (GRETINA), which is the key device of the present experiment. In this section, details on GRETINA and the basic procedure of the γ-ray data analysis are described.

3.3.1 Overview of GRETINA

GRETINA is a new-generation array of γ-ray detectors [95–97]. GRETINA is especially suitable for experiments with intermediate-energy radioactive-ion beams and it has demonstrated its power in a number of nuclear structure studies performed in various accelerator facilities. The results of commissioning experiments performed at NSCL are summarized in [98].

In the current experiment, the array consisted of 7 modules, each of which houses 4 crystals of high-purity germanium crystals (28 crystals in total). Each crystal is tapered in a hexagonal shape at the front face. There are two types of crystals which differ in the shapes, called A-type and B-type, so that a spherical surface is approximated when the crystals are closely packed. As can be seen in Figure 3.4, two A-type and B-type crystals share the same cryostat and are enclosed in one GRETINA module, which is sometimes called a quad. Overall, seven quads provide a solid angle coverage of about 1π. The high solid-angle coverage gives a photo-peak efficiency of about 5 % at 1 MeV.

One of the most important abilities of GRETINA is the sub-segment reconstruction of γ-ray interaction points. Each crystal is electrically segmented into 36 parts, as shown in Figure 3.4, for the γ-ray hit-position sensitivity. Online signal processing provides sub-segment interaction points with a resolution of 4 mm in FWHM [99]. This is one of the key developments and is crucial for the Doppler correction (see Section 3.3.2 for details).

It should be noted that GRETINA is still in the process of upgrading. In the foreseeable future, the construction of the full 4π array, γ-ray Energy Tracking Array (GRETA) that calls for 28 modules, is planned.

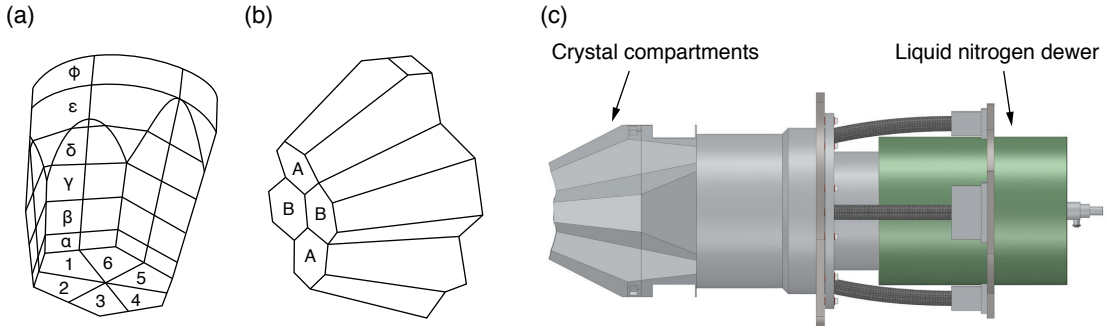

Figure 3.4: Schematic drawings of (a) an individual crystal with the electrical segmentation, (b) compartments housing four crystals, and (c) a GRETINA module. The crystal has a central contact (electrode) inside, but it is not visible in the figure. Taken from [97] with modifications.

Geometrical design

Photographs of the experimental setup in the S800 experimental hall and the GRETINA modules are shown in Figures 3.6 and 3.7. All the GRETINA modules are mounted on a rigid aluminum support frame composed of two hemispheres. The mounting positions on the support frame are called the holes. The current support frame has four and ten holes respectively in rings at 58° and 90°, relative to the beam axis. However, two positions at 90° are used for the axle mechanism to hold the frame. In the configuration adopted for the present experiment, four modules are mounted on the holes centered at 58° and the remaining three modules are mounted at 90°. This arrangement is called the NSCL standard configuration. The numbers associated with each hole and the crystal number within one module are indicated in the "world map" (see Figure 3.5). The distance between the target and the surface of the module is about 18 cm. The support frame is placed on a cart so that the two hemispheres can slide on rails. The positioning of the hemispheres is based on a guide-pin mechanism allowing high-precision alignment. It was found that the position of the hemispheres relative to the S800 experimental hall varies less than 1 mm [98].

Waveform processing

When a γ-ray interaction takes place, electron-hole pairs are generated in the crystal. They drift towards the electrodes according to the crystal's internal electric field. The charge signals induced on segments are sent to preamplifiers and the resulting transient waveforms are recorded by digitizers. By comparing the waveforms with basis signals generated by simulations, it is possible to achieve a higher position resolution than that determined by the electrical segment size. The basis signals are computed based on the Shockley-Ramo theorem in which the time evolution of the induced signal on the electrode, i.e. the instantaneous electric current is related to the motion of a charge in the crystal [100]. More specifically, The induced signals on the electrodes are calculated using weighting potentials $\phi_0(\boldsymbol{x})$, which are the solutions to Poisson's equation with boundary conditions that a specific electrode is set to a fixed potential of unity and the rest are grounded. The signal induced by moving electrons with charge $-q$ can be expressed as

$$Q(t) = -q\phi_0(\boldsymbol{x}(t)). \tag{3.14}$$

The motion of the holes also contributes to signal formation. Equation (3.14) implies that the transient signal carries information on the position where the γ-ray interaction takes place, and the signals are induced not only on the segment where a γ-ray interacts but also on neighboring segments. Together with the electric-field map of the crystal and the charge mobility, the basis signals induced on all the electrodes can be pre-generated for each interaction point by simulations. The observed signals are compared with the basis signals to find the best fit of the energy and interaction point. This waveform processing is termed "decomposition", and this technique has been applied to the Segmented Germanium Array (SeGA) [101], a progenitor of GRETINA at NSCL. It has to be noted that the basis signals generated by simulations are for a single interaction point, but the decomposition process also allows to handle more than one interaction point contained in one segment, since the measured signals are a superposition of those originating from individual interaction points. As a result of the decomposition, a set of energies and interaction points is obtained. The decomposition is performed by a dedicated computer farm in real time, so there is no need to run the decomposition process offline.

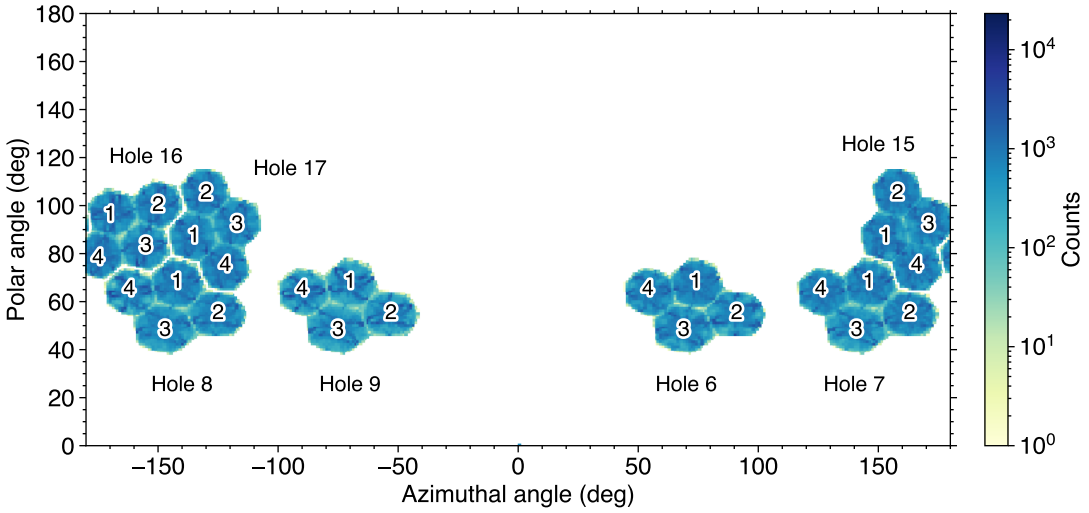

Figure 3.5: Distribution of the γ-ray hit positions, the "world map", taken from an offline measurement using a ^{152}Eu source. Hole and crystal numbers are indicated.

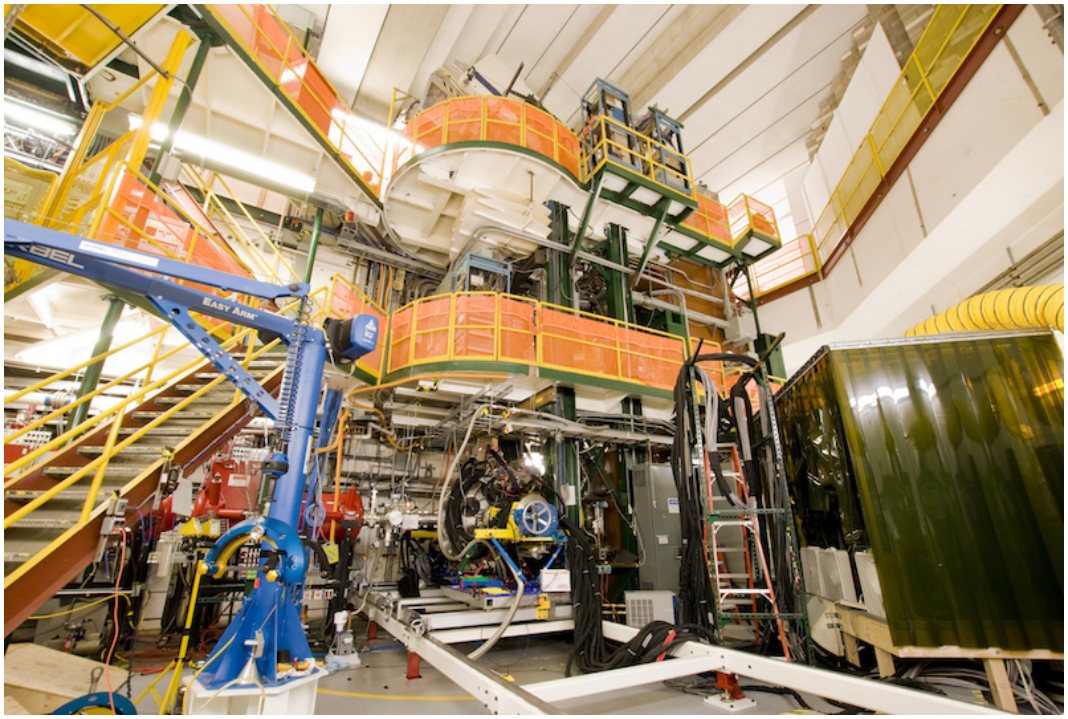

Figure 3.6: Experimental setup in the S800 vault. The beam comes from the left. GRETINA's supporting shell is seen at the center of this picture.

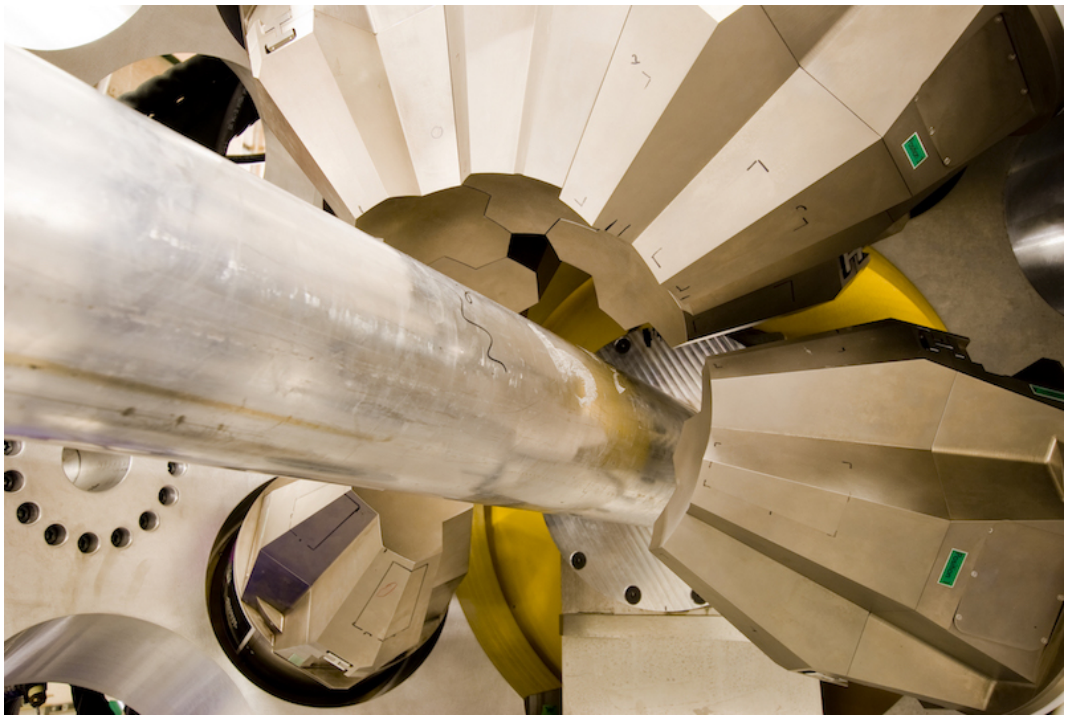

Figure 3.7: GRETINA modules in the NSCL standard configuration where seven quads are installed. The beam axis points into the paper. A reaction target is inside the beam pipe. Figures courtesy of Dr. Shumpei Noji at NSCL.

3.3.2 Doppler correction

As γ rays are emitted in flight typically at a velocity of 40 % of the speed of light, the γ-ray energies are affected by the Doppler effect. The formula for the Doppler shift is obtained by transformation of the γ-ray four-momenta $p^\mu = (E, \boldsymbol{p})$ from the intrinsic frame to the laboratory frame. The original γ-ray energy can be related to the observed energy in the laboratory frame as

$$E_{\mathrm{lab}} = E\gamma(1 + \beta\cos\alpha) \tag{3.15}$$

where α denotes the emission angle of the γ ray in the intrinsic frame. By inverting this equation, one obtains

$$E = E_{\mathrm{lab}}\gamma(1 - \beta\cos\alpha_{\mathrm{lab}}). \tag{3.16}$$

This means that one can reconstruct the actual transition energy knowing the emission angle of the γ ray. This is the main reason that the γ-ray hit position sensitivity is critical for in-beam γ-ray spectroscopy with fast beams.

Due to the finite position resolution and the uncertainty in the velocity of the residual, the γ-ray peak in the Doppler-corrected spectrum is more broadened than the intrinsic energy resolution ΔE_{int}. The fractional peak broadening is calculated as

$$\left(\frac{\Delta E}{E}\right)^2 = \left(\frac{\Delta E_{\mathrm{int}}}{E_{\mathrm{lab}}}\right)^2 + \left(\frac{\gamma^2(\beta - \cos\alpha_{\mathrm{lab}})}{1 - \beta\cos\alpha_{\mathrm{lab}}}\right)^2 \Delta\beta^2 + \left(\frac{\beta\sin\alpha_{\mathrm{lab}}}{1 - \beta\cos\alpha_{\mathrm{lab}}}\right)^2 \Delta\alpha_{\mathrm{lab}}^2 \tag{3.17}$$

where $\Delta\alpha_{\mathrm{lab}}$ is the uncertainty in the angle arising from the finite position resolution and $\Delta\beta$ is the uncertainty in the velocity. The overall energy resolution and the contributions from each term are visualized in Figure 3.8. In forward and backward angles, the contribution from the velocity uncertainty dominates. As the target thickness is the main source of the velocity uncertainty, the target should be as thin as possible, but this is a trade-off between the resolution and luminosity. The intrinsic energy resolution also contributes to the Doppler-corrected energy, but its impact on the overall energy resolution is not large.

3.3.3 Add-back analysis

Instead of being fully absorbed in one crystal, a γ ray might also be scattered into neighbouring crystals. In this case, only part of the energy is deposited in each crystal. This leads to increased Compton background in the γ-ray spectrum and thus worsens the peak-to-total ratio. The photo-peak efficiency and the peak-to-total ratio can be improved by adding the energy deposition from the neighboring crystals together. This process to recover the original energy of scattered γ rays is called add-back. If two crystals containing interaction points of interest share a common boundary, they are considered nearest neighbors and their energy is added. In this approach, the angle of the incident γ ray needed for the Doppler correction is taken from the position of the interaction point with the highest energy deposition.

In in-beam γ-ray spectroscopy, especially with knockout reactions induced by a nuclear target, many prompt γ rays including the in-beam background are emitted in coincidence, making γ-ray multiplicity high. This results in wrong summing of prompt γ rays, and in this situation the absolute add-back efficiency cannot be reliably determined. Therefore, add-back is not used for the extraction of the absolute γ-ray yields and thus for the cross sections in the present analysis. Add-back is used for γ-ray peak identification, γ-γ coincidence analysis, and the extraction of momentum distributions, as it gives higher spectral quality.

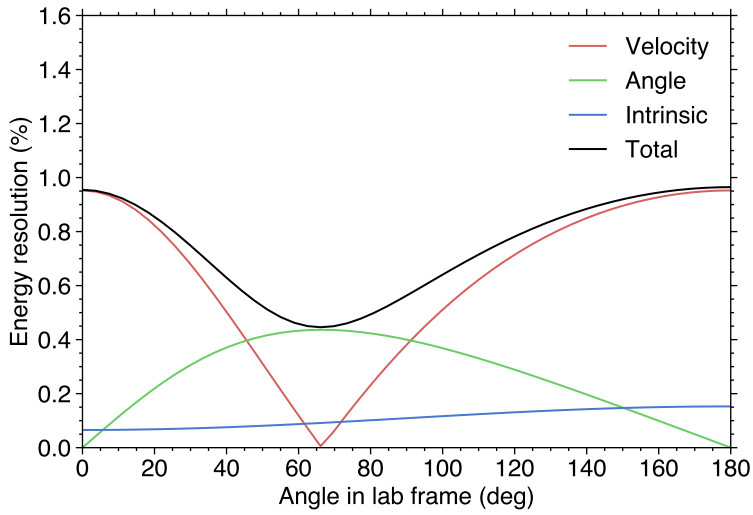

Figure 3.8: Fractional energy resolution resulting from 1-MeV photon in the rest frame and the Doppler correction for $\beta = 0.4$. A velocity uncertainty of 2 %, an angle resolution of 1 mrad, and an intrinsic resolution of 0.1 % have been assumed.

3.3.4 Offline detector characterization

Energy and efficiency calibrations are important for a precise determination of γ-ray energies and intensities. Calibrated γ-ray energies are given by the signal decomposition process, if the calibration parameters were provided. However, it is beneficial to inspect the energy calibrations because of possible gain shifts during the in-beam measurements. Using the calibration data for GRETINA taken with several calibration sources before and after the physics runs, it was confirmed that there were no significant shifts in energy. In the in-beam data analysis, γ-ray energies are always re-calibrated (Figure 3.9), even though the deviations are quite small as compared to typical in-beam energy resolution and accuracy. The linearity of the γ-ray energies was also inspected. The origin of the zigzag pattern appearing in the residual plot (Figure 3.10) can be traced back to the non-linearity of the waveform digitizer, as has been pointed out in [99].

As will be shown in Section 4.4, experimental in-beam γ-ray spectra are fitted by simulated response functions to deduce the absolute γ-ray intensities. Therefore, it is worthwhile to test if the absolute photo-peak efficiency is accurately reproduced by simulations. To determine the photo-peak efficiency, several γ-ray sources were placed at the same position as the target used for an in-beam experiment, 18 cm away from the detector surfaces. For the absolute efficiency, a γ-ray source with a well-characterized activity has to be used. A standard ^{152}Eu source with a calibrated activity of 313.1 kBq (reference date 1 May, 1978) was used for the measurement. An uncertainty in the source activity of 1.4 % was given by the manufacturer. Figure 3.11 shows a measured spectrum of ^{152}Eu in comparison with a simulation by the code UCGretina [102] based on the Geant4 Monte-Carlo package [103]. The measured spectrum is very well reproduced by the simulation. The details on the simulation are described in Section 4.4. The efficiency determination with the ^{152}Eu source is limited roughly up to 1.5 MeV as there are no γ-ray lines above this energy. For the efficiency higher than 1.5 MeV, a ^{56}Co source which provides γ-ray lines up to 3.5 MeV was used additionally. Since the activity of this source is not well known, the intensity was scaled so that the measured efficiency curve

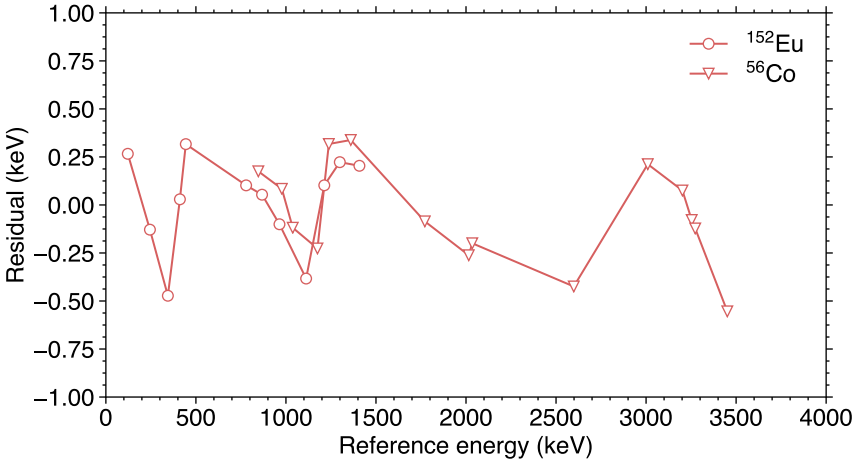

Figure 3.9: Deviations of the recalibrated energies from the reference energies of the standard sources. The zig-zag pattern is originating from the non-linearity of the waveform digitizer.

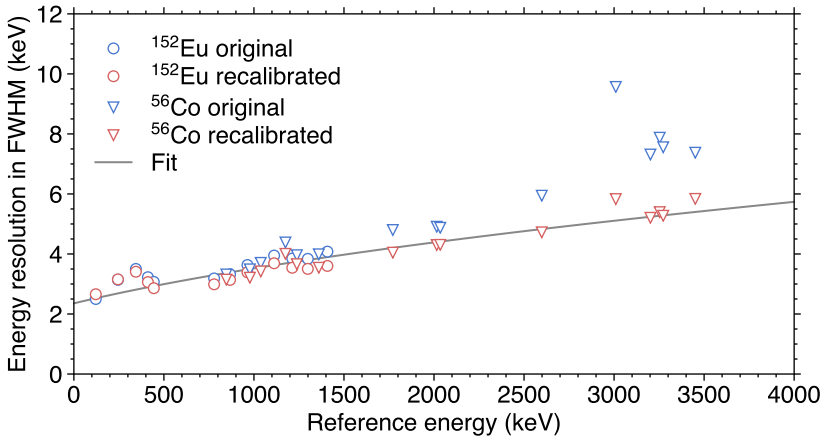

Figure 3.10: Intrinsic energy resolution for a combined spectrum of all the GRETINA crystals. In the in-beam data analysis, the recalibrated γ-ray energies were always used.

is smoothly connected with that of ^{152}Eu. An attempt to deduce the absolute efficiency with this approach is also illustrated in [98], though GRETINA was configured with eight quads in their measurement. The reference γ-ray intensities and energies of all the calibration sources are taken from IAEA [104]. The measured efficiencies are then compared with simulations where monoenergetic γ rays were generated with a 100 keV step. The measured and simulated photo-peak efficiencies are plotted in Figure 3.12. The absolute efficiency is well reproduced by the simulations. This indicates that there is no need for empirical adjustments.

3.4 Electronics and data acquisition

3.4.1 S800 electronics and data acquisition

The detectors of the S800 spectrograph are equipped with a conventional data acquisition system that adopts an event-by-event readout scheme in which a master trigger signal controls the event

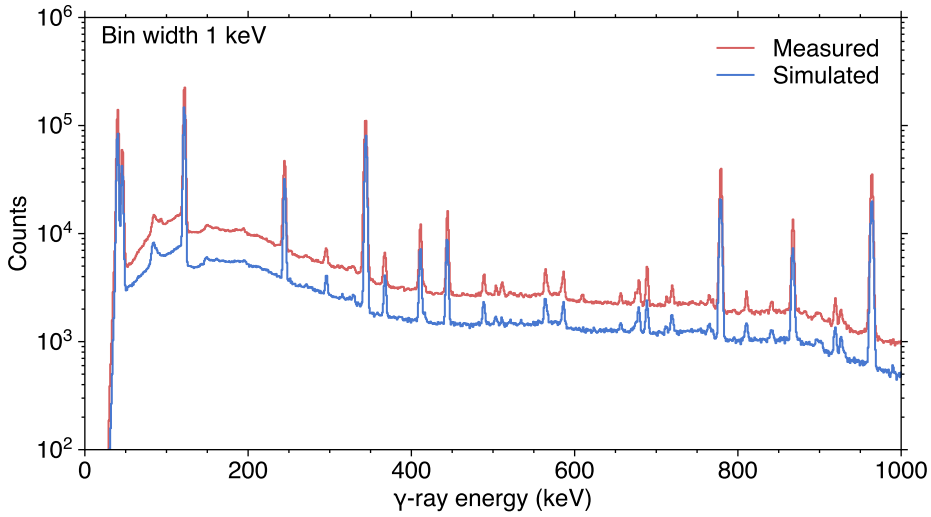

Figure 3.11: Comparison of measured and simulated spectra of γ rays emitted from ^{152}Eu. The measurement was performed using a ^{152}Eu standard source. The data were accumulated for 17 min. The simulated statistics amount to 1×10^6 decay events. The intrinsic resolution and the threshold effect were respectively modeled by $\sqrt{a + bE}$ and $1 + \tanh[(E - c)/d]$ with a, b, c, and d being free parameters to reproduce the spectra.

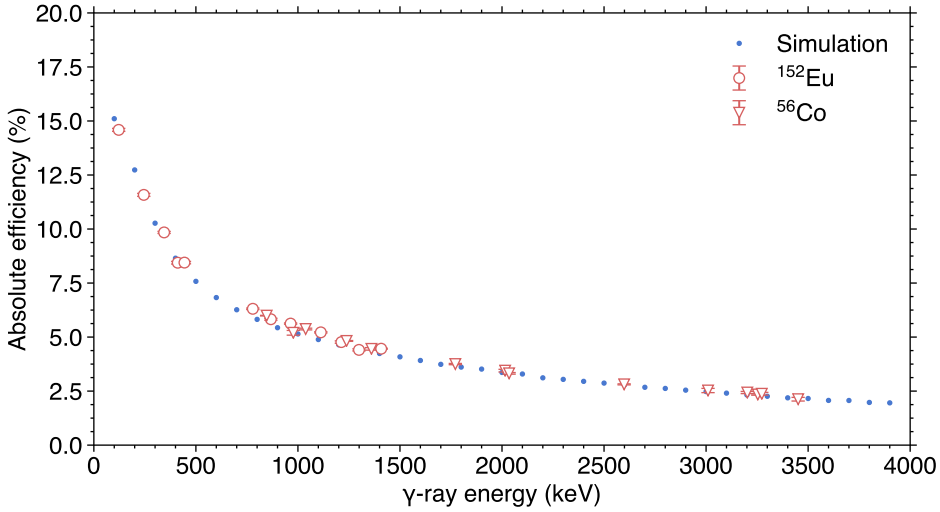

Figure 3.12: Absolute photo-peak efficiency of GRETINA without add-back. The blue points correspond to the measured efficiencies using calibration sources. The red points are taken from simulations where monoenergetic γ rays are generated with an energy step of 100 keV.

readout. To record the timing information of the scintillators and the CRDC anode wires, and the charge information of the ionization chamber, TAC (Time-to-Amplitude Converter) and ADC are implemented in the S800 electronics. Additionally, the scintillator's timing signals are recorded by TDC (Time-to-Digital Converter). A scaler is used to count the input rates of the several trigger sources, the number of generated triggers, and the rates of the scintillators. The

master trigger is generated using the versatile trigger logic which is capable of handling multiple trigger sources. Coincidence conditions between two trigger sources can also be set, and this feature was used for the coincidence of the γ-ray and residual particle detection for the present experiment. The trigger sources used for the present experiment include the GRETINA singles, the downscaled S800 spectrograph, and the coincidence between the S800 and GRETINA. Here the downscaled S800 trigger was taken from the E1 scintillator. Every S800 event is time-stamped using a clock running typically at 20 MHz to correlate the S800 events with those of GRETINA. A typical dead time of the S800 data acquisition is ranging from 120 µs to 200 µs depending on the number of channels to read. This dead time limits the maximum acceptable trigger rate. For the measurement of the dead time, a 10 kHz clock signal vetoed by the DAQ busy signal is recorded using a scaler in addition to a raw clock, and thus the DAQ running time and live time can be calculated.

In the in-beam data collection, the S800 DAQ is triggered by two sources. One is the trigger signal generated by the E1 scintillator, and the other is the coincidence of E1 and GRETINA. This trigger condition ensures that a projectile-like particle is detected at the S800's focal plane. When the rate at the focal plane is low enough, the downscaling of the E1 trigger to reduce the data-taking rate is not necessary. The two trigger sources are simply mixed in this case. For some of the magnetic settings, the E1 trigger signal is downscaled by a factor of 15 or 3 to achieve a moderate data-taking rate. The DAQ is also allowed to run only with the GRETINA singles trigger to take source calibration data.

The CRDCs are equipped with electronics called the STAR front end electronics, which are developed by the STAR collaboration for their time projection chambers. The electronics consist of preamplifiers, shaping amplifiers, switched capacitor arrays, and ADCs. The switched capacitor array samples the waveform of the shaped signal when a trigger is issued and it is digitized by the ADC. The data readout is controlled by an external FPGA-based module that bridges the CRDC and the S800 electronics. The PPACs in the analysis line also adopt the same electronics.

3.4.2 GRETINA electronics

The transient current signals induced on the segmented electrodes and central contact are first integrated by built-in preamplifiers of the GRETINA module. The signals after the amplification are then sent to digitizers [105] to record the waveforms with a sampling frequency of 100 MHz. The recorded signals are time-stamped and stored in the digitizer module locally. The leading-edge timing of the central contact is used to trigger the system. The trigger signal is fed into the GRETINA Trigger Timing and Control logic and the trigger decision is made within the GRETINA electronics. The trigger logic can provide fast trigger outputs and can accept external triggers. This feature is used to link GRETINA with the S800 electronics. When a trigger condition is met, all channels are read out by an event matching process based on time stamps and raw data are transferred to the GRETINA computer farm. The stored data are dropped if a time-stamp matching does not occur within an expiration time. The signal-decomposition software running on the computer gives the position and energy of the interaction point. The GRETINA computer farm is capable of processing 3×10^4 γ-ray events per second. A decomposed event is comprised of the timing and energy of the central contact, the energies of the segmented electrodes, a list of interaction points, and a time stamp. The GRETINA event building software collects event data from the decomposition processes. This software combines

the event data from the S800 data acquisition with the GRETINA events and finally writes them in disk. Note that the GRETINA event builder just orders events according to the time stamps, so it does not build coincidences of the S800 and GRETINA. More technical details on the GRETINA electronics can be found in [105–107].

3.4.3 Event building

For the in-beam data analysis, particle identification is required to associate γ rays with a residual nucleus. As the data acquisition processes of the S800 and GRETINA run independently, S800 (GRETINA) events do not contain γ-ray (beam) information. Nevertheless, by looking at time stamps assigned to every event, it is possible to correlate S800 and GRETINA events to build coincidences of the γ rays and the beam. This process is called the event building.

A conceptual illustration of the event building is shown in Figure 3.13. In the event-building process, one S800 event is correlated with more than one GRETINA events within a given coincidence window based on the time ordering of the events. If a partner is not found within the window, the event is considered as non-coincident. In the data analysis of the present experiment, the event building was performed by a dedicated analysis code GRROOT [108]. The length of the coincidence window was set at 500 time units, corresponding to 5 µs.

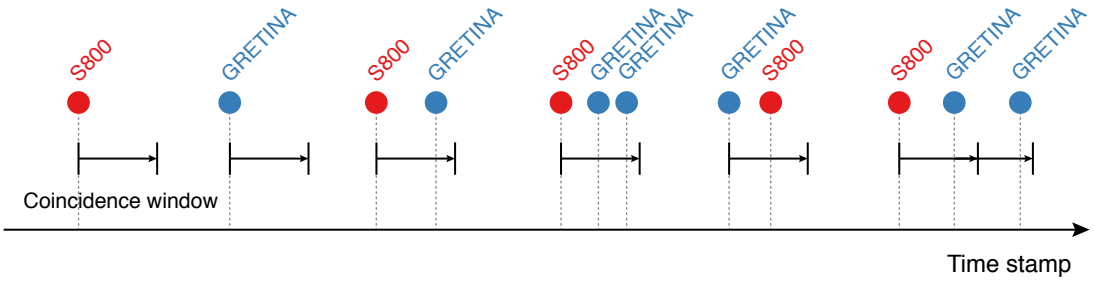

Figure 3.13: Schematic figure showing how the event building works. The circles correspond to events. A coincidence window of a fixed length is opened by either a S800 or GRETINA event. Multiple GRETINA events can extend the window (the rightmost case).

3.5 Summary of measurements

In the present experiment, measurements were performed with three incoming beam settings for the spectroscopy of ^{30}Mg. The first setting is optimized for one-neutron knockout ($-1n$) from ^{31}Mg. The second setting is for two-neutron removal ($-2n$) from ^{32}Mg. The last setting is optimized for two-proton ($-2p$) knockout from ^{34}Si, but this setting also allows for the transmission of ^{30}Mg arising from multi-nucleon removal from ^{34}Si and ^{35}P. The secondary beam intensity can be more than 100 kpps, and this rate is too high for the focal plane detectors to accept. However, because of the limited momentum acceptance of the spectrograph, the unreacted secondary beam is inevitably cut when the magnets are optimized for the transmission of reaction products. This necessitates another magnetic setting dedicated to the measurements of unreacted particles, which gives crucial information needed for the analysis of momentum distributions and cross sections. In this case, the magnetic rigidities up to the S800 analysis line

are kept the same and only the spectrograph's magnetic field is changed. The reaction target does not have to be removed, because the energy straggling effects in the target need to be evaluated experimentally. The magnetic rigidity settings are summarized in Table 3.1. A summary of the beam intensities, run numbers, and total running times is shown in Table 3.2.

In addition to these physics runs, mask calibration data were taken several times to track the time dependence of the calibration whenever the secondary beam setting was switched. Offline measurements for GRETINA were performed before and after the physics runs.

Table 3.1: Magnetic settings for the transmission of the secondary beams of interest. The magnetic rigidities of the A1900 are indicated in units of Tm. The subscripts mean the segment numbers (see Figures 3.1 and 3.2). For instance, $B\rho_{12}$ stands for the common magnetic rigidity of the segment 1 and 2, i.e. the first half of the A1900. The rigidities of the S800, $B\rho_{67}$ for the analysis line and $B\rho_8$ for the spectrograph, are also shown. The momentum acceptance shown here corresponds to the full momentum bite of the A1900 fragment separator.

Secondary beam	Reaction	Momentum acceptance	$B\rho_{12}$	$B\rho_{34}$	$B\rho_5$	$B\rho_{67}$	$B\rho_8$
^{31}Mg	$-1n$	1.1 %	3.94830	3.79332	3.78440	3.77550	3.43220
	unreacted						3.54662
^{34}Si	$-2p$	1.1 %	3.70650	3.52406	3.51020	3.48830	3.52420
	unreacted						3.22870
^{32}Mg	$-2n$	1.1 %	4.10500	3.95130	3.93990	3.92210	3.46300
	unreacted						3.69410

Table 3.2: Secondary beam intensities, run numbers, and total running times of the measurements. The data taking for the ^{31}Mg$-1n$ channel was split into two. The number in the brackets stands for the downscaling factor.

Secondary beam	Reaction	Trigger sources	Run numbers	Total running time
^{31}Mg (first)	$-1n$	S800 (1/15) and GRETINA-S800 coinc.	38–49	10.9 h
^{32}Mg	$-2n$	S800 (1/1) and GRETINA-S800 coinc.	198–232	26.6 h
^{34}Si	$-2p$	S800 (1/3) and GRETINA-S800 coinc.	138–187	36.4 h
^{31}Mg (second)	$-1n$	S800 (1/15) and GRETINA-S800 coinc.	240–249	10.8 h

Chapter 4

In-beam data analysis

The data analysis steps are described in this chapter. First, the calibration of the focal plane detectors and various corrections, which are essential for the particle identification of the incoming radioactive beam and the outgoing reaction products, are described in Section 4.1. The γ-ray analysis, including γ-γ coincidences to build the level scheme, is presented in Section 4.2. The extraction of inclusive cross sections is described in Section 4.3. Details on Monte Carlo simulations to generate GRETINA response functions as a prerequisite for extracting the exclusive cross sections and fits to experimental γ spectra are presented in Section 4.4. Finally, the extraction of the parallel momentum distributions associated with each state in ^{30}Mg is described in Section 4.5.

4.1 Beam transport

This section describes the calibration of the S800 focal plane detectors, their response to the beam particles and reaction products, the necessary corrections, and the particle identification.

4.1.1 Characterization of focal-plane detectors

CRDC calibration

Each of the two CRDCs has 224 individual cathode pads to provide the hit position along the x (dispersive) direction. As described in Section 3.4.1, the CRDC electronics record the waveforms of the shaped signals of each cathode pad, and the net charge deposited in a specific pad is calculated by integrating over all the sampling points. The x position is deduced by taking the center of gravity of the charge distribution. Figure 4.1 shows deduced x position distributions from a ^{31}Mg run after the gain matching of all cathode pads. The cutoff seen at the 35th pad is due to a blocking plate, which is inserted upstream of the S800 focal plane to stop unreacted beam particles.

The y position (non-dispersive direction) is determined by the drift time of electrons. As the drift velocity has been observed to change over time depending on the gas temperature and pressure, mask calibration data were taken intermittently during the experiment. In a calibration run, a metal mask was inserted in front of either the first or second CRDC. The mask plate itself is thick enough for beam particles to stop, but it has many pinholes and slits with known locations to allow for precise calibration. Figure 4.2 shows calibrated x and y positions from

a mask run. To account for the shifts, the y position was calibrated for each secondary beam setting. For the x direction, the position is calculated based on the known pitch of the cathode pads (2.54 mm) and the design position of the central pad. It was confirmed that no further correction is necessary for the x position.

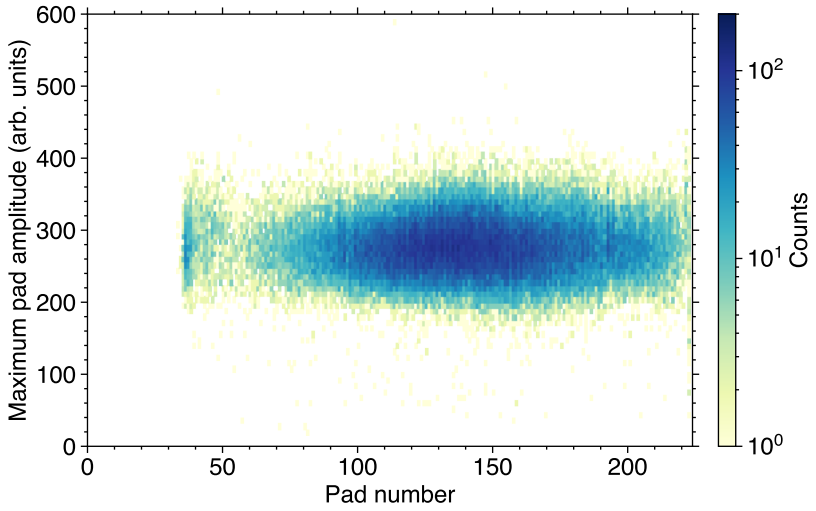

Figure 4.1: Gain-matched cathode pad amplitudes of the first CRDC. The histograms show the maximum amplitude within an event and its pad number. Cuts for incoming ^{31}Mg and outgoing ^{30}Mg have been applied.

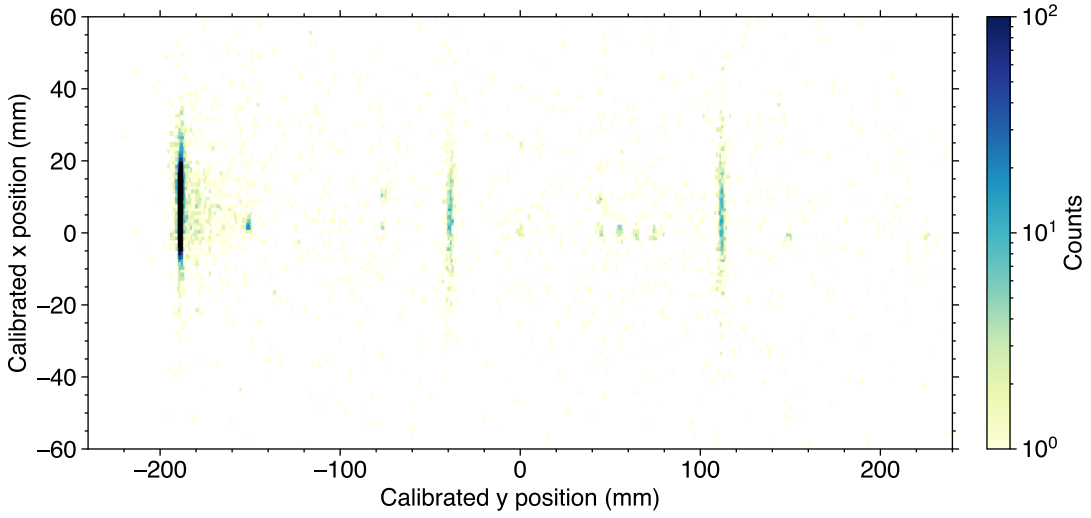

Figure 4.2: Calibrated x and y positions for a mask run of the first CRDC. The calibration is performed using the known positions of holes and slits.

Ionization chamber calibration

As was reviewed in Section 3.2.1, the ionization chamber comprises of 16 individual segments along the beam axis. The energy loss of the reaction product is evaluated by taking the average of the amplitudes of the segments. In order to achieve the best possible resolution, the gain matching of all the segments was performed. By applying rough particle identification cuts for outgoing particles with $Z = 7$ to 12, the calibration parameters for each segment were determined so that the signal amplitudes match the first segment. Figure 4.3 shows the recorded charges and the gain-matched amplitudes.

It was observed that the energy loss ΔE measured in the ionization chamber depends on the hit position of the particle. The x position dependence was empirically corrected by

$$\Delta E' = \Delta E e^{px} \tag{4.1}$$

where p is the fitting parameter. Figure 4.4 shows the x position dependence before and after the correction. No significant dependence was observed along the y direction.

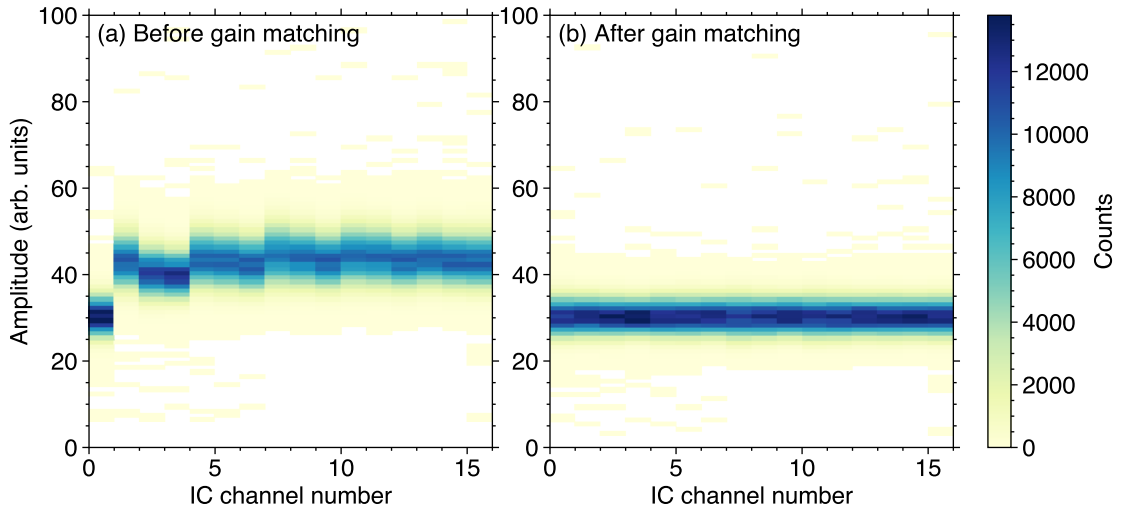

Figure 4.3: Gain matching of the ionization chamber segments. An incoming cut for ^{31}Mg and an outgoing cut for ^{30}Mg have been applied.

Time-dependent corrections

During the ^{34}Si secondary beam runs, large fluctuations in the raw timing of the OBJ scintillator were observed. The fluctuation is likely to originate from changes in the light output due to damages of the scintillator material caused by irradiation of high-intensity secondary beams. During the experiment, the scintillator's position was shifted to recover the light output. This also resulted in jumps in timing. The fluctuation was corrected using a lookup table where the shifts in the OBJ timing are stored as a function of event number. The corrected time dependence is shown in Figure 4.5. In the present experiment, time dependence was not observed for the XFP timing and the signal amplitude of the ionization chamber.

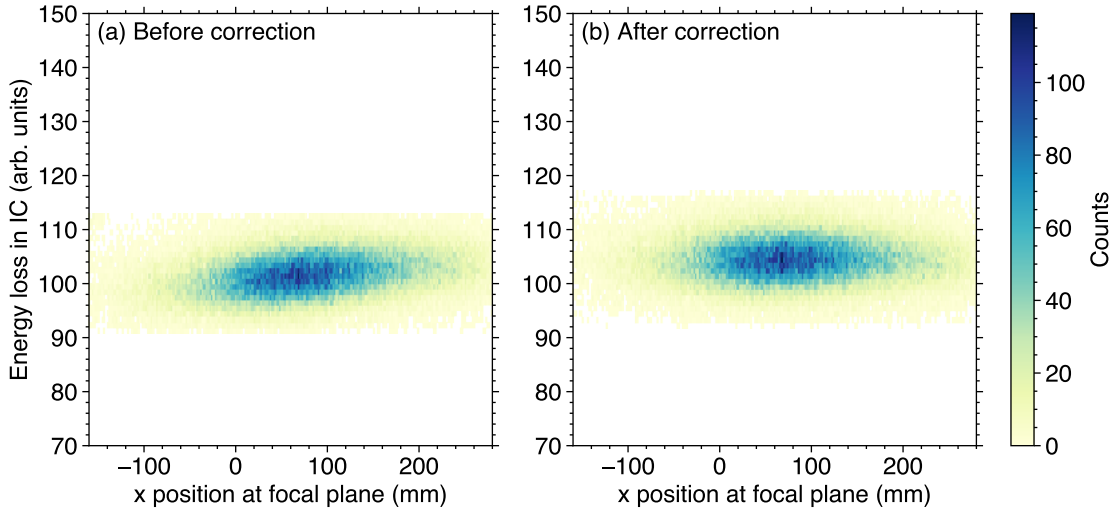

Figure 4.4: Correction for the hit-position dependence of the ionization chamber. The original energy loss measured in the ionization chamber and the energy loss empirically corrected by Equation (4.1) are respectively shown in the panels (a) and (b). Rough cuts for incoming ^{31}Mg and outgoing ^{30}Mg have been applied.

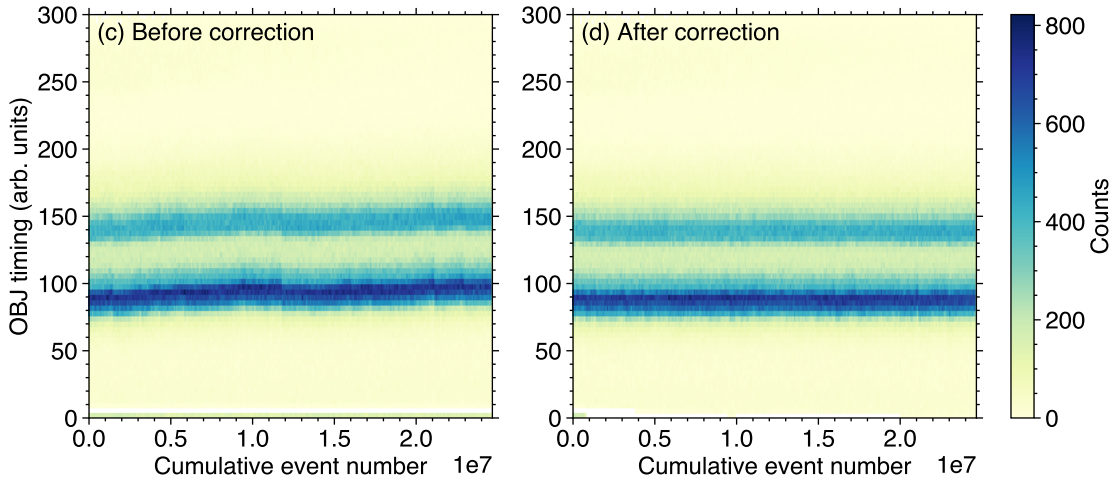

Figure 4.5: Time dependence of (a) the raw timing signal measured by the OBJ scintillator and (b) the corrected timing for runs taken with the ^{34}Si secondary beam setting. The band at around 90 and 140 respectively contain reaction products originating from ^{34}Si and ^{35}P.

TOF corrections

As discussed in Section 3.2.3, different flight paths in the S800 spectrograph lead to a variation in the measured TOF. The correction for the particle trajectory is performed empirically by, to first order,

$$t'_{\mathrm{out}} = t_{\mathrm{out}} + C_1 x_{\mathrm{fp}} + C_2 a_{\mathrm{fp}} \tag{4.2}$$

where t_{out} is the measured time difference between OBJ and E1. C_1 and C_2 are parameters that minimize the variation in t'_{out} for a specific reaction channel. This correction is the most important of all. Without this correction, particle identification for outgoing particles would not be possible. To determine C_1 and C_2, first the TOF is corrected for its dependence on the focal plane position x_{fp} only by varying C_1. The optimum C_1 is obtained by tilting the two-dimensional histogram of the position versus corrected TOF of Equation (4.2) and minimizing the width. With this pre-determined C_1, the same tilting and minimization process is performed for the dispersive angle a_{fp} varying only C_2. This procedure needs to be iterated until both C_1 and C_2 converge. The TOF-x_{fp} and TOF-a_{fp} correlation plots before and after the correction are compared in Figures 4.6 and 4.7. The resulting particle identification plot for incoming ^{30}Mg is shown in Figure 4.8 together with a plot produced without the correction. It is clear that isotopes are not separated without the TOF correction.

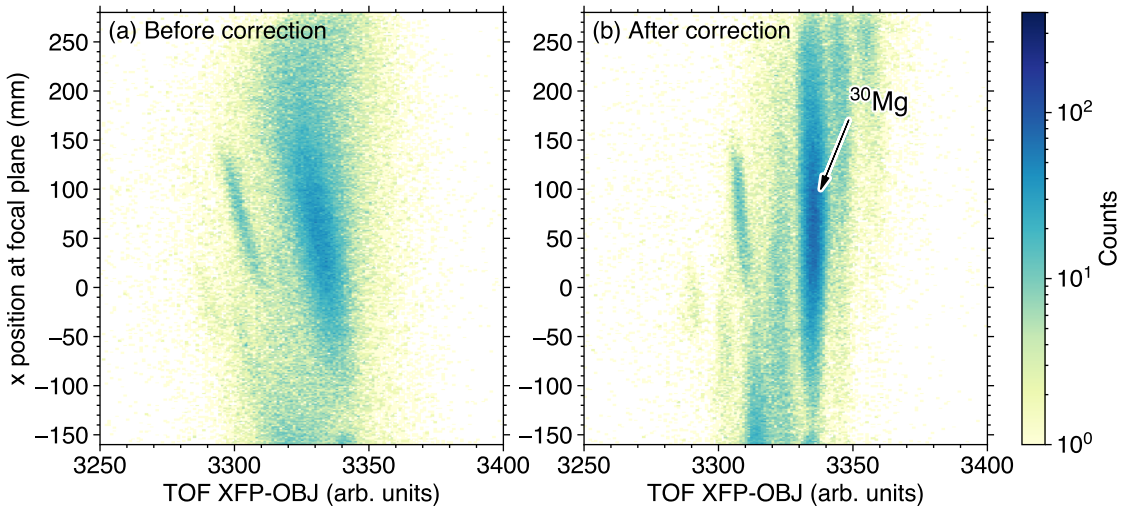

Figure 4.6: TOF correction for position in the focal plane x_{fp}. The panels (a) and (b) respectively display the correlations of TOF and x_{fp} before and after the correction. An incoming cut for ^{31}Mg has been applied.

4.1.2 Particle identification of incoming and outgoing particles

The TOF measurements of XFP-E1 and OBJ-E1 are used for particle identification of the incoming beam, while the combination of the OBJ-E1 TOF after the correction discussed above and the energy loss measured in the ionization chamber provides identification of the outgoing particles.

Unreacted secondary beam

Prior to the in-beam γ-ray measurements, the secondary beam was directed to the S800 spectrograph with the magnetic rigidity setting optimized for the transmission of particles that do not react in the target. This is called the unreacted beam setting. The incoming and outgoing particle identification plots for ^{31}Mg are shown in Figure 4.9. The unreacted beam is mainly

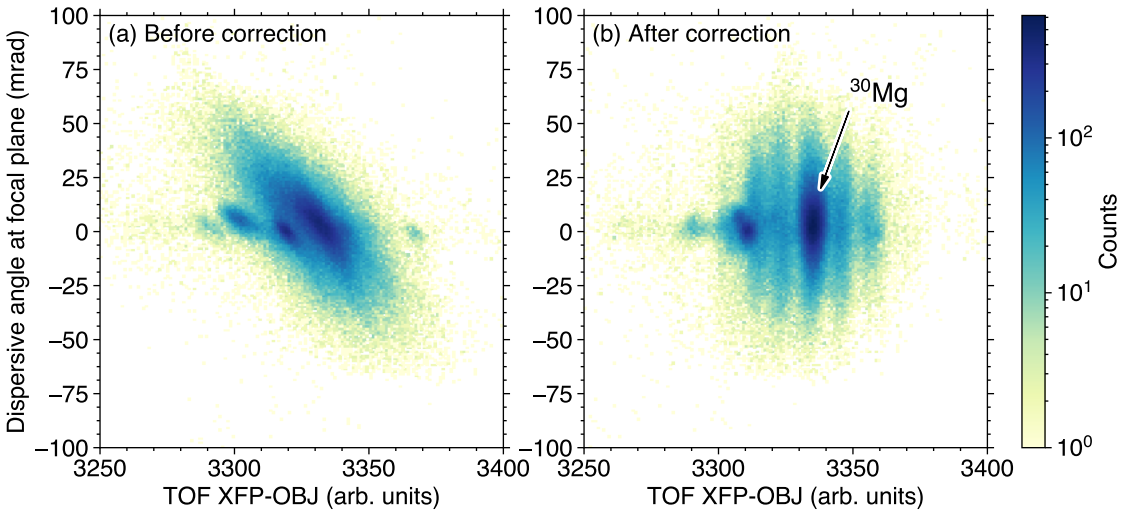

Figure 4.7: Same as Figure 4.6 but for angle in the focal plane a_{fp}.

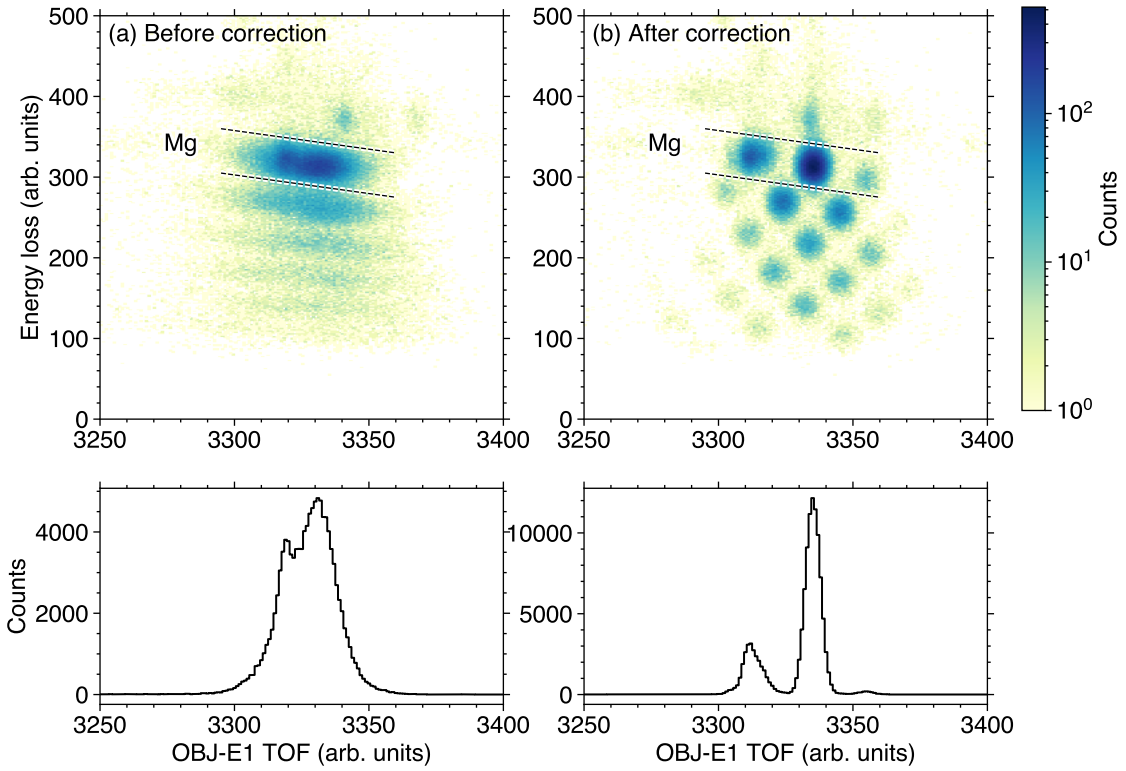

Figure 4.8: Particle identification plots for the outgoing particles with an incoming cut for ^{31}Mg. (a) Without the TOF correction isotopes are not separated. (b) Complete separation is achieved with the correction. The bottom panels show the TOF histogram with a gate on Mg isotopes.

used for the normalization of the beam intensity on target. When the S800 is optimized for the

reaction products, the beam intensity can be monitored only by using the counting rates of the XFP and OBJ scintillators. Therefore, a scaling factor to reproduce the on-target beam intensity is required for the extraction of cross sections. The scaling factor should take into account the beam transmission from XFP or OBJ to the target, the fraction of the incoming isotope of interest, and the detection efficiency of the S800 focal plane detectors. Thus, the scaling factor f_{scale} is given by

$$f_{\mathrm{scale}} = f_{\mathrm{purity}} f_{\mathrm{trans}} \epsilon_{\mathrm{FPD}} = \frac{N_{\mathrm{out}}}{N_{\mathrm{beam}} \epsilon_{\mathrm{DAQ}}} \tag{4.3}$$

where N_{out} is the number of ^{30}Mg ions counted at the S800 focal plane, and N_{beam} is the number of total beam particles taken from the OBJ or XFP scintillator. ϵ_{DAQ} is evaluated using the ratio of the measured live-time and real-time obtained from a clock running at 10 kHz.

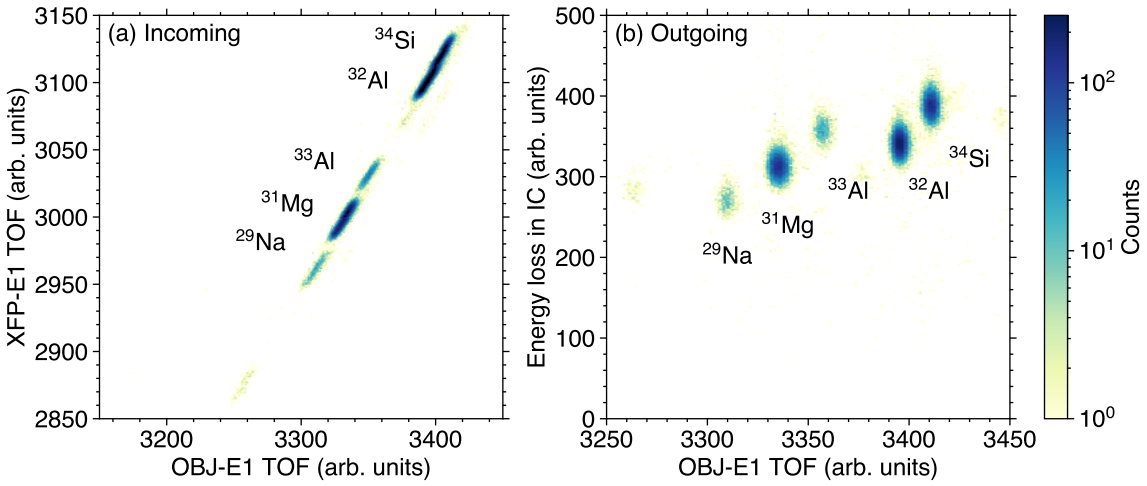

Figure 4.9: Particle identification plots for (a) incoming and (b) outgoing particles with the S800 centered on unreacted ^{31}Mg.

Reacted secondary beam

For the in-beam γ-ray measurements, only the reaction products are directed to the S800 focal plane. Unreacted beam particles are stopped in the beam pipe or in the beam stopper in front of the focal plane, but a small portion of them can still reach the focal plane. The particle identification plot for reaction products in the ^{31}Mg setting is shown in Figure 4.10 Particle identification cuts are also drawn. The incoming particle identification plots look very different from those of the unreacted beam because of TOF spreads in OBJ-E1 and XFP-E1. However, this does not change the incoming particle identification, as only the time difference between OBJ and XFP matters.

Contamination due to scattered particles

It was observed that the outgoing particle identification for the ^{32}Mg two-neutron removal setting was contaminated by scattered ^{32}Mg and ^{31}Mg ions. Even though the exact location

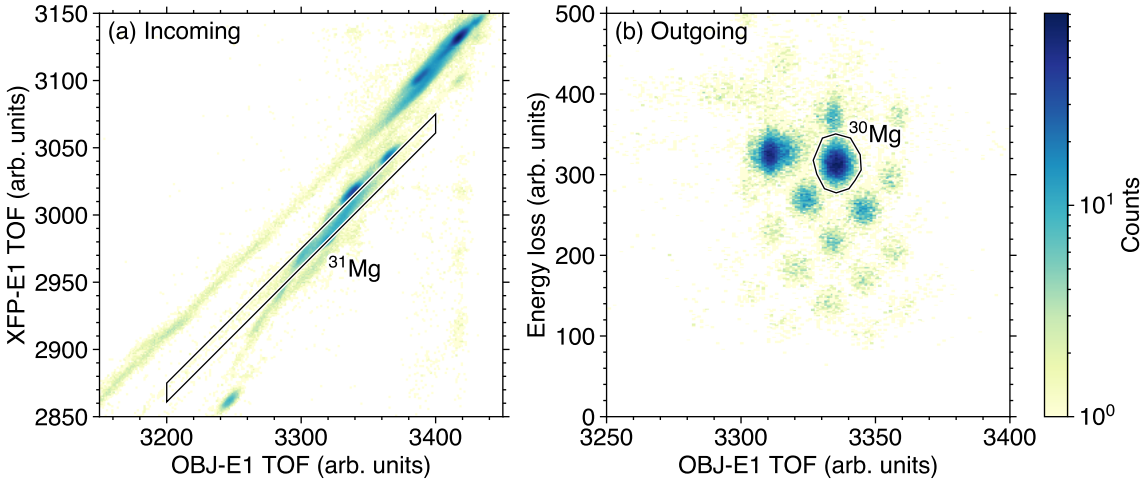

Figure 4.10: Particle identification plots for (a) incoming particles and (b) outgoing particles with the S800 centered on reacted ^{30}Mg taken from a single run. The incoming and outgoing cuts are also indicated.

where scattering takes place has not been identified, it is thought to originate from some place near the focal plane, as previously observed in a different experiment [109, 110]. Scattered particles appear as strongly correlated loci in the two-dimensional plot of the position and angle measured at the focal plane (a_{fp} and x_{fp}) and it was confirmed that this is the case only for the ^{32}Mg setting. As can be seen in Figure 4.11, the plot is contaminated by strongly correlated loci localized in the high-momentum side. To clean up the particle identification for outgoing ^{30}Mg, an additional cut was applied as shown in the figure.

4.2 γ-ray analysis

The particle identification cuts defined in the previous section allow for the clear selection of a specific reaction channel. This section describes γ-ray analysis of four reaction channels populating ^{30}Mg: one-neutron knockout from ^{31}Mg, two-neutron removal from ^{32}Mg, and multi-nucleon removal from ^{34}Si and ^{35}P.

4.2.1 Singles γ-ray spectra

Prior to the γ-ray analysis, non-prompt γ-ray hits are rejected to reduce uncorrelated background in the γ-ray spectra. Figure 4.12 shows the correlation between the γ-ray energy and the hit timing relative to the trigger signal. The structure seen around -265 ns corresponds to the prompt γ rays, while the rest are the non-prompt γ rays. A γ-ray timing cut was defined as shown in the figure. The same timing cut was used for the analysis of all the reaction channels.

As previously mentioned in Section 3.3.2, the Doppler correction is performed event-by-event based on the measured γ-ray energy, the opening angle between the residue and the γ ray, and the velocity β. The residual's velocity after the target can be easily calculated from the d_{ta} measurement in the focal plane (see Section 3.2.2). However, as the γ-ray emission

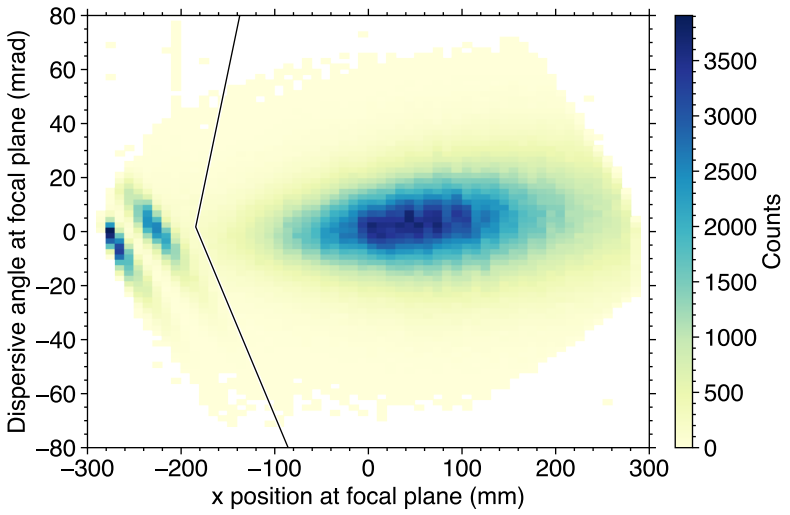

Figure 4.11: Correlation plot of the position and angle in the focal plane created by gating on incoming ^{32}Mg and outgoing ^{30}Mg. The main blob centered at around 50 mm corresponds to ^{30}Mg, while structures originating from scattering of ^{32}Mg and ^{31}Mg are seen around −250 mm. An additional cut was defined for a cleaner separation.

takes place on average in the middle of the target for sufficiently short-lived transitions, the mid-target velocity that should enter the Doppler correction is different from the post-target velocity. The event-by-event β for the Doppler correction is calculated based on the d_{ta} measurement introducing the reference velocity β_{ref}:

$$\beta \approx \beta_{\mathrm{ref}} \left(1 + \frac{d_{\mathrm{ta}}}{\gamma_{\mathrm{ref}}(1+\gamma_{\mathrm{ref}})}\right) \tag{4.4}$$

where $\gamma_{\mathrm{ref}} = 1/\sqrt{1-\beta_{\mathrm{ref}}^2}$ is the Lorentz factor. To determine the optimum reference velocity, β_{ref} is varied to minimize the width of a Doppler-corrected γ-ray peak in the spectrum. The reference velocity for one-neutron knockout from ^{31}Mg was determined to be $\beta_{\mathrm{ref}} = 0.415$ minimizing the width of the peak at 3541 keV. The 3541-keV transition is expected to be very short-lived as the lifetime is inversely proportional to E^{2L+1} for a transition multipolarity of L, and thus the shift in the peak position is likely to be small.

For the identification of γ-ray peaks, add-back is utilized to improve on the spectral quality. This is particularly important for the identification of weak γ-ray transitions. The algorithm of add-back used in this work is described in Section 3.3.3. The improvement in the peak-to-total ratio is demonstrated in Figure 4.13. Doppler-corrected add-back γ-ray spectra populating excited states in ^{30}Mg resulting from one-neutron knockout from ^{31}Mg, two-neutron removal from ^{32}Mg, and multi-nucleon removal from ^{34}Si and ^{35}P are shown together in Figure 4.14. The transitions observed in the previous one-neutron knockout measurement [48] are clearly seen. The identification of peaks with small intensities was guided by known γ-ray energies from previous β-γ measurements [51, 55].

Most of the transition energies were determined by Gaussian fits to the peaks in the Doppler-corrected add-back spectrum of one-neutron knockout from ^{31}Mg in this work independently. The energies of the peaks lying higher than 3400 keV were, if observed, with few exceptions,

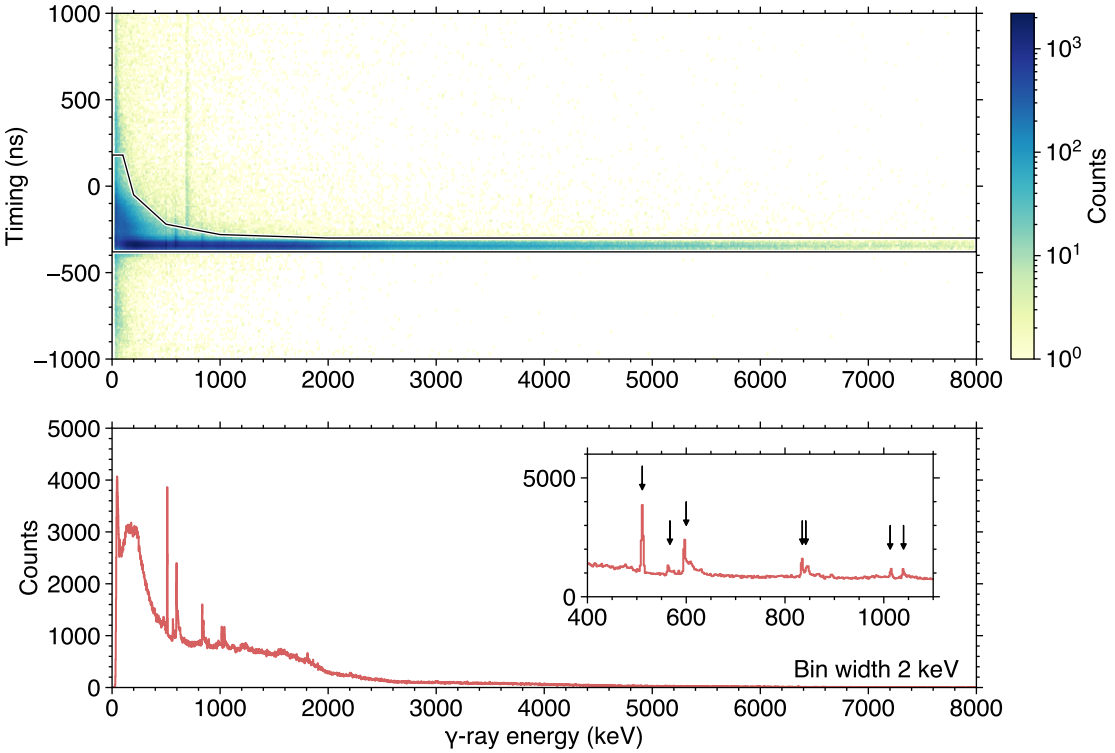

Figure 4.12: Correlation between measured lab-frame γ-ray energies and timings for one-neutron knockout from ^{31}Mg. A timing cut to reject non-prompt γ rays is overlayed. A projection is shown in the bottom panel. The annihilation peak at 511 keV and peaks associated with neutron-induced reactions are indicated by the arrows (see Table 4.1 for details).

taken from the results of a β-γ measurement consistently [55]. Some of the peaks are not observed in the spectrum of ^{31}Mg. In this case, the transition energies were determined using the spectra of ^{32}Mg or ^{35}P. The observed transitions and their energies are listed in Table 5.1.

4.2.2 γ-γ coincidence analysis

The γ-γ coincidence analysis is an effective tool for placing transitions into the level scheme. In this analysis, all the combinations of γ-ray hits within the coincidence window are filled in a two-dimensional histogram to create the so-called γ-γ matrix. For instance, when three γ rays with energies E_1, E_2, and E_3 are detected in coincidence, six combinations of hits, i.e. (E_1, E_2), (E_2, E_3), (E_3, E_1), (E_2, E_1), (E_3, E_2), and (E_1, E_3) are filled in the histogram and thus the resulting matrix is automatically symmetrized. The γ-γ matrices produced from the one-neutron knockout reaction from ^{31}Mg and the two-neutron removal reaction from ^{32}Mg are shown in Figure 4.15. The γ-γ matrix produced from the fragmentation of ^{35}P and ^{34}Si is shown in Figure 4.16. Note that the coincidence window being used in this work is identical to the timing cut defined in Figure 4.12. From the γ-γ matrix, one can produce a one-dimensional projection by gating on a specific transition. To suppress coincidences originating from Compton scattering events, the background contribution has to be handled carefully. In the present analysis, one-dimensional

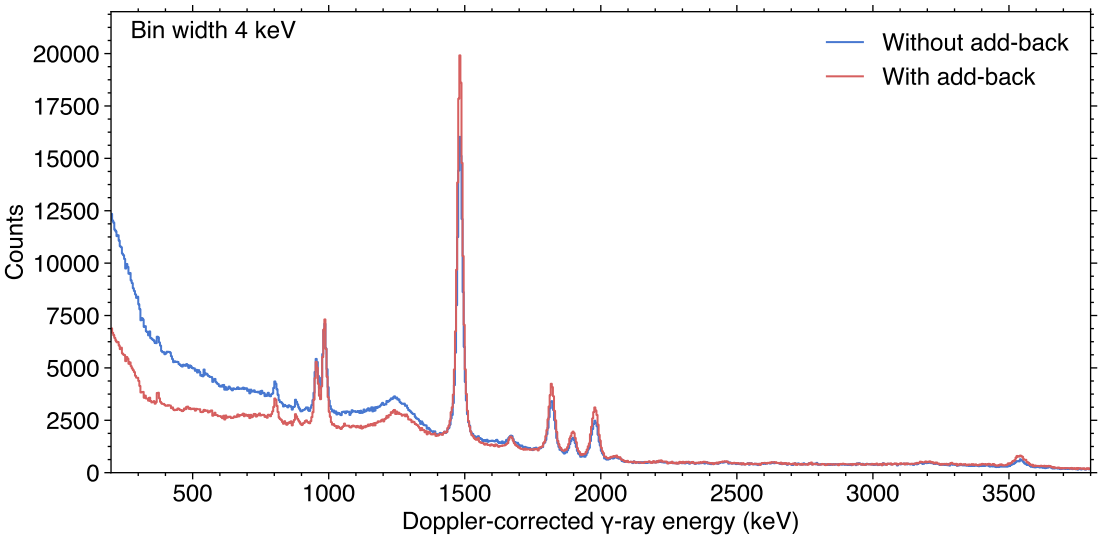

Figure 4.13: Comparison of Doppler-corrected γ-ray spectra with and without add-back, respectively shown in red and blue. Peaks are more pronounced in the add-back spectrum owing to the improved peak-to-total ratio. The spectra are taken from the one-neutron knockout reaction from ^{31}Mg.

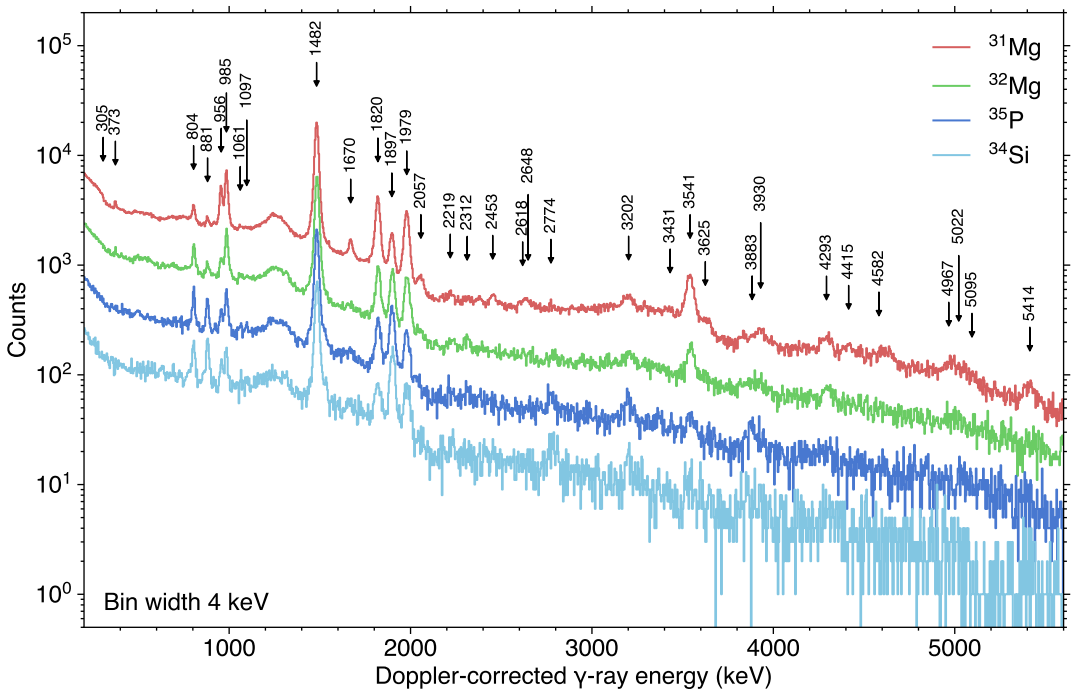

Figure 4.14: Doppler-corrected add-back γ-ray spectra detected in coincidence with ^{30}Mg, resulting from four different reaction channels: one-neutron knockout from ^{31}Mg (red), two-neutron removal from ^{32}Mg (green), and multi-nucleon removal from ^{34}Si (cyan) and ^{35}P (blue). Arrows represent identified γ-ray transitions and energies. The reaction-channel dependence of the population of states is clearly seen.

projections beside the region of interest with proper weighting factors were used to account for the background. One-dimensional projections of the γ-γ matrices after the background subtraction are shown in Figures 4.17 and 4.18. The observed coincidences are summarized later in Table 5.2.

4.3 Inclusive cross sections

The inclusive cross section, i.e. the sum of cross sections to populate all particle-bound states in ^{30}Mg including the ground state, is given by

$$\sigma_{\mathrm{incl}} = \frac{N_{\mathrm{out}}}{N_{\mathrm{in}} n_{\mathrm{targ}} \epsilon} \tag{4.5}$$

where N_{out} is the number of ^{30}Mg ions detected at the S800 focal plane, N_{in} is the number of incoming particles on target, n_{targ} is the areal number density of the reaction target ($2.51 \times 10^{22}\,\mathrm{cm}^{-2}$ in the present experiment), and ϵ is the correction factor that accounts for the efficiency of the system. N_{out} is obtained by counting the number of events contained in the outgoing particle identification cut shown in Figure 4.10. N_{in} is taken from the number of counts of the OBJ or XFP scintillator and the scaling factor of Equation (4.3) that accounts for the transmission and purity. Note that the detection efficiency of the S800 focal plane detectors is already included in this factor. For consistency, the number of counts in OBJ is used for all reaction channels. The efficiency ϵ is decomposed into two parts: the DAQ efficiency ϵ_{DAQ} that accounts for the deadtime of DAQ, and the correction factor ϵ_{S800} for the finite momentum acceptance of the S800. The latter was taken to be unity as the full momentum distribution was covered by the acceptance of the S800. For the data taken with mixed trigger sources, an additional condition where the data acquisition is triggered by the downscaled E1 scintillator (the "S800 trigger") was applied when counting the number of events. In this case, N_{out} should be multiplied by the downscaling factor f_{DS}.

The total uncertainty of the inclusive cross section contains the statistical error of the number of the detected particles and the systematic uncertainty originating from the target thickness and the secondary beam composition. The tolerance of the target thickness is estimated as 1 % [110]. Fluctuations in the secondary beam composition were found to largely impact the inclusive cross section. As can be seen in Figure 4.19, the fluctuations are visualized by calculating inclusive cross sections on a run-by-run basis. The inclusive cross section was taken from the weighted average of all the data points, and the uncertainty due to these fluctuations was estimated by taking the RMS deviation from the averaged value.

The cross sections for the ^{34}Si and ^{35}P channels have to be considered as lower limits, since the S800 was not optimized for the transmission of ^{30}Mg. Significant cuts in the momentum acceptance did not allow for the reconstruction of the missing components. The acceptance cuts are shown in Figure 4.20.

The resulting inclusive cross section for one-neutron knockout from ^{31}Mg is 97(3) mb. The previous experiment employing the same reaction reported an inclusive cross section of 90(12) mb [48]. This value agrees with the present cross section within the quoted uncertainty. The inclusive cross section for two-neutron removal from ^{32}Mg is determined to be 108(2) mb. This value is larger than that of one-neutron removal from ^{31}Mg. Even if more nucleons are removed, it does not necessarily mean that the cross section becomes smaller. One possible

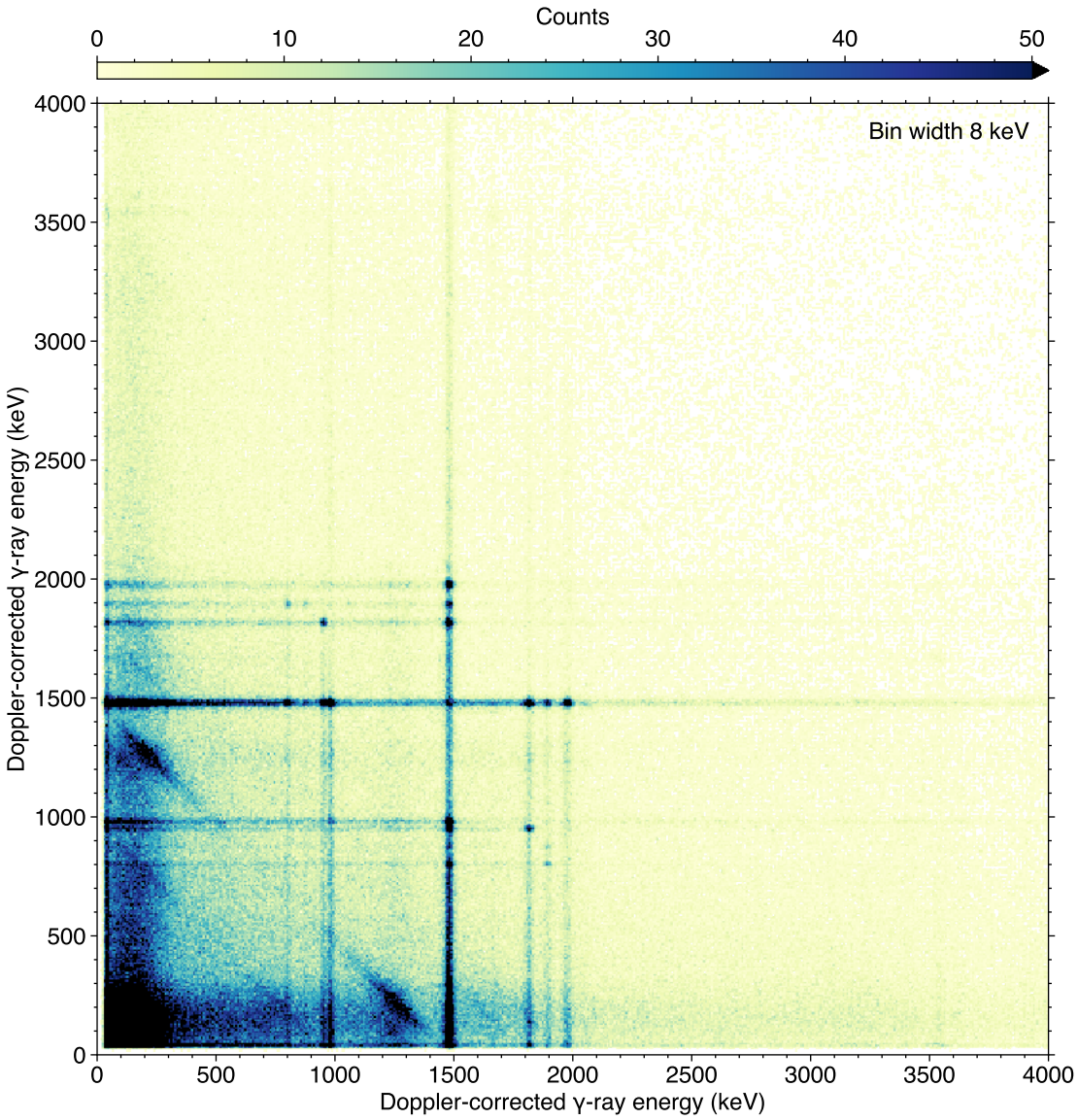

Figure 4.15: Doppler-corrected add-back γ-γ coincidence matrix for the decay of excited states in ^{30}Mg. γ-γ matrices resulting from the one-neutron knockout reaction from ^{31}Mg and the two-neutron removal reaction from ^{32}Mg are added together to gain statistics.

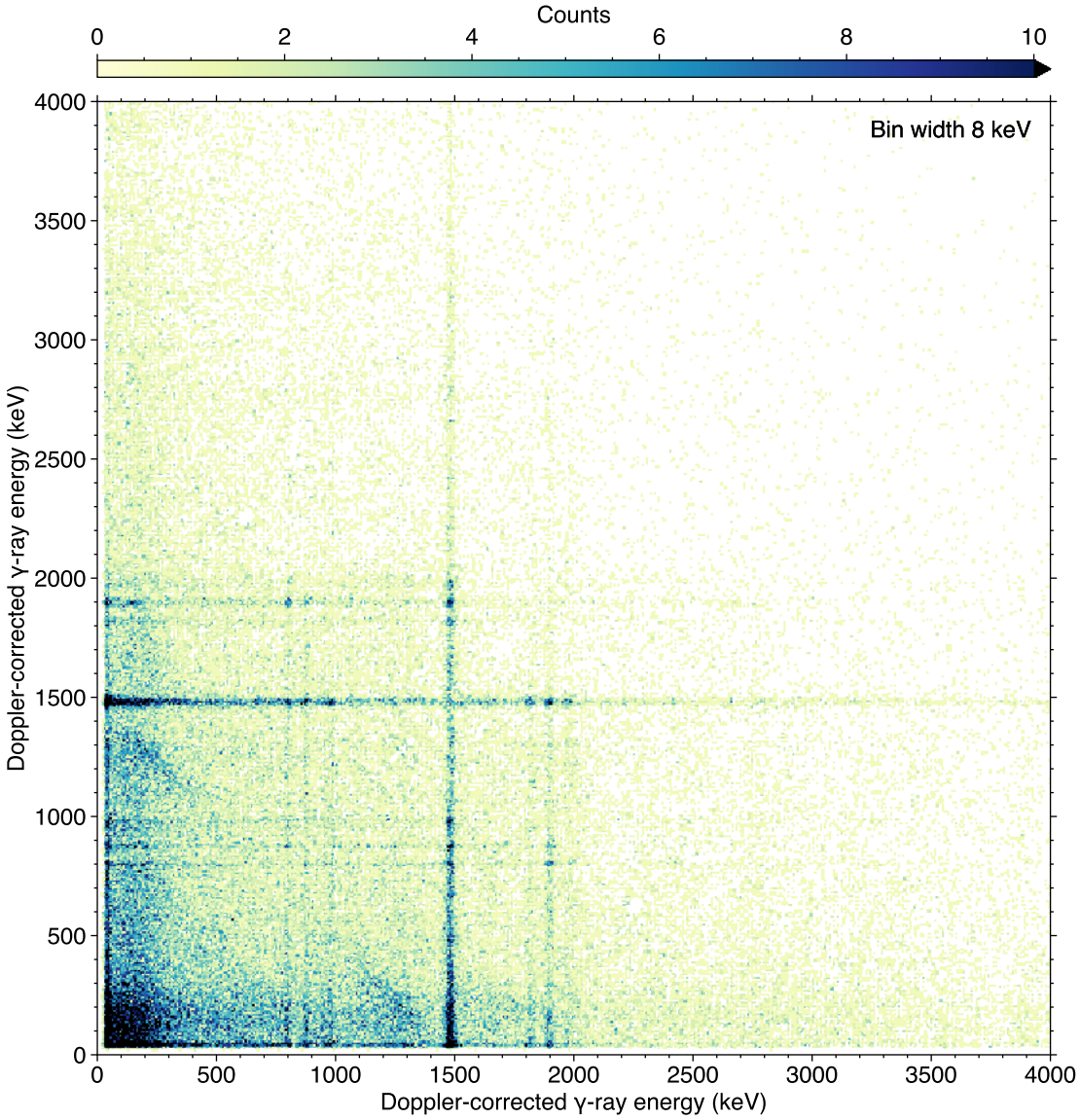

Figure 4.16: Same as Figure 4.15, but γ-γ matrices resulting from the fragmentation of ^{35}P and ^{34}Si are added together.

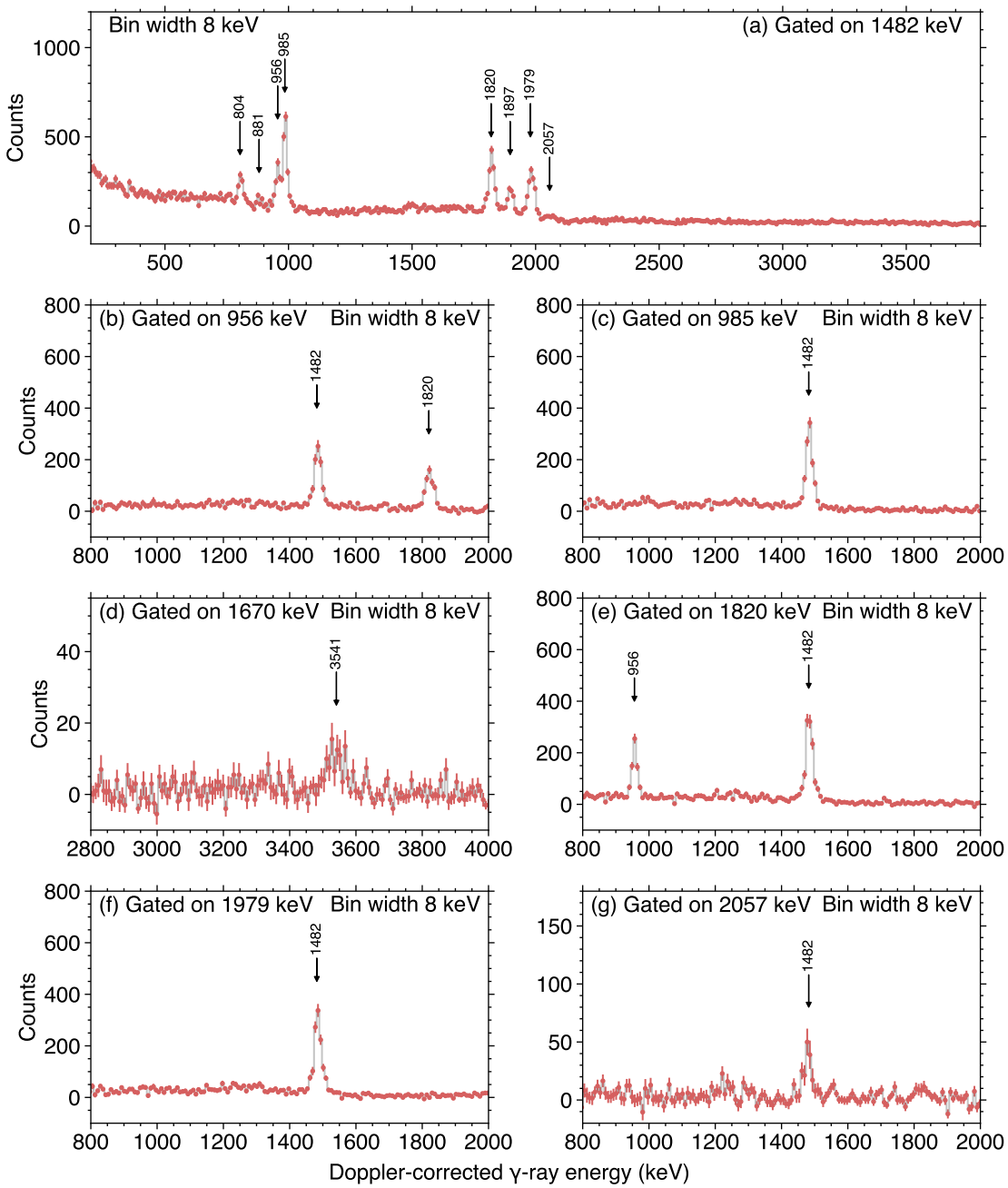

Figure 4.17: Background-subtracted one-dimensional projections of the γ-γ matrix of the ^{31,32}Mg neutron removal data (see Figure 4.15) obtained by gating on (a) 1482 keV, (b) 956 keV, (c) 985 keV, (d) 1670 keV, (e) 1820 keV, (f) 1979 keV, and (g) 2057 keV.

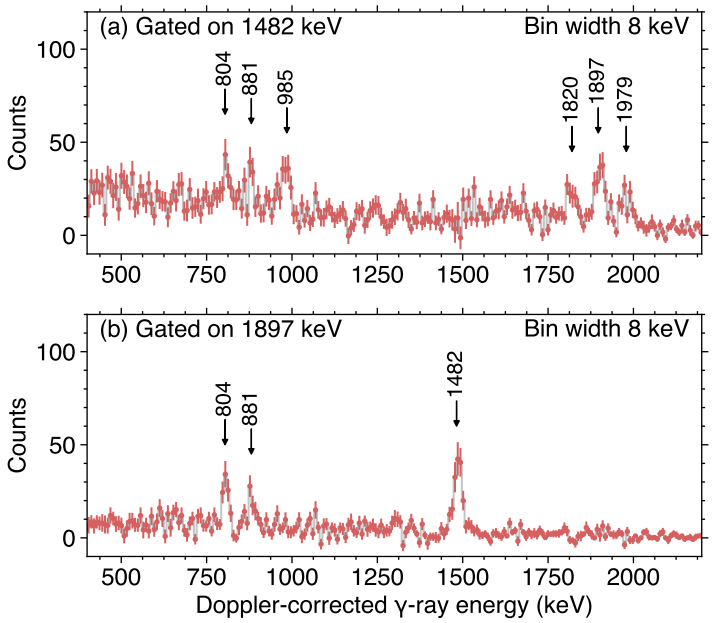

Figure 4.18: Background-subtracted one-dimensional projections of the multi-nucleon removal from ^{34}Si and ^{35}P (Figure 4.16) obtained by gating on (a) 1482 keV and (b) 1897 keV.

reason is that two-neutron removal reactions on neutron-rich nuclei are largely dominated by indirect processess. In fact, relative enhancements in cross sections of two-nucleon removal and also the "even-odd staggering" behavior have been observed for heavier systems [111].

4.4 Exclusive cross sections

The knockout cross section to populate a specific state in the residual nucleus is called the partial cross section or the exclusive cross section. This cross section is one of the most important observables in knockout reactions, as it carries structural information that can be directly compared with theories. The exclusive cross section can be related to the inclusive cross section by

$$\sigma_i = \sigma_{\text{incl}} P_i = \frac{N_{\text{out}} P_i}{N_{\text{in}} n_{\text{targ}} \epsilon} \tag{4.6}$$

where the index i labels an excited state and P_i is the probability of populating that state directly in the reaction. The population of a specific state is calculated from the balance of absolute γ-ray intensities I_i that depopulate and feed the state,

$$P_i = \sum_{\text{depop}} I_i - \sum_{\text{feed}} I_i, \tag{4.7}$$

and the remaining strength is assumed to correspond the ground state

$$P_{\text{gs}} = 1 - \sum_i P_i. \tag{4.8}$$

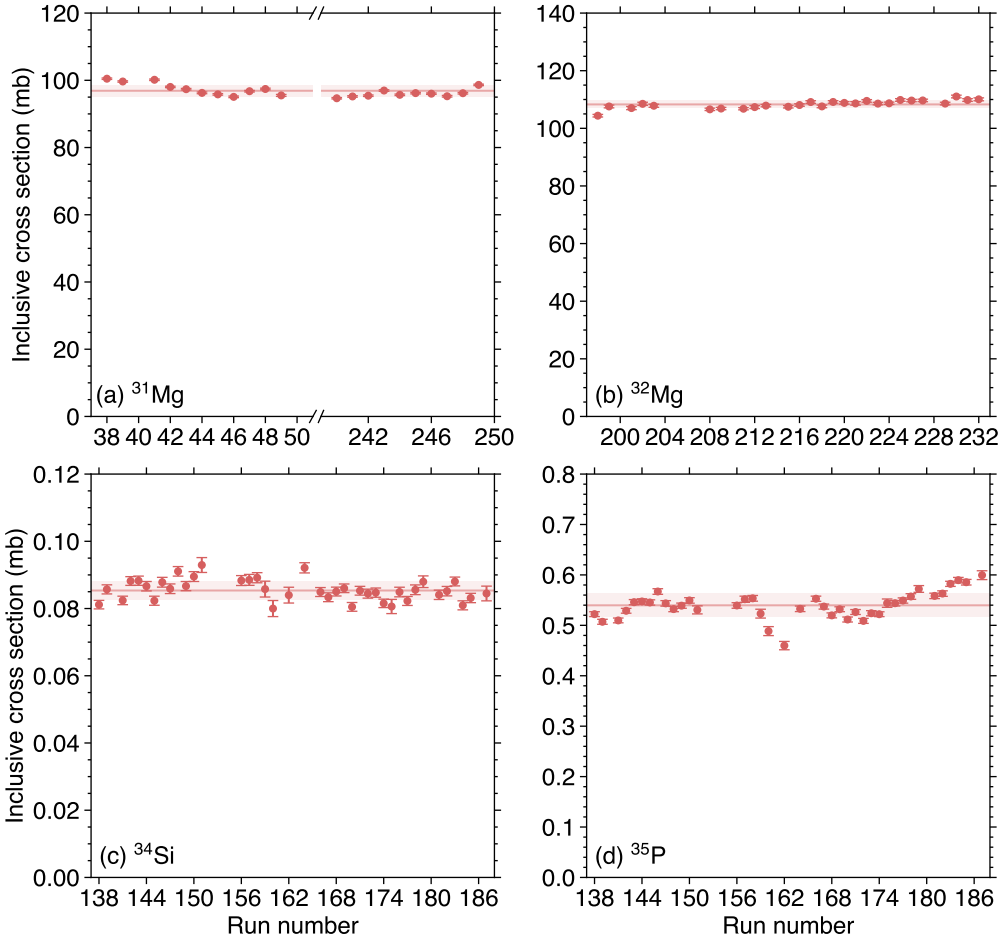

Figure 4.19: Cross sections to all bound states for the one-neutron knockout reaction on (a) ^{31}Mg, the multi-nucleon removal reactions on (b) ^{32}Mg, (c) ^{34}Si, and (d) ^{35}P presented on a run-by-run basis. The errorbars are statistical only. The horizontal line shows the weighted mean of all the data points, and the band indicates the uncertainty evaluated by taking RMS relative to the mean.

The uncertainty associated with each population probability ΔP_i is calculated by adding the uncertainties of the γ-ray intensities in quadrature by

$$(\Delta P_i)^2 = \sum_{\text{depop}} (\Delta I_i)^2 + \sum_{\text{feed}} (\Delta I_i)^2 \tag{4.9}$$

where the uncertainty of intensities ΔI_i are taken from fits to the γ-ray spectrum (see Section 4.4.1). In the present analysis, the lifetime uncertainty of the 305 keV transition (3.9(4) ns [53]) also impacts the γ-ray yield and needs to be taken into account. The uncertainty in the inclusive cross section described in Section 4.3 propagates to the uncertainty in the exclusive cross sections through Equation (4.6). Additionally, an uncertainty in the γ-ray absolute efficiency (estimated to be 3 %) is taken into account. It should be noted that the cross sections are calculated under the assumption that all the transitions are observed and correctly placed in the level scheme.

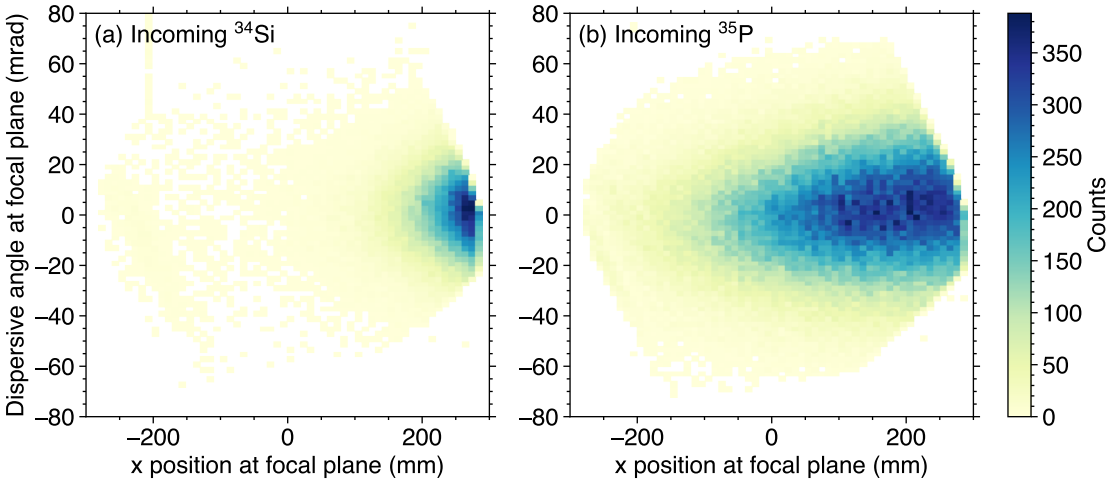

Figure 4.20: Correlation plots of the angle and position measured at the focal plane for outgoing ^{30}Mg gated on incoming (a) ^{34}Si and (b) ^{35}P. Cuts of outgoing ^{30}Mg, roughly >90 % for incoming ^{34}Si and >50 % for incoming ^{35}P, due to the finite acceptance of the S800 spectrograph are seen.

4.4.1 Simulations of GRETINA response functions

To deduce the γ-ray intensities, the in-beam γ-ray spectrum was fitted using simulated GRETINA response functions. The detector response to γ rays emitted in flight was simulated by the same framework used for the source simulations presented in Section 3.3.4. The simulations employ the code UCGretina [102] and the Geant4 Monte Carlo simulation package [103]. The simulation includes segmented germanium crystals and their housing, cryostats and mounting frames, the aluminum beam pipe, the quadrupole magnet and gate valve of the S800 spectrograph, and the secondary target. The materials included in the simulation are shown in Figure 4.21. For in-beam simulations, first the characteristics of the incoming beam, such as the momentum spread and the beam profile on target, were adjusted to reproduce the experimental lineshape. The energy loss of the beam and reaction residue through the target is also implemented in the simulation.

The Doppler correction assumes the γ-ray emission takes place in the middle of the target. However, for excited states with sufficiently long lifetimes, the decay takes place after traveling some distance through the target, leading to a more downstream z position and a slower velocity than the assumption. This produces a tail to the low-energy side on the peak for forward angle detectors. To illustrate this lifetime effect, a single transition with an energy of 1 MeV was simulated with various lifetimes. The resulting lineshapes are shown in Figure 4.22.

The lifetime effect is particularly important for the excited 0^+ state at 1788 keV, whose half-life was reported to be 3.9(4) ns [53]. The response function for the 1788 $\rightarrow$ 1482 $\rightarrow$ 0 cascade is simulated with this level half-life. It should be noted that the 2^+ state at 1482 keV has a half-life of 1.5 ps based on the $B(E2)$ measurement [58]. Nevertheless, in the present experiment, this short lifetime does not cause a noticeable change in the lineshape or the peak position.

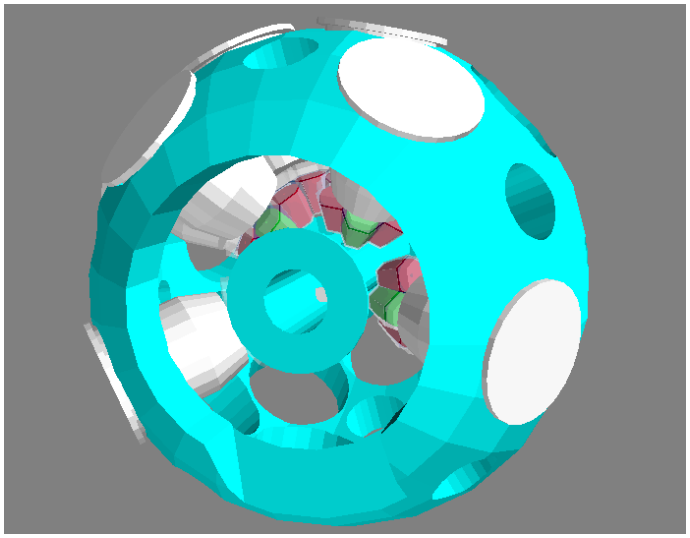

Figure 4.21: Materials used in the simulation. In addition to the detector volume, the surrounding materials are included. The S800's quadrupole magnet and gate valve are not shown in this figure. The beam passes through the duct with a flange. The beam axis points out of the paper.

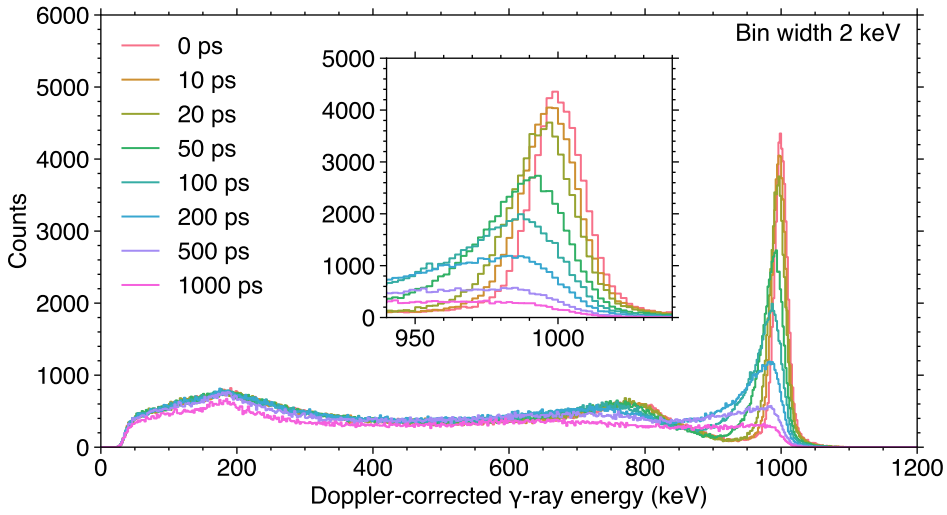

Figure 4.22: Simulated γ-ray spectrum assuming a 1-MeV transition with various lifetimes.

4.4.2 Fits to experimental spectra

Before performing fits to experimental spectra, the contributions from background γ rays need to be addressed. In knockout experiments, a continuous background is always present in γ-ray spectra. Even though the origin of the background has not been studied thoroughly, it is known that the background cannot be explained solely by atomic processes. Usually, the background is the most pronounced in the low energy region and decays exponentially with energy. A similar continuous background is observed in different reactions, such as inelastic scattering induced by a nuclear target. However, the background is absent in pickup reactions [112]. One of the possible origins of this background is the light charged particles and neutrons arising from the interactions of target breakup products; the light particles interact with surrounding materials

and produce a beam-correlated prompt background. The background is often modeled by a double exponential empirically. As a function of γ-ray energy emitted in the rest frame E, the background γ-ray yield is written as

$$Y_{\mathrm{bg}}(E) = b_1 e^{-p_1 E} + b_2 e^{-p_2 E} \tag{4.10}$$

where the amplitudes b_1 and b_2 and the decay constants p_1 and p_2 are treated as free parameters.

Additionally, discrete γ rays from neutron-induced reactions with surrounding materials also create a beam-correlated background in the mid-energy region around 500–1000 keV. These γ rays are clearly seen in the lab-frame γ-ray spectrum shown in Figure 4.12. γ lines from neutron-induced reactions with the aluminum beam pipe and germanium crystals (see Table 4.1) as well as the annihilation line at 511 keV are observed. To account for the background originating from these γ rays emitted at rest, monoenergetic γ lines in the lab frame were Doppler-shifted with a fixed β_{ref} in Equation (4.4). The resulting Doppler-corrected spectrum was used for fits, as was attempted before [113].

Table 4.1: List of beam-correlated background γ rays originating from neutrons interacting with the surrounding materials. The 691-keV transition was not observed after applying a timing cut on prompt γ rays because of its long lifetime (about 400 ns). γ-ray energies are taken from the ENSDF database [4].

Energy (keV)	Reaction
567	^{76}Ge(n,n')
600	^{74}Ge(n,n')
691	^{72}Ge(n,n')
835	^{72}Ge(n,n')
842	^{27}Al(n,n')
1013	^{27}Al(n,n')
1040	^{70}Ge(n,n')

Using the simulated response functions for each transition $y^{(i)}_{\mathrm{sim}}(E)$, the exponential background $Y_{\mathrm{bg}}(E)$ of Equation (4.10), and the Doppler-shifted background γ rays $Y_{\mathrm{rest}}(E)$, the experimental γ-ray spectra were fitted to obtain scaling factors a_i of each response function and thus γ-ray intensities. The total γ-ray yield to be fitted is written as

$$Y(E) = Y_{\mathrm{sim}}(E) + Y_{\mathrm{bg}}(E) + Y_{\mathrm{rest}}(E) = \sum_i a_i y^{(i)}_{\mathrm{sim}}(E) + Y_{\mathrm{bg}}(E) + Y_{\mathrm{rest}}(E). \tag{4.11}$$

First, the intensities of the peaks above 600 keV were obtained from a single fit to the spectrum. The fit for the low-energy part of the spectrum (below 600 keV) was performed separately after determining the intensities of the higher-lying peaks. This approach enables to better model the background contribution around the long-lived 305-keV transition where the extrapolation of the background shape towards low energy is difficult. The fitting results are shown in Figures 4.23, 4.24, 4.25 and 4.26. The relative γ-ray intensities are summarized later in Table 5.3, and the resulting exclusive cross sections are presented in Table 5.4.

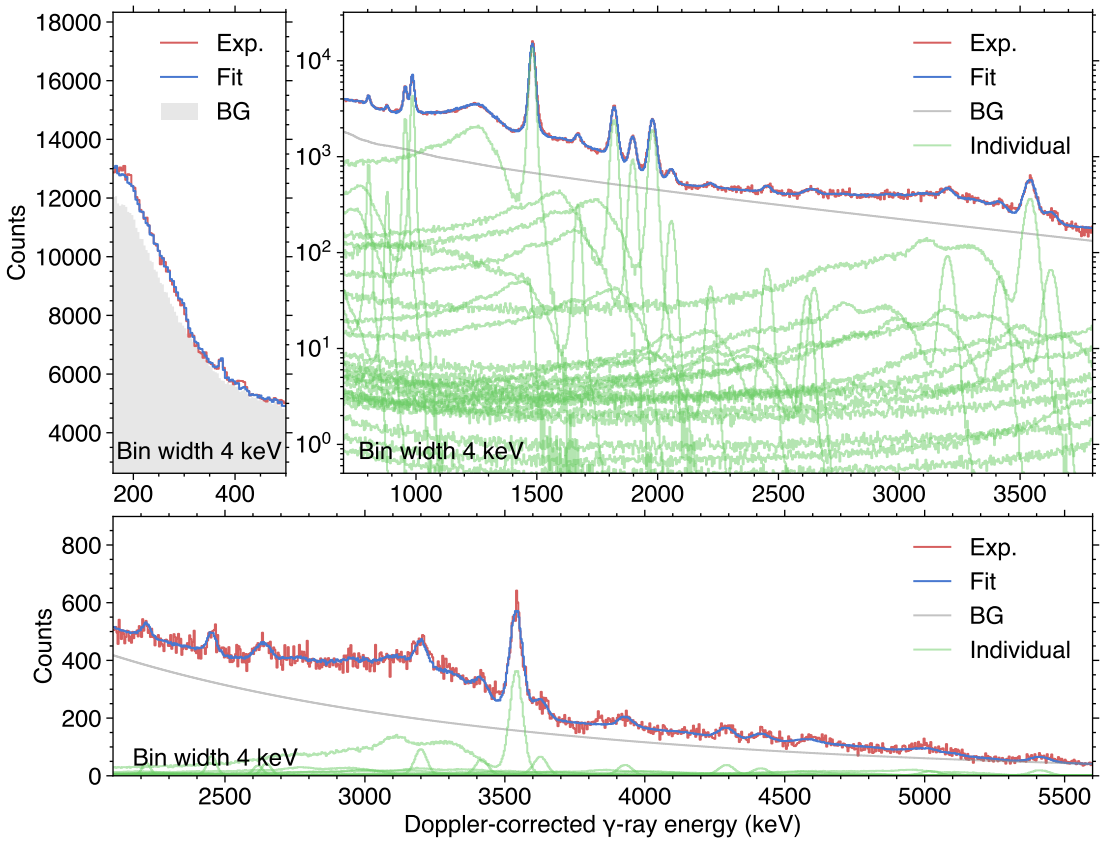

Figure 4.23: Doppler-corrected γ-ray spectrum for one-neutron knockout from ^{31}Mg without add-back. The fit used to extract γ-ray intensities is shown in blue. In the right panel, individual response functions (green) and background contributions modeled by a double exponential and Doppler-shifted γ rays emitted at rest (gray) are shown. The shaded gray area in the left panel shows the sum of the Compton background originating from all higher-lying peaks, the double exponential background, and Doppler-shifted γ rays emitted at rest. The bottom panel shows the high-energy part.

4.5 Parallel momentum distributions

To extract the parallel momentum distribution for each state, the feeding from higher-lying states should be taken into account. The procedure is similar to the extraction of exclusive cross sections: the background-subtracted momentum distribution associated with each γ-ray transition is first normalized to the γ-ray intensity, and then the momentum distribution for a specific state is deduced by adding and subtracting the distributions according to the level scheme. The extraction of the parallel momentum distribution also assumes that all the transitions are observed and correctly placed in the level scheme. It should be noted that the extracted distributions potentially have systematic uncertainties originating from unplaced and unobserved transitions, but the estimation of such uncertainties is not practical.

The extracted momentum distributions are then compared with theoretical calculations. As the reaction calculation gives parallel momentum distributions in the center-of-mass frame, they have to be Lorentz-boosted to the laboratory frame by multiplying the inverse of the Lorentz factor γ^{-1} to the parallel momentum $p_{\parallel}$ in the center-of-mass frame. In addition, the calculated distribution in the laboratory frame $F_{\mathrm{eik}}(p_{\parallel}/\gamma)$ has to be convoluted with the experimental

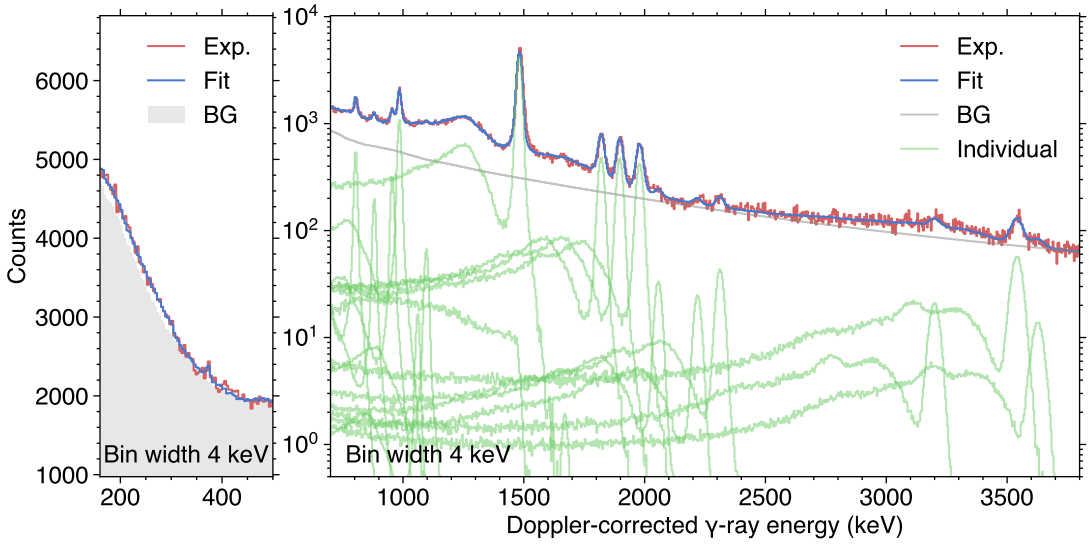

Figure 4.24: Same as Figure 4.23, but for two-neutron removal from ^{32}Mg.

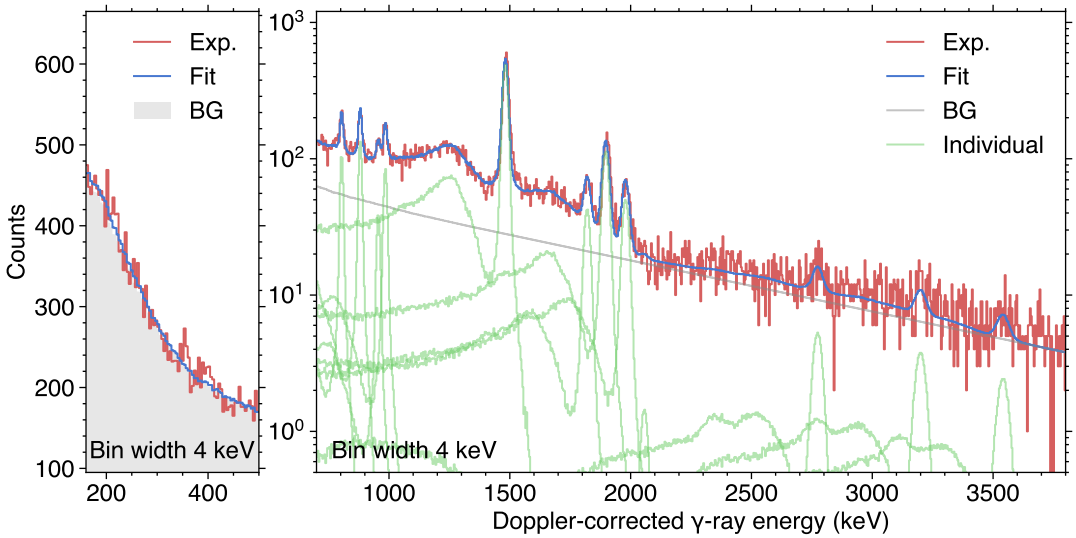

Figure 4.25: Same as Figure 4.23, but for multi-nucleon removal from ^{34}Si.

resolution. The unreacted beam setting of ^{31}Mg is used to extract the parallel momentum profile $F_{\text{unreact}}(p_{\parallel})$. This includes the intrinsic momentum spread of the secondary beam and the momentum broadening due to the presence of the reaction target. In knockout reactions, the velocities of the projectile and the residue are approximately conserved, so the distribution is scaled by $(A-1)/A$. The folded momentum distribution $F(p_{\parallel})$ can be written as

$$F(p_{\parallel}) = F_{\text{eik}}(p_{\parallel}/\gamma) * F_{\text{unreact}}\left(\frac{A}{A-1}p_{\parallel}\right) \tag{4.12}$$

where $*$ denotes a convolution.

In knockout experiments performed with a nuclear target and at intermediate energies (roughly 100 MeV/nucleon), a tail to the low-momentum side of the momentum distribution is

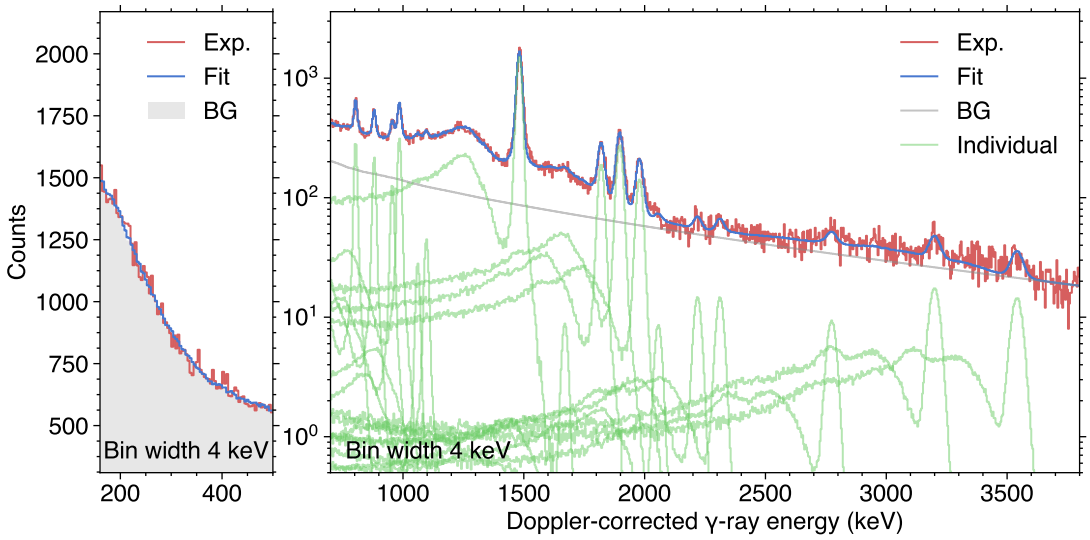

Figure 4.26: Same as Figure 4.23, but for multi-nucleon removal from ^{35}P.

often observed. This is associated with inelastic processes that cannot be explained by a direct one-step process. It is worth noting that, to empirically account for the low-momentum tail, the use of the measured inelastic momentum distribution instead of the unreacted beam was proposed in [109, 110], and a better reproduction of the measured momentum distribution was found. However, this was not pursued in the present experiment.

In Figure 4.27 calculated momentum distributions for the $2s_{1/2}$, $1d_{3/2}$, $1f_{7/2}$, and $2p_{3/2}$ orbitals after the convolution of Equation (4.12) are shown. Experimental momentum distributions are compared to the calculations later in Section 5.3.1 (see Figures 5.1 and 5.3).

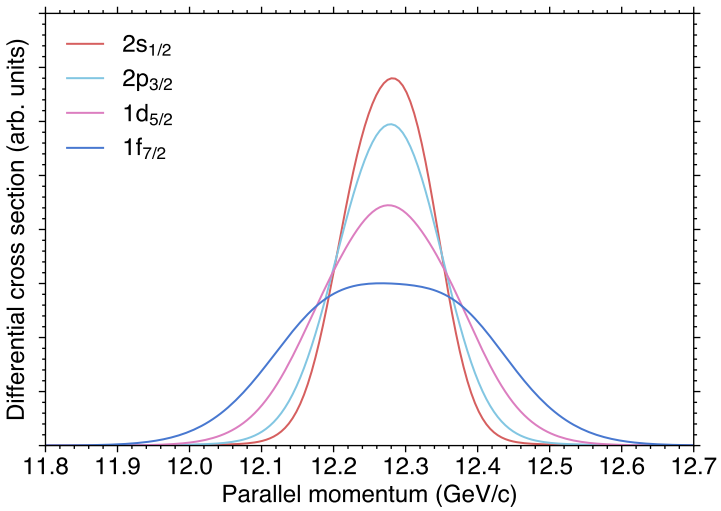

Figure 4.27: Convoluted momentum distributions assuming knockout from the $2s_{1/2}$ (red), $1d_{3/2}$ (pink), $1f_{7/2}$ (blue), and $2p_{3/2}$ (cyan) orbitals.

Chapter 5

Results

This chapter presents the results of the data analysis described in Chapter 4. First, the results of the γ-ray analysis, including an updated level scheme for ^{30}Mg, are shown in Section 5.1. The spin and parity assignments for each excited state are determined in Section 5.3. Based on the measured cross sections and the spin-parity assignments, spectroscopic factors have been extracted. These results are presented in Section 5.4.

5.1 Level scheme

The observed transitions and their energies are listed in Table 5.1. The 305-keV transition does not produce a peak in the γ-ray spectra because of the long half-life, 3.9(4) ns [53], of the 0^+_2 state at 1788 keV. The lifetime and energy could not be determined in this work independently since the present experiment was not optimized to detect such a long-lived state. For the $0^+_2 \rightarrow 2^+_1$ transition energy, the value was instead taken from a β-γ measurement [55]. Transition energies higher than 3400 keV were taken from the results of a β-γ measurement [55], except for the 3541-keV peak. For the two peaks not observed in [55], their transition energies, 3883 keV and 4293 keV, were determined from the present data.

The main source of the uncertainty in the transition energy is the uncertainty in the reference velocity β_{ref} used for the Doppler correction, which is correlated with the uncertainty in the target position, since it is determined using the data itself. It was observed that a z-position shift of 1 mm will result in an energy shift of 0.15 %. This has been included in the uncertainties in Table 5.1. This table also provides comparisons with selected previous measurements, showing good agreement with the present results. In terms of the transition energy determination, β-γ measurements are advantageous over the in-beam γ-ray experiments [47, 48], because the Doppler correction is not involved in these cases and lifetimes do not affect the determination of energies.

Table 5.2 summarizes the observed coincidences. The level scheme for ^{30}Mg was constructed based on this table. The 1482-keV γ ray corresponds to the de-excitation of the first excited 2^+ state in ^{30}Mg [50]. Although the coincidence of the 1482 keV and delayed 305-keV transitions was not confirmed in the present γ-γ analysis, this cascade was established in β-decay studies [27, 53]. Thus, the 305-keV transition was placed directly above the 2^+ state. The 3541-keV transition was reported to originate from the direct ground-state decay [50]. Other transitions are placed in the level scheme based on Table 5.2. The level scheme obtained in this work is presented later in Figure 4.17. The 2057 keV and 3541-keV transitions respectively feeding the state at

1482 keV and the ground state are assumed to originate from the same state, as the energies are close to each other. This level structure and the branching ratio from the 3540-keV state are consistent with β-decay measurements [51, 55].

Table 5.1: Observed γ-ray energies and transitions based on the present γ-γ analysis. The energies are shown in units of keV. The γ-ray energies are compared to those obtained in previous measurements [47, 48, 51, 55]. The transitions shown in the brackets are instead taken from [55]. Energy uncertainties were not indicated in [55].

Adopted E_γ	Transition	Ref. [51]	Ref. [55]	Ref. [47]	Ref. [48]
305	1788→1482	305.6(3)	305		300(5)
373(1)*					
804(1)	4183→3379			802.3(6)	799(2)
881(1)	4260→3379			879.0(9)	
956(1)	4258→3302			954.0(15)	954(2)
985(1)	2467→1482	985.1(4)	984	984.8(17)	985(2)
1061(3)*				1059.8(9)	
1097(2)*					
1482(2)	1482→0	1482.0(3)	1482	1480.6(5)	1482(2)
1670(3)	5210→3540				1660(2)
1820(3)	3302→1482	1820.2(6)	1820	1816.0(23)	1816(2)
1897(3)	3379→1482		1898	1898.4(8)	
1979(3)	3461→1482	1978.0(6)	1978	1974.8(19)	1975(2)
2057(3)	3540→1482	2059.0(6)	2059		
2219(5)†	(4683→2466)		2216		
2312(4)*					
2453(4)*					
2618(12)†	(5095→2466)	2626.0(13)	2627		
2648(11)*					
2774(5)*					
3200(5)†	(4683→1482)		3201		
3431†	(5897→2466)		3431		
3541(5)	3540→0	3541.1(11)	3542		3534(6)
3625†	(5414→1788)	3625.0(11)	3625		
3883(9)*					
3930†	(5414→1482)	3929.7(13)	3930		
4293(7)*					
4415†	(5897→1482)	4414.4(15)	4415		
4582†	(6064→1482)		4582		
4967†	(4967→0)		4967		
5022†	(5022→0)	5021.7(12)	5022		
5095†	(5095→0)	5094.3(12)	5095		
5414†	(5414→0)	5411.8(12)	5414		

* Unplaced transitions.

† Transitions that could not be placed in the level scheme in the present γ-γ analysis, but the placements are given in β-decay results [51, 55].

Table 5.2: Summary of coincident γ rays from ^{30}Mg observed in one-dimensional projections of Figures 4.17 and 4.18. The ticks (✓) denote the observed coincidences.

E_γ (keV)	804	881	956	985	1482	1670	1820	1897	1979	2057	3541
804					✓			✓			
881					✓			✓			
956					✓		✓				
985					✓						
1482	✓	✓	✓	✓			✓	✓	✓	✓	
1670											✓
1820			✓		✓						
1897	✓	✓			✓						
1979					✓						
2057					✓						
3541						✓					

5.2 Cross sections

As was shown in Section 4.4, the γ-ray spectra were fitted by simulated GRETINA response functions and background contributions. The fits were performed below 6000 keV for the one-neutron knockout reaction from ^{31}Mg. The fitting range of the other reaction channels are below 3800 keV. The relative γ-ray intensities compared to the $2^+_1 \rightarrow 0^+_1$ transition for each reaction channel are shown in Table 5.3. Only the statistical uncertainties are indicated in this table. An additional systematic uncertainty associated with the half-life uncertainty of the 1788-keV state, 3.9(4) ns, needs to be taken into account for the cross sections.

The exclusive cross sections were extracted using Equation (4.6). The calculation is based on the level scheme constructed in this work shown in Figure 5.5. In the present experiment, weak γ rays were also observed in the high-energy region of the spectra. Although these transitions could not be placed in the level scheme in the present γ-γ analysis, the placements of some of the transitions were already given in the previous β-decay studies [51, 55]. The contributions from these γ rays were also taken into account, relying on the level scheme constructed by Shimoda et al. [55]. The transitions with known placements are indicated by daggers in Table 5.1. According to [55], these transitions are reported to feed the states at 2466 keV, 1788 keV, 1482 keV, and the ground state. The resulting cross sections are presented in Table 5.4.

Table 5.3: Relative γ-ray intensities for each incoming beam obtained by fits to the Doppler-corrected γ-ray spectra without add-back. The empty cell mean that the corresponding γ ray is not included in the fit. The intensities are scaled with respect to the 1482-keV transition. The errors shown are statistical only.

E_γ (keV)	^{31}Mg	^{32}Mg	^{34}Si	^{35}P
305[a]	0.268(17)	0.164(33)	0.051(90)	0.024(49)
373*	0.009(1)	0.008(2)		
804	0.028(1)	0.058(3)	0.097(8)	0.086(4)
881	0.016(1)	0.023(2)	0.136(9)	0.071(4)
956	0.102(1)	0.042(3)	0.044(8)	0.047(4)
985	0.180(2)	0.146(3)	0.098(9)	0.118(5)
1061*		0.003(3)		0.012(4)
1097*		0.011(3)		0.020(5)
1482[b]	1.000(2)	1.000(5)	1.000(17)	1.000(10)
1670	0.027(1)	0.000(11)	0.001(17)	0.007(5)
1820	0.243(2)	0.154(3)	0.119(10)	0.171(6)
1897	0.099(2)	0.160(4)	0.333(12)	0.263(7)
1979	0.215(2)	0.153(3)	0.157(10)	0.145(6)
2057	0.026(1)	0.012(3)	0.004(6)	0.009(4)
2219†	0.006(1)	0.010(2)		0.018(4)
2312*		0.020(3)		0.019(4)
2453*	0.013(1)			
2618†	0.007(2)			
2648*	0.009(2)			
2774*			0.029(7)	0.017(5)
3200†	0.027(2)	0.018(3)	0.027(7)	0.041(5)
3431†	0.019(2)			
3541	0.127(2)	0.058(3)	0.021(8)	0.040(5)
3625†	0.024(2)	0.015(3)		
3930†	0.016(2)			
4293*	0.019(1)			
4415†	0.014(2)			
4582†	0.004(2)			
4967†	0.004(2)			
5022†	0.014(2)			
5095†	0.008(2)			
5414†	0.027(2)			

[a] An additional systematic uncertainty of 10 % originating from the lifetime uncertainty needs to be taken into account.

[b] The prompt component only.

* Unplaced transitions.

† Transitions that could not be placed in the level scheme in the present γ-γ analysis, but the placements are given in β-decay results [51, 55].

Table 5.4: Exclusive cross sections deduced from the γ-ray intensities shown in Table 5.3. The cross sections are presented in units of mb. Systematic uncertainties related to the overall normalization, i.e. the fluctuation in the beam composition depending on the incoming beam and the target thickness tolerance (see Section 4.3), and also a 3 % error of the absolute γ-ray detection efficiency are included.

E_x (keV)	^{31}Mg	^{32}Mg	^{34}Si[a]	^{35}P[a]
0	17.2(19)	49.7(25)	0.0318(52)	0.169(19)
1482	10.2(5)	17.1(8)	0.0131(17)	0.088(7)
1788	13.8(19)	7.2(18)	0.0025(45)	0.008(17)
2467	8.4(4)	6.5(3)	0.0049(6)	0.035(3)
3302	7.9(4)	5.4(3)	0.0037(7)	0.043(3)
3379	3.1(2)	3.8(3)	0.0050(9)	0.037(4)
3461	12.0(5)	7.3(3)	0.0078(8)	0.051(3)
3540	6.2(3)	3.3(6)	0.0012(10)	0.015(3)
4183	1.5(1)	2.8(2)	0.0048(5)	0.030(2)
4258	5.7(3)	2.0(2)	0.0022(4)	0.016(2)
4260	0.9(1)	1.1(1)	0.0068(7)	0.025(2)
5210	1.5(1)	0.0(5)	0.0001(9)	0.002(2)
Inclusive	97(3)	108(2)	0.085(3)	0.54(3)

[a] The cross sections of incoming ^{34}Si and ^{35}P should be seen as lower limits because of the acceptance issue (see Section 4.3).

5.3 Spin and parity assignments

5.3.1 Comparisons of parallel momentum distributions

Following the discussion in Section 4.5, the experimental momentum distributions were compared with the reaction model calculations (see Figure 5.1). The error bars shown in Figure 5.1 are statistical only. Note that, in the present analysis, the feeding subtraction is based on the level scheme constructed in this work. The feeding subtraction due to the weak γ rays from higher-lying states was not attempted, as such γ rays do not allow for the clear extraction of momentum distributions.

A χ^2 analysis was performed to examine which theoretical distribution best reproduces the observation. As only the shape of the momentum distribution is relevant in the comparison, the overall normalization factor and the offset in the parallel momentum were treated as free parameters. Data points used in the fit were restricted above 12.16 GeV/c in order to avoid having the previously-mentioned low-energy tail component. The best-fit χ^2 values are obtained for each of the assumed orbital ($2s_{1/2}$, $2p_{3/2}$, $1d_{3/2}$, and $1f_{7/2}$), and the orbital that gives the smallest χ^2 is then used to constrain the spin and parity of that state. The reduced χ^2 values are tabulated in Table 5.5 together with constraints on the spins and parities.

Here, it is instructive to show the robustness of the extracted momentum distributions. As an example, the momentum distribution for the state at 2467 keV, which is directly obtained by gating on the 985 keV photopeak, is shown in Figure 5.2 using different γ-ray gates. It is clear that the resulting distributions are insensitive to the choice of the gates.

The momentum distributions of the states at 3379 keV, 4186 keV, and 4260 keV show a highly asymmetric shape that is incompatible with any of the calculated momentum distributions, as can be seen in Figure 5.3.

The momentum distribution for populating the ground state is obtained by subtracting distributions associated with all feeding transitions from the total distribution. However, the present data did not allow for the clear extraction of the distribution. This implies that other unobseved transitions are present and thus the ground-state cross section should be seen as an upper limit.

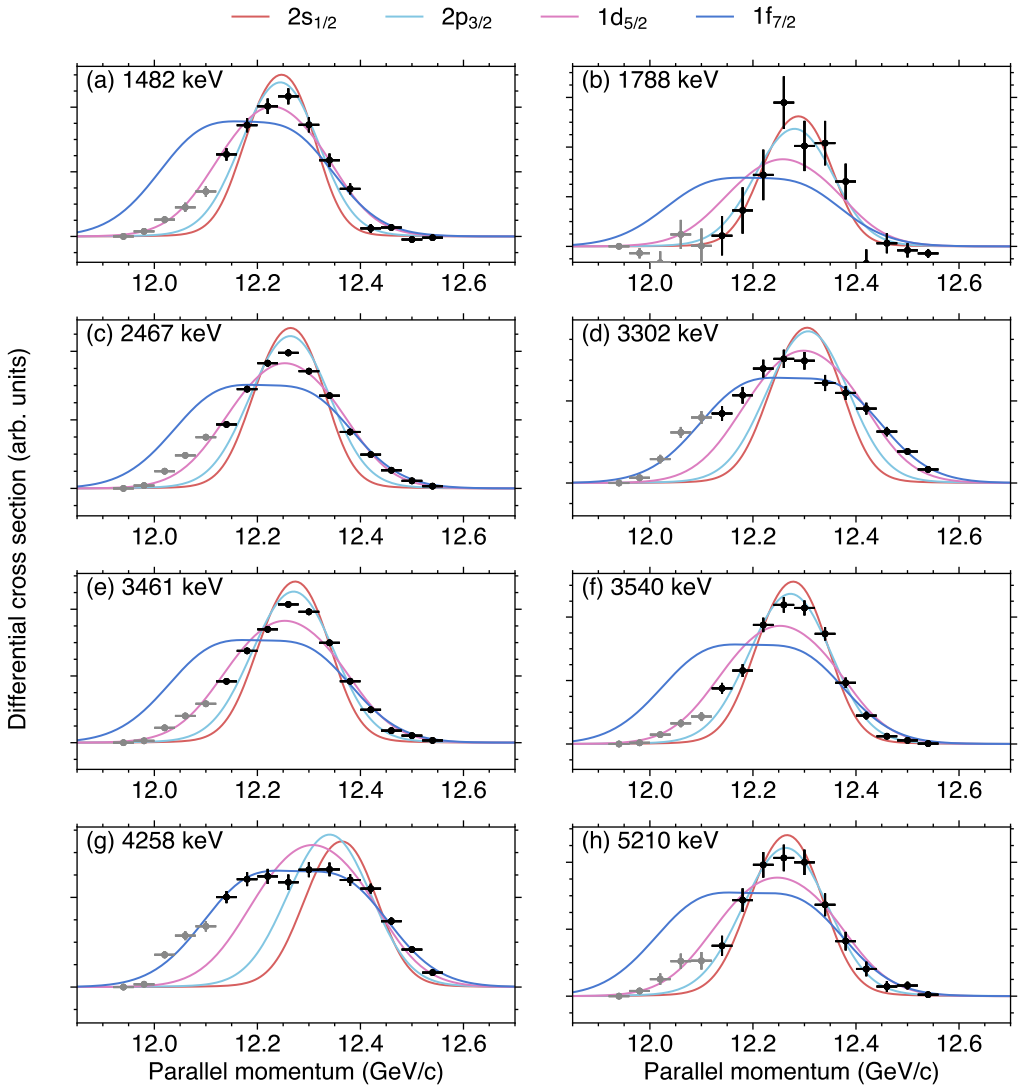

Figure 5.1: Experimental momentum distributions in comparison with calculations assuming knockout from $2s_{1/2}$ (red), $1d_{3/2}$ (pink), $1f_{7/2}$ (blue), and $2p_{3/2}$ (cyan) orbitals. The calculated distributions are fitted to the black data points, whereas the gray data points are not used for the fit. The error bars on each point are statistical only.

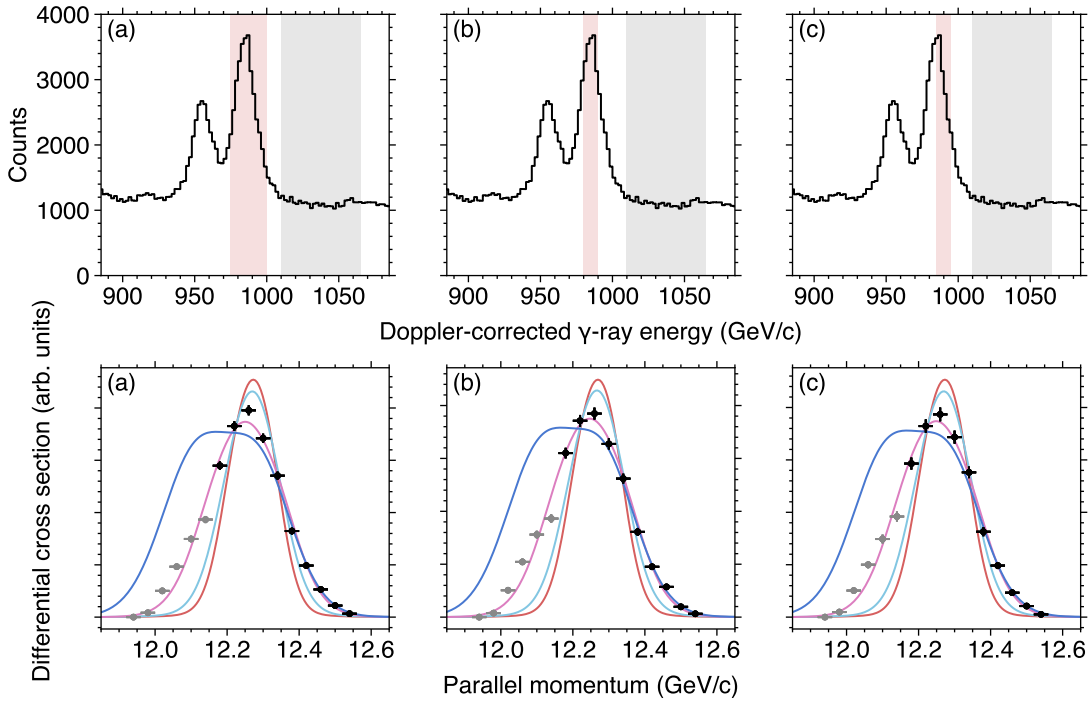

Figure 5.2: Momentum distributions for the state at 2467 keV extracted with different gates: (a) a wide gate on the 985 keV peak to maximize the statistics, (b) a narrow gate (±5 keV) on the peak, and (c) a narrow gate on the high-energy side of the peak. The red shaded region corresponds to the photopeak gate, while the gray region is used to estimate the background.

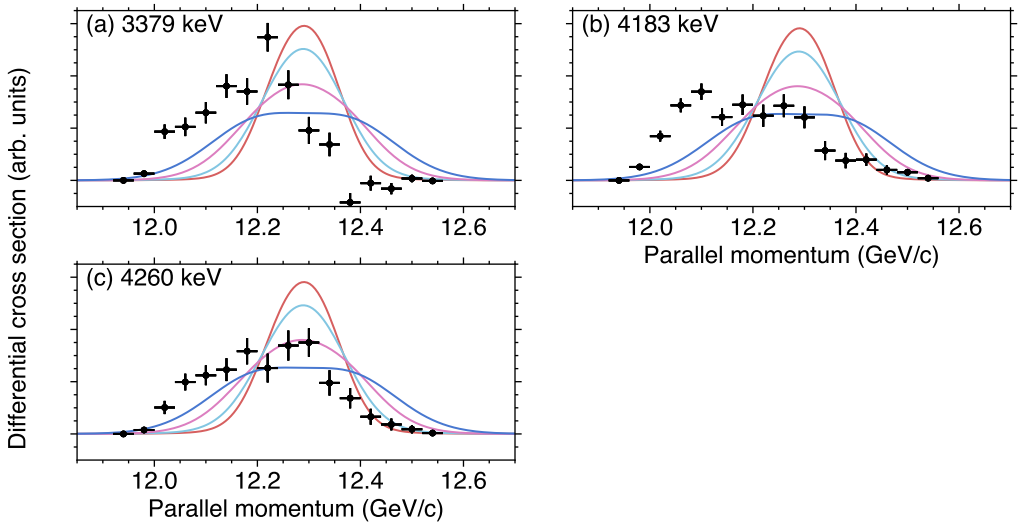

Figure 5.3: Experimental momentum distributions showing a highly asymmetric shape. Calculated momentum distributions, with the same color code as Figure 5.1, are not fitted to the experimental distribution.

Table 5.5: Reduced χ^2 values of experimental momentum distributions with respect to the calculations assuming neutron knockout from the $2s_{1/2}$, $2p_{3/2}$, $1d_{3/2}$, and $1f_{7/2}$ orbitals. The minimum values are shown in boldface. The χ^2 values associated with the momentum distributions for the states at 3379 keV and 4183 keV are not shown here, as they are governed by the "tail" component and incompatible with the calculated distributions.

E_x (keV)	$2s_{1/2}$	$2p_{3/2}$	$1d_{3/2}$	$1f_{7/2}$	Possible J^π
1482	13.5	5.1	**3.0**	9.4	2^{+a}
1788	**1.3**	1.7	3.3	4.8	0^{+a}
2467	129.5	50.8	**4.9**	54.7	$1^+, 2^+$
3302	49.2	30.1	5.3	**1.9**	$3^-, 4^-$
3461	87.9	24.1	**14.2**	71.0	$1^+, 2^{+b}$
3540	9.8	**1.8**	8.6	23.2	$1^-, 2^-$
4258	91.3	60.5	14.8	**2.0**	$3^-, 4^-$
5210	2.9	**0.6**	2.4	6.3	$1^-, 2^-$

[a] The states at 1482 keV and 1788 keV were already assigned as 2^+ and 0^+, respectively.
[b] A doublet of states is proposed as will be discussed in Section 6.1.2.

5.3.2 Relative cross sections

It has been observed that yrast states are preferentially populated in fragmentation-like multi-nucleon removal reactions, as pointed out in [59]. The 4^+ yrast state in ^{20}O was populated in the ^{36}S(^{9}Be,X) reaction [67]. Another example is the ^{36}Si(^{9}Be,X) reaction, where the population of the 4^+ yrast state in ^{34}Mg [114] was observed. Moreover, the population of the 6^+ yrast state in ^{32}Mg following the fragmentation on ^{46}Ar was reported recently [115]. Even though there is no effective theory that can quantitatively predict the level population in multi-nucleon removal reaction, the cross sections of these reactions can be used as a qualitative tool. It should be noted that it is not possible to form a spin-parity of 4^+ by direct single-particle knockout from the *sd* and *pf* orbitals in the $1/2^+$ ground state of ^{31}Mg. The direct population of a 4^+ state would require neutron knockout from the $1g_{9/2}$ orbital, but this is incompatible with the structure of ^{31}Mg and very unrealistic. Therefore, excited states with $J^\pi = 4^+$ and states with a spin of $J \geq 5$ require more complicated reaction processes that go beyond the one-step direct knockout. The different reaction mechanism is also reflected to the momentum distribution, as can be seen in Figure 5.3.

The cross sections of the multi-nucleon removal reactions relative to those of one-neutron knockout from ^{31}Mg are shown in Figure 5.4. Relative enhancements in the cross sections populating the states at 3379 keV 4183 keV, and 4260 keV can be seen. As discussed above, these are indicative of the yrast or high-spin nature of the states. It is natural to assign a spin-parity of 4^+ to the 3379 keV state as a member of the ground-state band. A 4^+ assignment to the state at 3379 keV was already made in the previous fusion-evaporation experiment by Deacon *et al.* [47] by measuring the angular distribution of the γ ray de-exciting this state. Similarly, for the state at 4183 keV, Deacon *et al.* also suggested either the $E1$ or $M1$ multipolarity of the de-excitation γ ray to the 3379-keV state, and therefore the state was given a $J = 5$ assignment.

Another feature that can be seen in the relative cross sections is the small population of the 0_2^+

state in the multi-nucleon removal reactions. Starting from normal-configuration nuclei ^{34}Si and ^{35}P, it would be less easy to populate such an intruder-dominated state, and the present result is in line with this speculation. However, the discussion for the two-neutron removal from ^{32}Mg is more complicated and less straightforward. The ground state of the ^{32}Mg is characterized by an intruder configuration and thus firmly placed inside the island of inversion. Therefore, one may expect statistical population of states with some additional population of intruder-dominated states in ^{30}Mg, but the observation does not give definitive evidence that this conjecture holds.

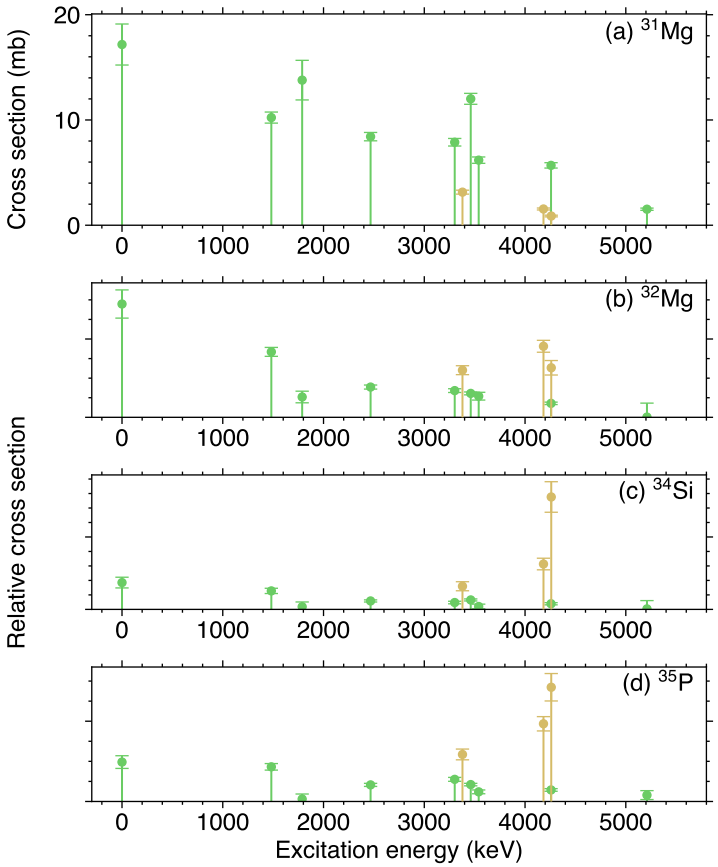

Figure 5.4: Comparison of cross sections to populate states in ^{30}Mg in different reaction channels. (a) Cross sections for the one-neutron knockout reaction from ^{31}Mg. Cross sections for the multi-nucleon removal reactions from (b) ^{32}Mg, (c) ^{34}Si, and (d) ^{35}P relative to the cross sections of ^{31}Mg. Candidates for the high-spin states are highlighted in yellow.

5.3.3 Summary of spin-parity assignments

Following the results presented earlier, spin-parity assignments to the observed states in ^{30}Mg are discussed on a level-by-level basis. To further constrain the assignments, characteristic decay patterns have also been utilized. The resulting level scheme for ^{30}Mg is presented in Figure 5.5 together with the determined spins and parities.

1482-keV and 1788-keV states

As reviewed in Section 1.4.3, there is no doubt of the correctness of the 2^+ assignment for the state at 1482 keV. Following the observation of the conversion electron associated with the $E0$ decay of the 1788-keV state by Schwerdtfeger *et al.* [27], the 0_2^+ assignment to this state was also firmly established. These spin-parity assignments are cross-checked by the momentum distributions. Figure 5.3 shows the corresponding momentum distributions. χ^2 minimizations in Table 5.5 validate the 2^+ and 0^+ assignments.

2467-keV state

The present data clearly favor knockout from the $1d_{3/2}$ orbital. The robustness of this result is demonstrated in Figure 5.2. Therefore, the possibility of a negative parity was rejected, and the spin-parity of this state is assigned as 2^+. This interpretation is also supported by shell-model calculations. As detailed in Section 6.2, calculations reproduce the excitation energy of the 2_2^+ state without much sensitivity to the choice of interactions.

3302-keV state

According to Table 5.5, the momentum distribution supports knockout from the $1f_{7/2}$ orbital and possible J^π are 3^- and 4^-. In the latter case, the transition to the 2_1^+ state at 1482 keV should be characterized by the M2 multipolarity, and as such, likely carries a lifetime which should have been observed in the present experiment. Thus, a spin-parity assignment of 3^-, which allows for an $E1$ transition, is most likely. The non-observation of a direct ground-state decay is in line with this assignment.

3379-keV state

This state is a candidate for the 4^+ of the ground-state band, as first suggested by Deacon *et al.* [47]. The coupling of the ground-state spin of $1/2^+$ and a neutron hole in the $sdpf$ orbitals does not allow for the population of a 4^+ state. Thus, the population of this state should involve a more complicated, indirect multi-step excitation. This different reaction process is also reflected in the momentum distribution showing a very asymmetric shape. As can be seen in Figure 5.3 (a), the distribution is not compatible with any of the calculated momentum distributions. Therefore, the 4^+ assignment made in [47] is adopted here.

3461-keV state

The momentum distribution agrees with knockout from the $1d_{3/2}$ orbital, although the reduced χ^2 presents a higher value than others. A tentative 2^+ assignment is made here, guided by the preliminary assignment in a β-γ measurement [55]. In the case of a 1^+ assignment, the state would decay to the ground state directly. It is worth noting that shell-model calculations do not produce any 1^+ states being as low as 3.5 MeV. The observed momentum distribution is slightly narrower than the calculated distribution for pure $1d_{3/2}$ knockout. The presence of a doublet of states may explain this deviation. This possibility is discussed later in Section 6.1.2. The 4^+ assignment previously given to this state [47] is incompatible with the observed momentum distribution.

3540-keV state

The momentum distribution for this state is compatible with knockout from the $2p_{3/2}$ orbital, and thus spin-parity assignments of 1^- and 2^- are suggested. An assignment of 1^- is preferred because of a strong γ-ray branch to the ground state. Table 5.6 shows γ-ray relative intensities of the two transitions depopulating this state. The experimental branching ratio is better reproduced when the $E1$ nature of both transitions is assumed. In this work, therefore, a spin-parity of 1^- is proposed.

Table 5.6: Relative γ-ray intensities of the 3541 keV and 2057-keV transitions. Experimental relative intensities (I_{exp}) are compared with calculated ones based on Weisskopf estimates (I_{W}) for the two possible spin-parity assignments of 1^- and 2^- for the state at 3540 keV. Weisskopf estimates of transition strengths are given by $6.45 \times 10^{-2} \times A^{2/3}\, e^2\mathrm{fm}^2$ for $E1$ and $1.65 \times A^{2/3}\, {\mu_N}^2$ for $M2$.

E_i (keV)	E_f (keV)	I_{exp}	I_{W} (1^-)	I_{W} (2^-)
3540	1482	0.23(1)	0.16 ($E1$)	1.0 ($E1$)
3540	0	1.00(2)	0.84 ($E1$)	1.4×10^{-5} ($M2$)

4183-keV state

This state was first observed in Deacon *et al.* [47] and a $J = 5$ assignment was made. Similar to the state at 3379 keV, the momentum distribution is very asymmetric, as can be seen in Figure 5.3 (b). The $J = 5$ spin assignment is adopted here.

4258-keV and 4260-keV states

For the state at 4258 keV, the momentum distribution clearly shows knockout from the $1f_{7/2}$ orbital (see Figure 5.1 (g)), suggesting a spin-parity assignment of 3^- or 4^-. Now that the state at 3302 keV is assigned as a 3^- state, it is natural to assume a 4^- assignment to this state as a partner originating from $1f_{7/2}$.

As the states at 4258 keV and 4260 keV are close to each other in energy, one might be tempted to assume these states are identical. However, these two states show different momentum distributions (see also Figure 5.3 (c)). Moreover, the ratio of the intensities of the 956-keV and 881-keV γ rays, respectively depopulating the states at 4258 keV and 4260 keV, are shown to vary depending on the reaction channel by an order of magnitude. The ratios are summarized in Table 5.7. As discussed earlier, similar to the other cases, the asymmetric momentum distribution associated with the 4260-keV state and the relative enhancement of the 881-keV γ ray in the multi-nucleon removal reactions are the indication of the high-spin nature of this state.

Table 5.7: γ-ray intensities of the 881-keV transition relative to 956 keV calculated for each reaction channel.

E_γ (keV)	^{31}Mg	^{32}Mg	^{34}Si	^{35}P
881	0.15(1)	0.55(6)	3.06(20)	1.52(10)
956	1.00(1)	1.00(7)	1.00(17)	1.00(9)

5210-keV state

This state was placed in this work for the first time. Although the 1670-keV γ ray was first observed in the previous knockout measurement by Fernández-Domínguez *et al.* [48] (corresponding to the 1660(2)-keV transition in their result), the placement of this transition was not possible due to the limited statistics. In the present measurement, this transition is clearly coincident with 3541-keV γ ray which de-excites a candidate for a negative-parity state at 3540 keV. The narrow momentum distribution extracted from the present data suggests that this state is likely to be of negative parity, and the possible spin-parity is 1^- or 2^-. Considering the non-observation of a decay branch to the ground state, a 2^- assignment is proposed.

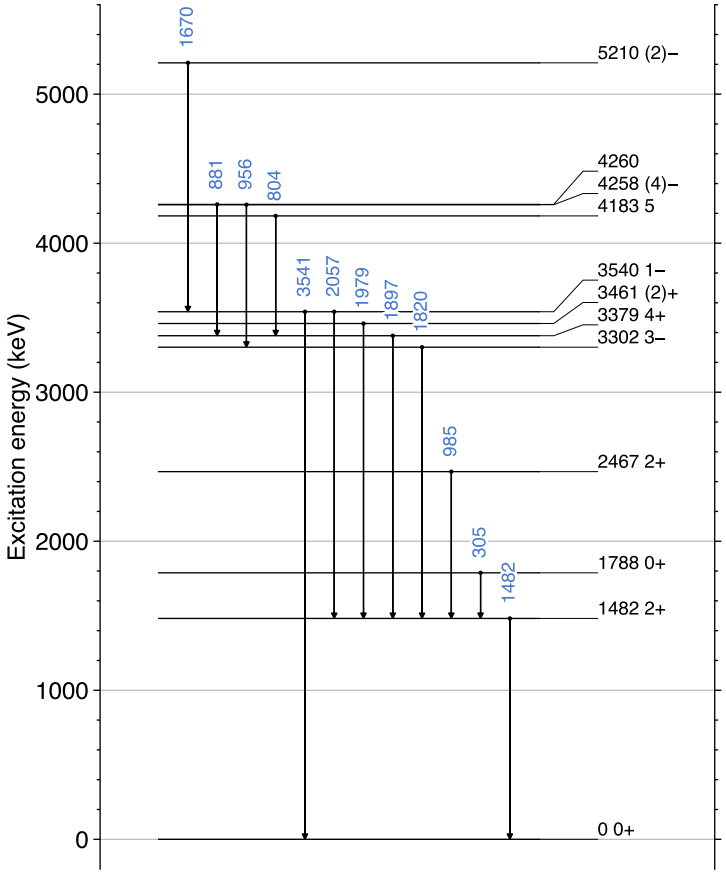

Figure 5.5: Experimental level scheme for ^{30}Mg constructed in the present experiment. Excitation energies in keV, spins and parities are shown beside the levels.

5.4 Experimental spectroscopic factors

Spectroscopic factors were deduced from the ratio of the experimental and the calculated single-particle cross sections. As the spectroscopic factors depend on the orbital from which the neutron is removed, spectroscopic factors and assumed single particle orbitals are shown together in Table 5.8. The corresponding single-particle cross sections are also indicated. The center-of-mass

correction, the factor $[A/(A-1)]^N$ in Equation (2.11), is included in the spectroscopic factor. In the table, only the statistical uncertainties are quoted. The details on the systematic uncertainties are described in the caption of Table 5.4. From the momentum distribution, neutron knockout from the $1d_{5/2}$ orbital is indistinguishable from that of $1d_{3/2}$, and even these contributions can mix. Nevertheless, the removal of a $1d_{5/2}$ neutron should be suppressed as compared those from the $2s_{1/2}$ and $1d_{3/2}$ orbitals, because the $1d_{5/2}$ orbital is deeply bound. The spectroscopic factors for the 4^+ state at 3379 keV and other candidates for the yrast states at 4183 keV and 4260 keV are not given, as these states cannot be populated via single-step one-neutron knockout.

Table 5.8: Experimental cross sections and spectroscopic factors. Assumed single particle orbitals, quantum numbers n and l are shown together. The center-of-mass correction factors are included in the spectroscopic factors. Spectroscopic factors with and without multiplying the reduction factor (see Section 2.2.6 for details) are shown separately.

E_x (keV)	Single-particle orbital	n	l	σ_{exp} (mb)	σ_{sp} (mb)	C^2S_{exp}	C^2S_{exp}/R_S[b]
0	$2s_{1/2}$	1	0	17.2(19)	52.1	0.31(4)	0.35(4)
1482	$1d_{3/2}$	0	2	10.2(5)	22.0	0.43(2)	0.51(3)
1788	$2s_{1/2}$	1	0	13.8(19)	35.0	0.37(5)	0.44(6)
2467	$1d_{3/2}$	0	2	8.4(4)	19.8	0.40(2)	0.48(2)
3302	$1f_{7/2}$	0	3	7.9(4)	17.1	0.42(2)	0.51(2)
3379				3.1(2)			
3461[a]	$1d_{3/2}$	0	2	12.0(5)	18.0	0.62(3)	0.76(3)
3540	$2p_{3/2}$	1	1	6.2(3)	23.9	0.23(1)	0.29(1)
4183				1.5(1)			
4258	$1f_{7/2}$	0	3	5.7(3)	16.1	0.32(1)	0.40(2)
4260				0.9(1)			
5210	$2p_{3/2}$	1	1	1.5(1)	20.1	0.07(1)	0.09(1)

[a] A doublet of states is proposed here. The spin-parity assignments and the spectroscopic factors are discussed separately. See Section 6.1.2 for details.

[b] The reduction factor R_S is taken from Equation (2.13).

Chapter 6

Discussion

The interpretation of the experimental results is discussed in this chapter. In Section 6.1, the experimental level scheme with the spin-parity assignments as well as the spectroscopic factors are compared with previous in-beam and decay measurements for ^{30}Mg. Section 6.2 focuses on the comparison to theoretical calculations using the shell model. Systematics of the nuclear structure around ^{30}Mg are discussed in Section 6.3 with a special emphasis on the negative-parity states. Section 6.4 describes "T-plot" analyses to get more insight into the different shell-model interactions. Lastly, Section 6.5 summarizes the findings obtained in this work.

6.1 Comparison to previous experiments

6.1.1 In-beam measurements

As introduced in Section 1.4.3, Fernández-Domínguez *et al.* reported an in-beam γ-ray measurement using the one-neutron knockout reaction from ^{31}Mg [48]. Except for small differences in the experimental condition, i.e. a different target material (carbon) and a lower incident energy (55 MeV/nucleon), the reaction of interest is identical to the present work. Thus, their experimental results can be directly compared with the present results. The experimental levels and the spectroscopic factors are compared in Figure 6.1. Note that the reduction factor explained in Section 2.2.6 is not included in the spectroscopic factors presented in this section for the consistency.

Significantly increased statistics in the γ-ray spectra obtained in the present experiment allowed for the construction of an extended level scheme with updated spin-parity assignments (see also Figure 1.12 for comparison). The ground state can only be populated by the knockout of a $2s_{1/2}$ neutron from ^{31}Mg. The spectroscopic factor for the ground state deduced in this work is 0.31(4). This value is smaller than but in agreement with an upper limit of 0.50 presented in [48]. It should be noted that the presence of unplaced or unobserved transitions that directly feed the ground state can still lead to overestimation of the deduced cross section and thus a higher spectroscopic factor [116, 117]. This situation is known as the pandemonium effect, originally proposed in the context of β-γ spectrosocpy, where a number of weak transitions from fragmented higher-lying states escape observation and they feed the ground and low-lying states. The actual ground-state cross section is considered to be much smaller, and accordingly a clear momentum distribution for the ground state could not be extracted. Therefore, the present spectroscopic factor should be taken as an upper limit. The spectroscopic factor leading to

the ground state of ^{31}Mg was extracted using proton resonant elastic scattering on ^{30}Mg. The deduced spectroscopic factor of 0.07 ± 0.03(stat.) ± 0.07(sys.) interpreted as a small overlap between the ground states of ^{30}Mg and ^{31}Mg, is smaller than the present estimate. The 0^+_2 state is also populated by removing a neutron from the $2s_{1/2}$ orbital. The removal of this neutron leaves the neutrons in the fp shell untouched, and thus can populate the intruder configuration. In the conventional picture of the structure of ^{30}Mg, the 0^+_2 state is dominated by an intruder configuration. A large spectroscopic factor of 0.37(5) which is in contrast to 0.20(4) in [48], may point to a substantial overlap with the intruder-dominated ground state of ^{31}Mg.

The 2^+_1 state is populated by the knockout of a $1d_{3/2}$ neutron. The present spectroscopic factor of 0.43(2) is compatible with an upper limit of 0.57 presented in [48]. The state at 2467 keV was previously discussed as a candidate for the 2^+_2 state [53]. This interpretation was questioned by [48], where the momentum distribution associated with this state favored, with limited statistics, the knockout from the $2p_{3/2}$ orbital and resulted in a negative-parity assignment. The present result rejects this assignment, and this state is now established as the 2^+_2 state. The spectroscopic factor extracted for this state is 0.40(2). Note that the cross section itself is slightly larger in the present measurement (8.4(4) mb compared to 7.6(11) mb in [48]) even though the feeding from the higher-lying states is taken into account in the present analysis. It is also worth noting that, not only for the 2467-keV state, the exclusive cross sections in [48] tend to show systematically lower values than the present values. For the inclusive cross section, the previous measurement reported a value of of 90(12) mb [48], which is slightly lower than but in agreement with the present estimate of 97(3) mb within the uncertainty.

By removing a $1d_{3/2}$ neutron, a candidate for the 2^+_3 state at 3461 keV was populated. The large spectroscopic factor of 0.62(3) naively understood as an intruder-dominated configuration of this state, is similar to the other cases, but again larger than the observation of [48]. However, this spectroscopic factor and the spin-parity have to be treated with caution, because of a possibility of having a doublet of states (see Section 6.1.2 for details). Previously, a 4^+ assignment to this state was made in the fusion-evaporation study [47]. As discussed earlier in Section 5.3.3, the clean, near symmetric momentum distribution is incompatible with 4^+, as this assignment requires a multi-step excitation and it would produce an asymmetric momentum distribution.

3^- and 4^- states can be populated by removing a $1f_{7/2}$ neutron. The state at 3302 keV was firmly assigned as the lowest negative parity state in ^{30}Mg in the present work. The spin-parity assignment of 3^- and spectroscopic factor of 0.42(2) is again slightly higher, but agrees with [48]. For the state at 4258 keV, the spin-parity assignment of $(4)^-$ and spectroscopic factor of 0.32(1) are also in line with [48].

Excited states characterized by knockout from the $2p_{3/2}$ orbital were found at 3540 keV and 5210 keV. The spectroscopic factor associated with the state at 3540 keV, 0.23(1) shows a lower value than [48]. This is partly because the 1670-keV γ ray, which could not be placed in the level scheme in the previous work, was newly observed to feed the 3540-keV state. The 1670-keV γ ray was assigned to the decay of the state at 5210 keV, and this level was given a tentative spin-parity assignment of $(2)^-$. This level was proposed for the first time in this work.

It should be emphasized that the analysis of the multi-nucleon removal reactions gave further information on the levels in ^{30}Mg. The enhancement of the population of the state at 3379 keV, 4183 keV, and 4260 keV in these reactions indicated the yrast nature of these states. The validity of the 4260 → 3379 → 1482 and 4183 → 3379 → 1482 cascades, originally proposed in [47], was confirmed by this work (see also Figure 1.11). On the other hand, coincidences of the 1061-keV transition proposed in [47] were not observed. Presently, a small peak at 1061-keV is

seen only in the multi-nucleon removal reactions from ^{32}Mg and ^{35}P. In both cases, the 1897-keV transition is strongly seen, while the very weak 1061-keV transition and the non-observation of the 838-keV γ ray are conflicting with the relative intensities proposed in [47]. Considering that the 4258 $\rightarrow$ 3302 $\rightarrow$ 1482 cascade was firmly established in the present work, the placement of the 1061-keV transition on top of the 1482-keV state, resulting in a negative-parity candidate at 2541 keV suggested in [47], is not supported by the present data. Moreover, if this state were of negative parity, it should have been strongly populated in one-neutron knockout because of the intruder-dominated nature of the ground state of ^{31}Mg. This state might be arising from the misidentification of γ rays from different reaction products or higher-lying states in ^{30}Mg. The relative enhancement of the 1061 keV transition in the multi-nucleon removal reaction from ^{35}P indicates that this transition is originating from a high-spin state, although the placement is not possible presently.

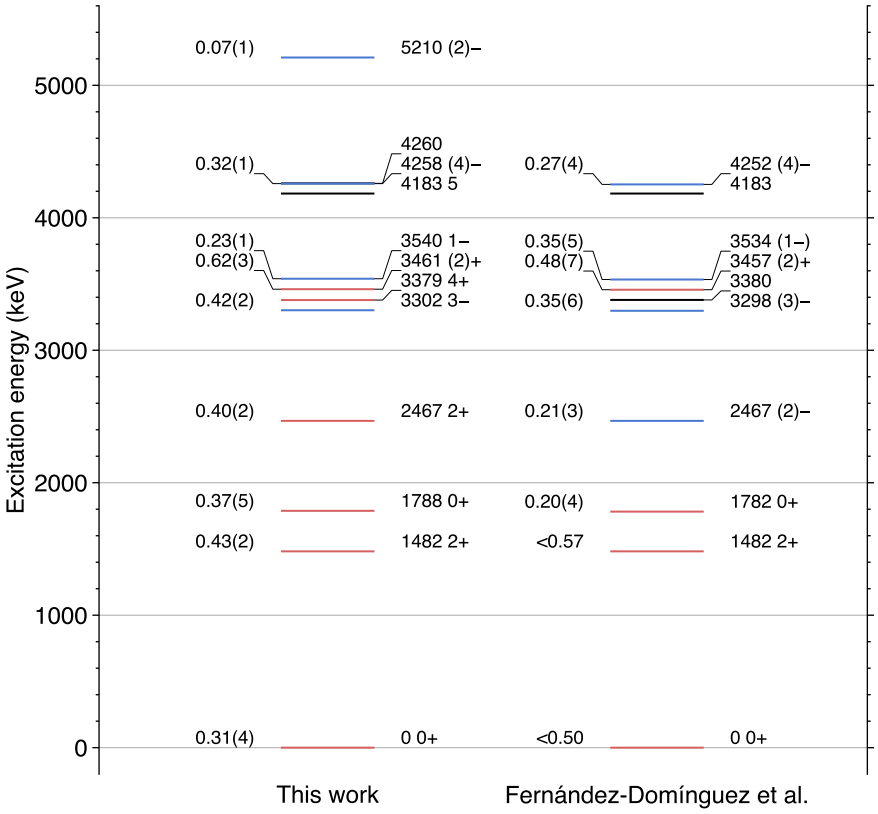

Figure 6.1: Comparison of the experimental levels of ^{30}Mg obtained in the present experiment and the previous measurement by Fernández-Domínguez *et al.* [48]. States with positive (negative) parity are shown in red (blue). Spectroscopic factors are indicated to the left of the levels.

6.1.2 β-decay measurements

In general, β-decay measurements provide $\log ft$ values, which are indicative of the type of the transition and can be used to constrain spins and parities. Note that the ground state of ^{30}Na has a spin-parity of 2^+ [60, 118]. Moreover, the use of a polarized radioactive beam and the measurement of β-decay asymmetry allow for the determination of spins and parities. However, as β decay predominantly populates levels higher than 4.9 MeV in ^{30}Mg, the spin-parity sensitivity is lost for the low-lying states.

A spin-parity of $(2,3)^+$ was assigned to the state at 3302 keV in [55] based on the $\log ft$ of 6.5(1) which indicates an allowed transition. This spin-parity assignment is in contradiction to the present 3^- assignment. More recently, an updated measurement [119] reported a larger $\log ft$ of 7.0(4), in line with a forbidden transition. This updated value does not reject the possibility of the negative-parity assignment. In the same measurement, the state at 4259 keV was observed for the first time in β-γ studies. The associated large $\log ft$ points to a forbidden transition and a negative-parity assignment is compatible with the present assignment of $(4)^-$.

The β-γ measurement [119] proposed a doublet of states at 3463 keV and 3461 keV. These two states are reported to decay to the 2^+_1 state by emitting 1978-keV and 1980-keV γ rays, respectively. The present experiment is not sensitive to this small difference, and thus it is not possible to disentangle which state is populated. Nevertheless, the momentum distribution showed a deviation from the calculated distribution for the pure $1d_{3/2}$ knockout and thus an increased χ^2 (see Figure 5.1 (e)). It is possible that the observed momentum distribution contains contributions from both 3463-keV and 3461-keV states with different spins and parities. A fit to the experimental momentum distribution with a sum of $1d_{3/2}$ and $2p_{3/2}$ components allows for the extraction of each contribution (see Figure 6.2). This assumption does not conflict with the result of the β-γ measurement, where the 3463-keV and 3461-keV states are respectively given $(1,2)$ and (2) assignments. The resulting cross sections of the individual components are 5.8(6) mb ($1d_{3/2}$) and 6.2(6) mb ($2p_{3/2}$), respectively leading to $C^2S_{\mathrm{exp}}/R_S = 0.37(4)$ and 0.29(3).

A spin-parity assignment of 2^+ to the state at 2467 keV was first suggested in the β-decay study by Mach *et al.* [53]. The assignment was guided by its short half-life of less than 5 ps and similarity to the decay pattern of the 2^+_2 state at 4555 keV in ^{28}Mg [120]. In the present analysis, the energy of the γ-ray peak de-exciting this state is determined to be 985(1) keV. Simulations show that a half-life of 5 ps leads to an energy shift of 1 keV in the Doppler-corrected γ-ray spectrum, and therefore the present data is consistent with an upper limit of 5 ps. A longer half-life, for example, 10 ps leading to a peak shift of 3 keV, would be incompatible with the observation of the peak at the correct energy. As discussed in [53], if a pure $E2$ is assumed for the 985-keV transition, a large $B(E2; 2^+_2 \rightarrow 2^+_1)$ of more than 123 e^2fm^4 is required to reproduce the lifetime, while shell-model predictions are on the order of 1 e^2fm^4 (see Section 6.2). This suggests a substantial $M1$ component of this transition.

6.2 Comparison to shell-model calculations

For the interpretation of the present experimental results, the level scheme and spectroscopic factors are compared to shell-model calculations using the SDPF-M [37], SDPF-U-MIX [13], and EEdf1 [41] interactions, which were introduced in Section 1.3.2.

The calculations with the SDPF-M and EEdf1 interactions were performed with the code

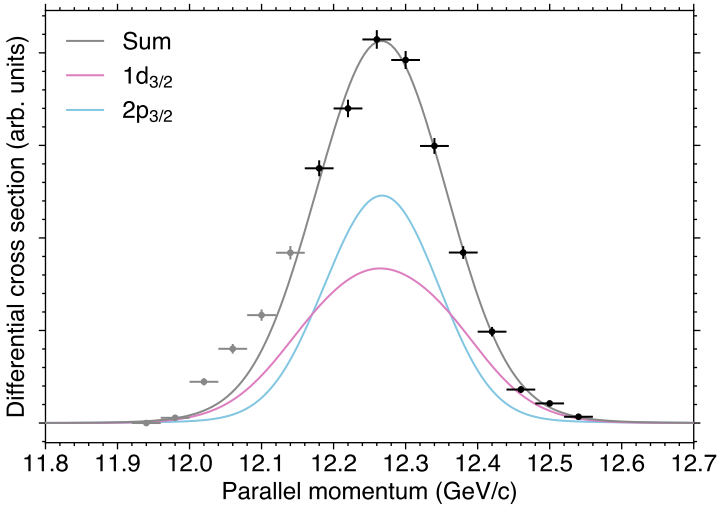

Figure 6.2: Fit to the experimental momentum distribution in coincidence with the 1979-keV γ ray. The fit assumes a sum of $1d_{3/2}$ (pink) and $2p_{3/2}$ (cyan) momentum distributions to extract each scaling factor. The fitted distribution is shown in gray (reduced $\chi^2 = 1.9$).

KSHELL [121]. The calculation with the SDPF-M interaction presented here is the result of the exact diagonalization without any truncation, while excitations up to $6\hbar\omega$ were allowed in the EEdf1 calculation because of limitations in the computational power. The result of the SDPF-U-MIX interaction was taken from [48]. Spectroscopic factors for one-neutron knockout from ^{31}Mg were also calculated in the shell model by taking the overlap of wave functions describing the ground state of ^{31}Mg and states in ^{30}Mg. Note that the SDPF-M (SDPF-U-MIX) calculation predicts a $7/2^-$ ($3/2^-$) ground state in ^{31}Mg. Instead, a $1/2^+$ state appears as an excited state. For the calculation of spectroscopic factors, the wave function of the first excited $1/2^+$ state is taken as being analogous to the the $1/2^+$ ground state.

In Figure 6.3, these calculations are compared with the experimental result. All of the calculations reproduce the present level scheme remarkably well. It is seen that the excitation energy of the 2^+_1 state and the correct ordering of the low-lying 0^+ and 2^+ states are reproduced. The negative-parity states are localized above 3.5 MeV. These features are common to all the calculations.

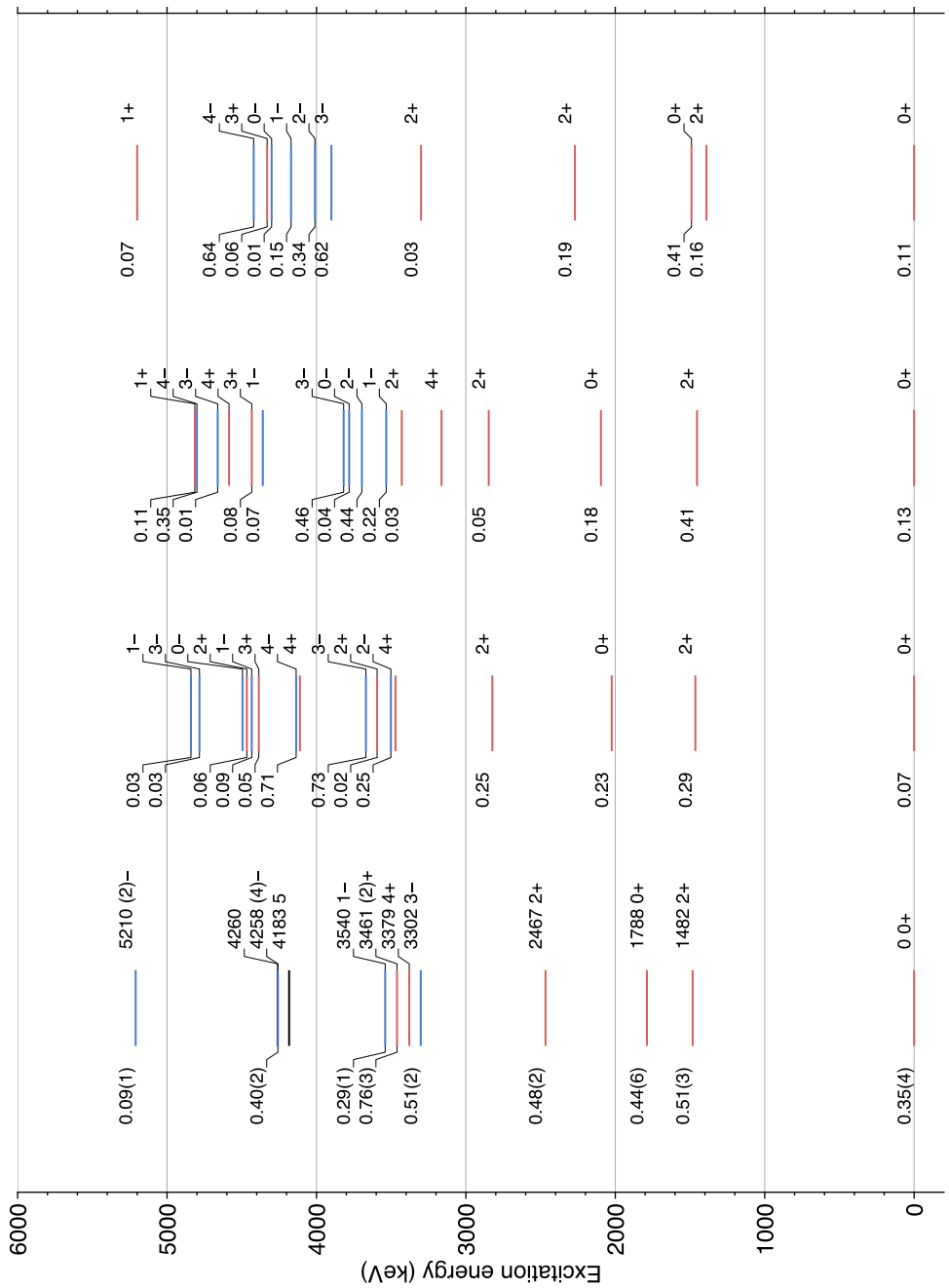

Figure 6.3: Experimental levels of ^{30}Mg in comparison with shell-model calculations using the SDPF-M, EEdf1, and SDPF-U-MIX interactions. States with positive (negative) parity are shown in red (blue). Experimental spectroscopic factors $C^2S_{\rm exp}/R_S$ and shell-model spectroscopic factors are indicated to the left of the levels. The spectroscopic factor for the 3461-keV state has to be treated with caution (see the caption of Figure 6.4).

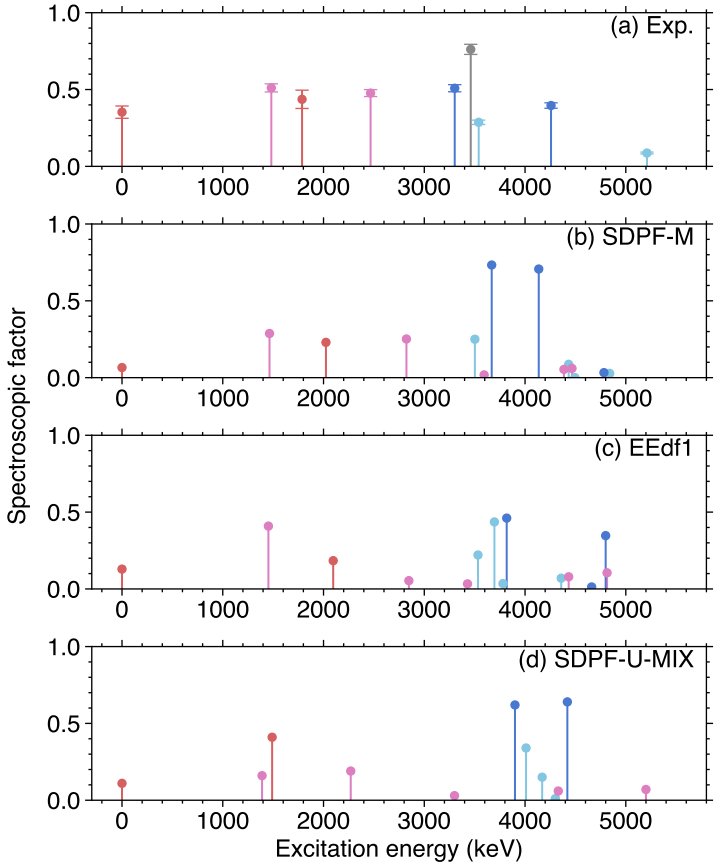

Figure 6.4: Experimental spectroscopic factors in comparison with shell-model predictions. The experimental values are shown in the panel (a). The experimental spectroscopic factors have been corrected for the reduction factor (see the last column of Table 5.8). The calculated spectroscopic factors using the SDPF-M, EEdf1, and SDPF-U-MIX interactions are shown in the panels (b), (c), and (d), respectively. States associated with $l = 0, 1, 2, 3$ are respectively shown in red, cyan, pink, and blue. The spectroscopic factor for the 3461-keV state (indicated in gray) has to be treated with caution. A fit to the momentum distribution assuming both $1d_{3/2}$ and $2p_{3/2}$ components gives 0.37(4) ($1d_{3/2}$) and 0.29(3) ($2p_{3/2}$) as discussed in Section 6.1.2.

The calculated spectroscopic strengths show a much larger variation depending on the interaction used, despite the similarity in the level structures. This is visualized in Figure 6.4, together with the spectroscopic factors deduced from the present experiment. The sum of spectroscopic factors for a specific orbital can be considered as an estimate or a lower limit of the occupancy of that orbital. The sum will exclude some states, but usually the majority is concentrated in low-energy states. The summed experimental spectroscopic factor associated with the $1f_{7/2}$ orbital of 0.90(4) indicates a significant occupation of the $1f_{7/2}$ orbital in the ground state of ^{31}Mg. Similarly, the summed spectroscopic factor of 0.37(2) from the $2p_{3/2}$ orbital also indicates a sizable occupation of the $2p_{3/2}$ orbital in ^{31}Mg. Note that, as discussed in Section 6.1.2, there is a doublet of states at 3461 keV, one of which could be originating from the $2p_{3/2}$ orbital. The summed spectroscopic factor for $2p_{3/2}$ increases to 0.66(4) if this contribution is added. These can also be compared with negative-parity spectroscopic factors

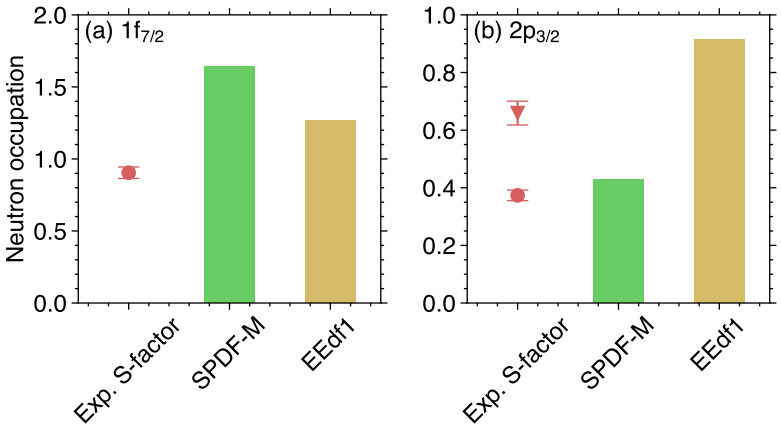

Figure 6.5: Comparison of experimental spectroscopic factors to neutron occupancies for (a) the $1f_{7/2}$ and (b) the $2p_{3/2}$ orbitals in ^{31}Mg calculated using the SDPF-M and EEdf1 interactions. The sum of deduced spectroscopic factors associated with $1f_{7/2}$ (the 3^- and 4^- states) is shown. The sum associated with $2p_{3/2}$ (the 1^- and 2^- states) is indicated by the circle. As discussed in Section 6.1.2, there can be a doublet of states at 3461 keV, one of which could be originating from $2p_{3/2}$. The triangle represents the sum of spectroscopic factors including this contribution.

deduced for one-neutron removal from ^{30}Mg and ^{32}Mg [25]. Strengths leading to the first $7/2^-$ and $3/2^-$ states are 0.41(10) and 0.19(7) in ^{29}Mg, while those of ^{31}Mg are 1.19(36) and 0.59(11). The present values are in between these values or somewhat closer to those of ^{31}Mg. The large occupation of the fp orbitals is a direct consequence of the intruder dominance of the ground state of ^{31}Mg. Figure 6.5 shows a comparison of the summed experimental spectroscopic factors with calculated neutron occupancies in ^{31}Mg. The summed spectroscopic factor for the $1f_{7/2}$ orbital is significantly lower than the SDPF-M occupancy, while that of the $2p_{3/2}$ orbital exceeds the the SDPF-M occupancy if the contribution from the 3461-keV state is added. The absolute values of all of spectroscopic factors associated with positive states obtained in the present analysis are not reproduced by any of the calculations. Nevertheless, the strengths relative to the ground state and the large spectroscopic factor for the 2^+_2 state are somewhat closer to the calculation with SDPF-M.

Here, it is worth noting that the electromagnetic transition strengths between low-lying states calculated using the SDPF-M and EEdf1 interactions are in good agreement with the observation as well. With the standard effective charges of $(e_p, e_n) = (1.5, 0.5)e$ for SDPF-M and $(e_p, e_n) = (1.25, 0.25)e$ for EEdf1, predicted $B(E2; 0^+_1 \rightarrow 2^+_1)$ values are 332 e^2fm^4 (SDPF-M) and 285 e^2fm^4 (EEdf1), while a Coulomb excitation measurement reported 241(31) e^2fm^4 [58]. For the $0^+_2 \rightarrow 2^+_1$ transition, 38 e^2fm^4 (SDPF-M) and 51 e^2fm^4 (EEdf1) reproduce the observed half-life of 3.9(4) ns (calculated partial halflives of 6.1 and 4.1 ns, respectively). The substantial $M1$ component of the $2^+_2 \rightarrow 2^+_1$ transition is also supported by both calculations. The SDPF-M interaction gives $B(M1; 2^+_2 \rightarrow 2^+_1) = 0.15\,\mu_N{}^2$ and $B(E2; 2^+_2 \rightarrow 2^+_1) = 1.8\,e^2$fm^4, and the EEdf1 interaction gives $B(M1; 2^+_2 \rightarrow 2^+_1) = 0.19\,\mu_N{}^2$ and $B(E2; 2^+_2 \rightarrow 2^+_1) = 1.0\,e^2$fm^4. Note that a measurement of the γ-ray polarization could determine the mixing ratio of the $E2$ and $M1$ multipolarities in the future.

As explained in Section 1.3.2, the SDPF-M interaction has been traditionally used in this mass region, and it reproduces basic observables, like $E(2^+_1)$ and $B(E2; 0^+_1 \rightarrow 2^+_1)$ values [37].

While the SDPF-M interaction takes into account only the $1f_{7/2}$ and $2p_{3/2}$ orbitals on top of the full sd shell, the model space is extended to contain the full neutron $sdpf$ shells in the recently-developed interactions, SDPF-U-MIX and EEdf1. The latter two interactions also demonstrated their prediction power for the basic quantities [13, 41]. Here, it should be emphasized again that the EEdf1 interaction is different from SDPF-M and SDPF-U-MIX by construction. The TBMEs of the EEdf1 interactions are microscopically derived from a realistic QDC-based nucleon-nucleon potential, whereas the TBMEs of the other two are empirically adjusted to reproduce the experimental observables. Even though the present experimental results do not allow a definitive choice of the interaction to be made, the new experimental information serves as a benchmark for these calculations and also provides guidance for refinements of the interactions. This point is further discussed below.

To gain more insight into the calculated spectroscopic factors, shell-model calculations using modifications of the SDPF-M interaction have also been performed. First, the single-particle energy of the $2p_{3/2}$ orbital was lowered by 1 MeV. This modified interaction is named "SDPF-M-mod-A", and the result of the calculation is shown in Figure 6.6. Owing to the reduction of the $1f_{7/2}$-$2p_{3/2}$ gap, spectroscopic factors associated with $1f_{7/2}$ are reduced, while those of $2p_{3/2}$ are increased. This trend is closer to the experimental results. However, similarly to the EEdf1 calculation, the spectroscopic factor for the 2^+_2 state is reduced. The spectroscopic factors of the low-lying shape-coexisting states may be sensitive to the spacing between the sd and pf shells corresponding to the $N = 20$ gap. In SDPF-M-mod-A, the energy required to form intruder configurations becomes smaller, as the spacing between the sd and pf shells is effectively reduced. To compensate this, another calculation using "SDPF-M-mod-B" where $2p_{3/2}$ is lowered by 0.5 MeV and $1f_{7/2}$ is raised by 0.5 MeV was performed. In this approach, the sd-pf spacing is approximately conserved, while the $N = 28$ gap is reduced by 1 MeV. The result of the calculation is also shown in Figure 6.6. The balance of $1f_{7/2}$ and $2p_{3/2}$ spectroscopic factors is unchanged compared to the SDPF-M-mod-A calculation, while significant changes in spectroscopic factors of the low-lying shape-coexisting states are seen.

To summarize, the behavior of the calculated spectroscopic can be interpreted in terms of the interplay of the sd-pf gap corresponding to $N = 20$ and the $1f_{7/2}$-$2p_{3/2}$ gap corresponding to $N = 28$, as schematically shown Figure 6.7. The spectroscopic factors for the low-lying shape-coexisting states (0^+_1, 2^+_1, 0^+_2, and 2^+_2) are sensitive to the size of the $N = 20$ gap, while the balance of spectroscopic factors associated with the $1f_{7/2}$ and $2p_{3/2}$ orbitals is affected by the size of the $N = 28$ gap. Here, it is worth noting that there have been discussions about the single-particle energies in the SDPF-M interaction. It has been pointed out that the single-particle energy gap between the $1f_{7/2}$ and $2p_{3/2}$ orbitals may be overestimated in this interaction [122–124]. The present analysis supports this argument. The proper accounting of these gap sizes would be key to better reproduce the experimental spectroscopic factors.

6.3 Systematic behavior of the level structure around ^{30}Mg

Negative-parity states require the promotion of an odd number of particles from the sd to the fp shell and are therefore expected to be sensitive to the magnitude of the $N = 20$ shell gap, as was discussed in Section 1.4.1. In the simplest possible configuration (1p1h excitation), 0^-–3^- states can be formed by promoting a neutron from the $1d_{3/2}$ to the $2p_{3/2}$ orbital, leaving a single neutron hole in the $1d_{3/2}$ orbital. Similarly, the spin coupling allows 2^-–5^- states to be made by promoting a $1d_{3/2}$ neutron to the $1f_{7/2}$ orbital. Therefore, it is expected that the size of the shell

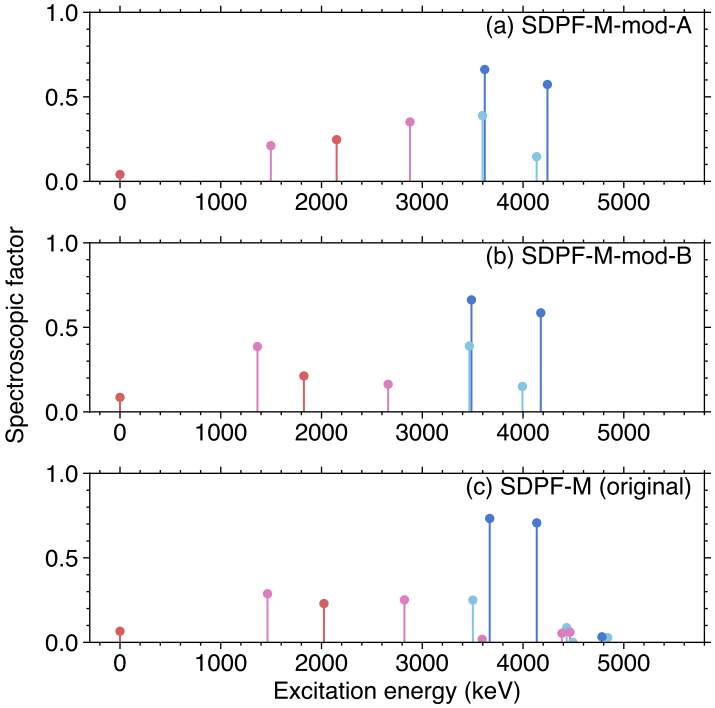

Figure 6.6: Calculated spectroscopic factors using (a) the SDPF-M-mod-A interaction where the $2p_{3/2}$ orbital is lowered by 1 MeV, (b) the SDPF-M-mod-B interaction where the $1f_{7/2}$-$2p_{3/2}$ gap is reduced by 1 MeV, and (c) the original SDPF-M which is identical to Figure 6.4. Only the lowest two states from a specific orbital have been calculated for the modified interactions. States associated with $l = 0, 1, 2, 3$ are respectively shown in red, cyan, pink, and blue.

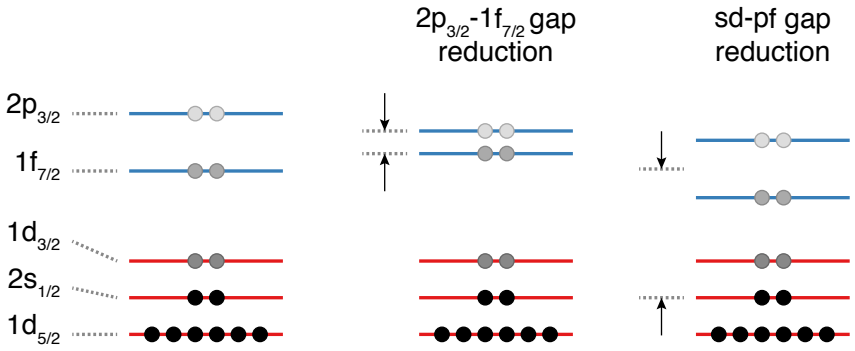

Figure 6.7: Schematic illustration of the $1f_{7/2}$-$2p_{3/2}$ ($N = 28$) and the sd-pf ($N = 20$) gaps. The $N = 28$ gap is important for describing the balance of the spectroscopic factors of $1f_{7/2}$ and $2p_{3/2}$. The spectroscopic factors for the low-lying shape-coexisting states are sensitive to the $N = 20$ gap size.

gap between $1d_{3/2}$ and $2p_{3/2}$ is more closely related to the excitation energies of the 1^- state.

However, these discussions should be treated with caution. In the shell model, the effective single-particle energies are said to be ones in the spherical limit, as they are defined based on the monopole component of the shell-model interaction. The effects arising from the nuclear deformation are contained in the multipole component of the interaction, and these

bring complications in the discussion of the shell-gap size [7]. Nevertheless, if one assumes a spherical shape and a pure neutron 1p1h excitation, in a qualitative manner, it is possible to relate the excitation energy of negative-parity states with the gap between the *sd* and *pf* shells.

Systematics of negative-parity states in $N = 18$ isotones are shown in Figure 6.8. The excitation energies of the lowest 1^- states stay rather constant at around 6 MeV above ^{32}Si, while the energy drops by more than 2 MeV between ^{32}Si and ^{30}Mg. Under the above-mentioned assumptions, the drop of the excitation energies of the 1^- state observed at ^{30}Mg could be interpreted as a signature of the reduction of the gap between $1d_{3/2}$ and $2p_{3/2}$. To illustrate the reduction of the gap, single-particle energies in the SDPF-M and EEdf1 interactions are shown in Figure 6.9. The drop in the excitation energy of the 1^- state coincides with the abrupt reduction of the shell gap at $Z = 12$. Systematics of the lowest 3^- states are also shown in Figure 6.8. A drop of excitation energy of about 2 MeV is seen between ^{32}Si and ^{30}Mg. In this case, the discussion is not as straightforward as the 1^- states, as both $2p_{3/2}$ and $1f_{7/2}$ can contribute. Moreover, a gradual increase in excitation energy is seen from ^{38}Ca to ^{32}Si. This feature could be attributed to the cross-shell excitation of protons. As protons are added to the $N = 18$ isotones, the energy spacing between the proton Fermi surface and the *pf* shell decreases. This makes proton cross-shell excitation energetically more favored and result in non-negligible contributions of the proton side.

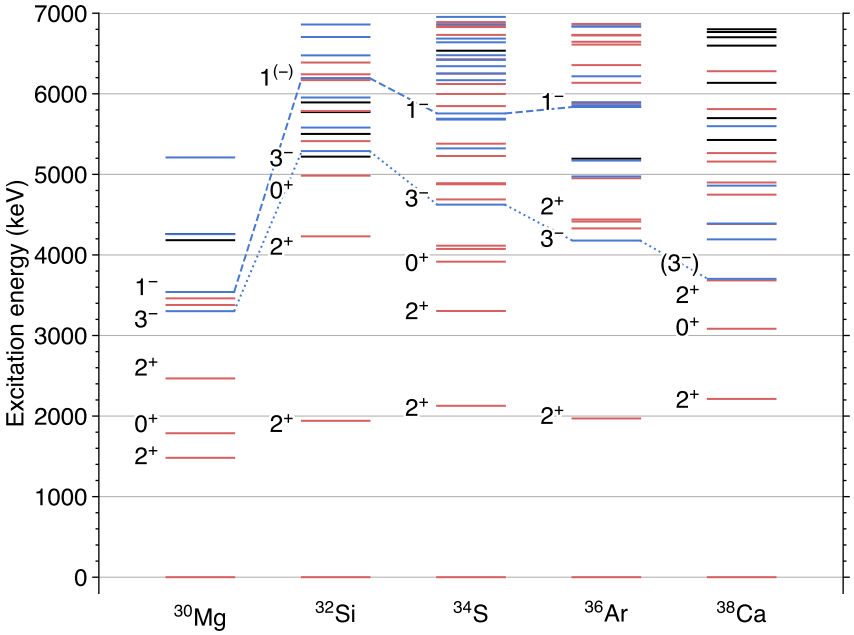

Figure 6.8: Systematics of negative-parity states in $N = 18$ isotones. Level data are taken from the ENSDF database [4]. The levels from the present experiment are shown for ^{30}Mg. The lowest 1^- (3^-) states are connected by dashed (dotted) lines. The spins and parities include tentatively assigned ones. Negative-parity (positive-parity) states are shown in blue (red).

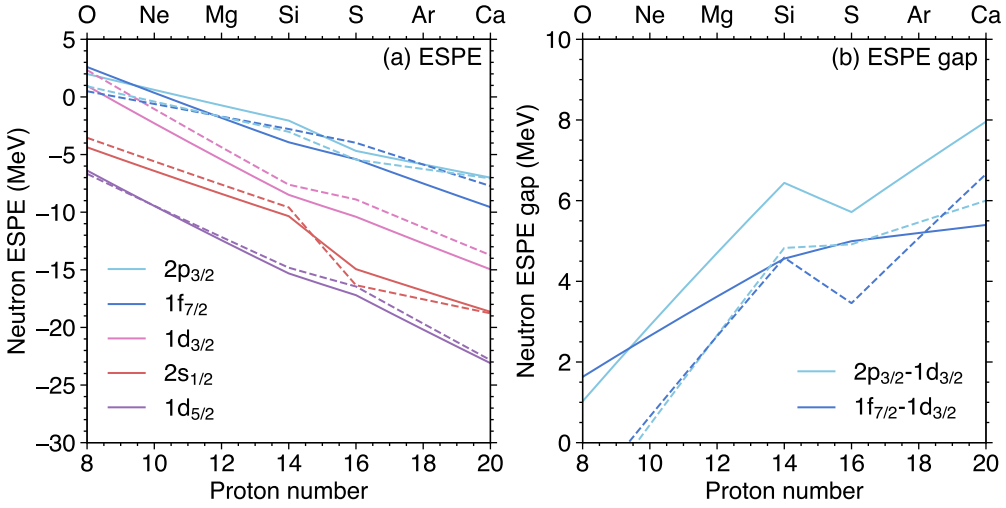

Figure 6.9: (a) Neutron effective single-particle energies as a function of proton number calculated for the $N = 18$ isotones using the SDPF-M (solid) and EEdf1 (dashed) interactions. (b) Effective shell-gaps associated with the $1f_{7/2}$ and $2p_{3/2}$ orbitals relative to the $1d_{3/2}$ orbital, taken directly from the panel (a).

6.4 T-plot analysis

As the wave functions for both initial and final states are involved, the discussion of the absolute value of the spectroscopic factors is complicated. Nevertheless, with the success in reproducing the experimental level structure, it is natural to assume that the basic ingredients of describing properties of each state are approximately captured by the shell-model calculations. To explore the nature of the underlying wave functions, the low-lying states were analyzed using the "T-plot" technique [125].

The intrinsic deformations of a specific state can be visualized in a T-plot analysis, where the plot shows the potential energy surface (PES) obtained by a Hartree-Fock calculation using the shell-model interaction with constraints on the quadrupole moments, Q_0 and Q_2. The PES is superimposed with circles describing the wave function of the states calculated by the Monte Carlo Shell Model (MCSM) approach [126]. The circles represent "deformed" Slater determinants of the MCSM, placed by their Q_0 and Q_2, and their size is proportional to the overlap between the MCSM eigenstate and the Slater determinant. The distribution of the circles and their sizes indicate the intrinsic shape and its fluctuation and mixing of the eigenstates.

The T-plots for the 0^+_1, 2^+_1, 0^+_2, and 2^+_2 states in ^{30}Mg obtained using the SDPF-M interaction are shown in Figure 6.10. One can see that the circles are localized in two places, the near spherical side (small $Q_0 \approx 30\,\mathrm{fm}^2$) and prolate-deformed side (large $Q_0 \approx 80\,\mathrm{fm}^2$) with a triaxial deformation. The 0^+_1 state is dominated by near spherical components, while the 0^+_2 state is governed by deformed configurations. The two 0^+ states are thus an example of shape coexistence with two distinct shapes close in excitation energy. This is in line with the simple picture presented in Section 1.4.1. The shape-coexisting feature of the 2^+_1 and 2^+_2 states is also seen, but with a higher degree of shape mixing. Given that the ground state of ^{31}Mg is characterized by a prolate-deformed shape (see also Figure 6.10), spectroscopic factors resulting from the SDPF-M interaction presented in Figure 6.4 can be intuitively understood as follows.

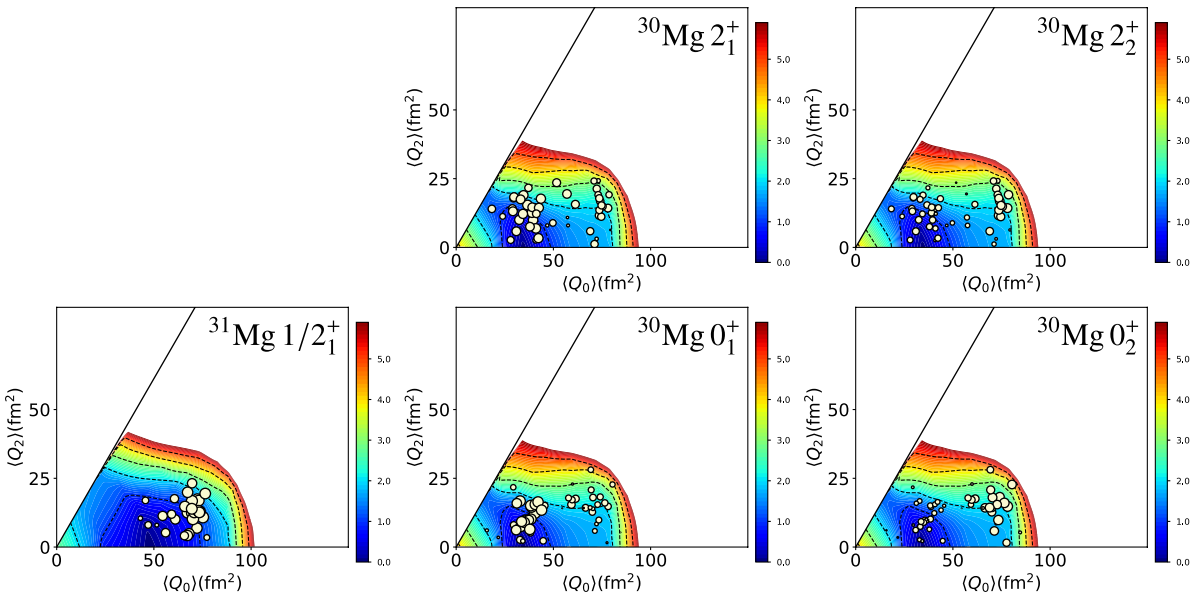

Figure 6.10: T-plots for the 0_1^+, 2_1^+, 0_2^+, and 2_2^+ states in ^{30}Mg and the $1/2^+$ state in ^{31}Mg produced using the SDPF-M interaction.

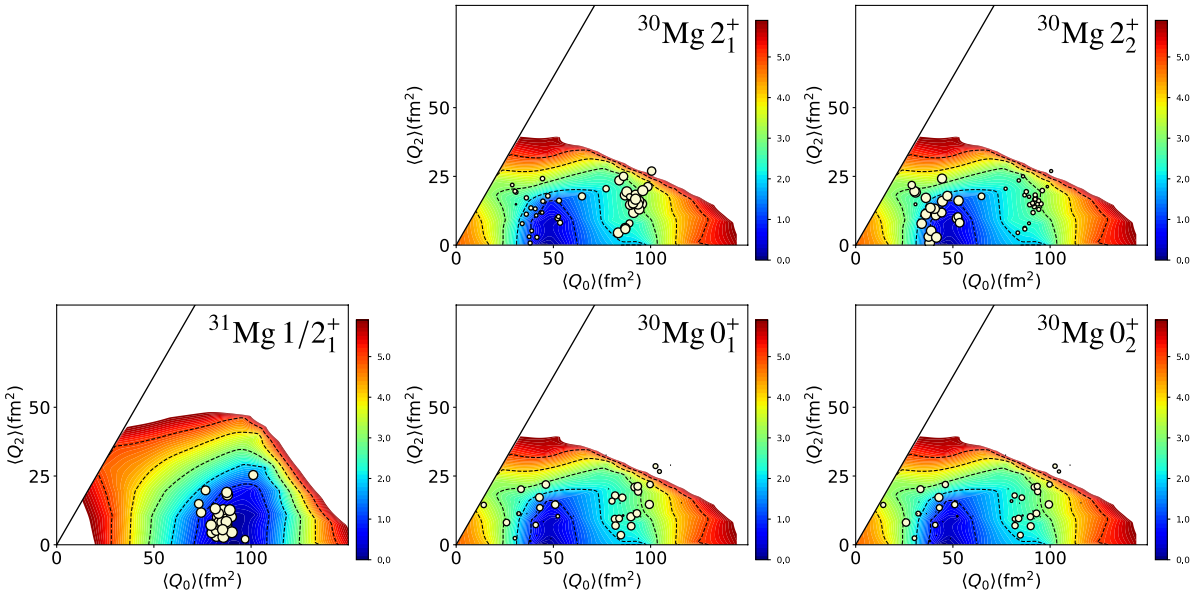

Figure 6.11: Same as Figure 6.10 but with the EEdf1 interaction.

The 0_1^+ spectroscopic factor is small as the 0_1^+ state is characterized by a spherical shape and the overlap of the wave functions is small. On the other hand, the 0_2^+ state is described by deformed configurations, thus yielding a large spectroscopic factor. The spectroscopic factors of the 2_1^+ and 2_2^+ states are of similar magnitude because of the large shape fluctuation. The experimental spectroscopic factors may be intuitively interpreted in this way.

T-plots resulting from the EEdf1 interaction are shown in Figure 6.11. The shape mixing of the 0_1^+ and 0_2^+ states is much more pronounced, in stark contrast with the T-plots presented in Figure 6.10 and with the conventional picture of the shape coexistence in ^{30}Mg. Interestingly, the shape-coexisting feature of the 2_1^+ and 2_2^+ states is "inverted", i.e. the 2_1^+ is described by a clear deformed shape and the 2_2^+ is almost spherical. The large (small) spectroscopic factors for the 2_1^+ (2_2^+) states calculated by the EEdf1 interaction can also be intuitively understood in terms of the shape overlap, as the ground state of ^{31}Mg is characterized by a prolate-deformed shape.

Despite the similar level schemes, the two interactions thus predict very different structures for ^{30}Mg. Usually, excitation energies are used as the first test of theory, but more detailed experimental information, such as electromagnetic transition strengths and spectroscopic factors, is required to further differentiate the models.

6.5 Summary

This section summarizes the experimental and theoretical findings. One of the highlights of the present work is the establishment of the location of the negative-parity states. A negative-parity candidate at 2467 keV proposed by Fernández-Domínguez *et al.* [48] was assigned as positive parity in the present work. This state is highly likely to be the 2_2^+ state from the systematics of neighboring nuclei, and this interpretation is also supported by shell-model calculations. Another candidate for a negative-parity state at 2541 keV was proposed by Deacon *et al.* [47]. The corresponding state was not observed in this experiment. The firmly established γ-ray cascade from this work suggests that the γ-γ analysis in [47] is affected by misidentified γ rays, requiring the re-ordering of their level scheme.

The 4_1^+ state at 3379 keV, whose spin-parity was originally assigned by Deacon *et al.* [47], was strongly populated in multi-nucleon removal reactions. In the one-neutron knockout reaction, the momentum distribution of this state was not compatible with reaction calculations, indicating an indirect population mechanism. These add to evidence of the 4_1^+ assignment. The 4_1^+ state at 3379 keV leads to $R_{42} = 2.3$, which is close to the vibrational limit. From the analyses of the multi-nucleon removal reactions, a candidate for the $J = 5$ yrast state at 4183 keV [47] was observed in the present experiment. It is also proposed that the state at 4260 keV has a high-spin ($J \geq 4$) character.

The state at 3302 keV was firmly assigned as a 3^- negative-parity state from the momentum distribution strongly supporting $1f_{7/2}$ knockout. This is considered as the lowest negative-parity state in ^{30}Mg. The states at 3540 keV, 4258 keV, and 5210 keV were assigned as negative-parity states with spin-parities of 1^-, $(4)^-$, and $(2)^-$, respectively. The 5210-keV state was observed for the first time in this work.

From the systematic analysis of $N = 18$ isotones, the excitation energies of the negative-parity states drop at ^{30}Mg, indicating a precursory structural change approaching the island of inversion. The observed energy drop is not as large as the one derived from the previous studies [47,48], but still significant. In the framework of the shell model, this could be attributed to the reduction of the ESPE gap at $N = 20$.

Large spectroscopic strengths arising from the $1f_{7/2}$ and $2p_{3/2}$ orbitals are in line with an intruder-dominated configuration of the ground state of ^{31}Mg. At the same time, from the systematics of the spectroscopic strength to negative-parity states in the neighboring nuclei ^{29}Mg and ^{31}Mg, the current data of ^{30}Mg show a transitional situation, locating ^{31}Mg the shore

of the island of inversion.

The overall level structure is very well reproduced by large-scale shell-model calculations employing the SDPF-M, EEdf1, and SDPF-U-MIX interactions. However, disagreements were found in the spectroscopic factors. The present data and calculations did not allow for a definitive choice of shell-model interactions, and it remains a challenge for the shell model to reproduce the experimental spectroscopic factors. Additionally, it was suggested that the proper accounting of the $N = 20$ and $N = 28$ gap sizes would be key to better reproduce the experimental spectroscopic factors. The T-plot analysis was performed to differentiate between the SDPF-M and EEdf1 interactions. Interestingly, it was found that these two interactions give very different pictures of shape coexistence. The calculated spectroscopic factors for the 0^+_1, 2^+_1, 0^+_2, and 2^+_2 states could be intuitively understood using the T-plots.

Chapter 7

Conclusion

In this work, the nuclear structure of ^{30}Mg was investigated by in-beam γ-ray spectroscopy to track the structural evolution towards the island of inversion. To populate excited states in ^{30}Mg, the one-neutron knockout reaction from ^{31}Mg was utilized as an established spectroscopic tool. In addition, the multi-nucleon removal reactions from ^{32}Mg, ^{34}Si, and ^{35}P were used to complement the study.

Prior to this work, in-beam γ-ray measurements of ^{30}Mg using the fusion-evaporation reaction ^{14}C(^{18}O,2p) [47] and the one-neutron knockout reaction from ^{31}Mg [48] were reported. These experiments indicated the presence of negative-parity states lying significantly lower in energy than shell-model predictions, and posed questions concerning the theoretical modeling of nuclear structure approaching the island of inversion.

The present measurements allowed for the construction of an updated level scheme for ^{30}Mg by a γ-γ coincidence analysis. Firm spin-parity assignments for states in ^{30}Mg were made based on comparison of the ejectile's parallel momentum distributions to reaction model calculations. This work revealed that the lowest negative-parity state in ^{30}Mg, the 3^-_1 state, lies at 3302 keV. This excitation energy is about 800 keV higher than those proposed by the previous in-beam γ-ray studies. A 1^- state was identified at 3540 keV. Other negative-parity states also were found at 4158 keV and 5210 keV. The state at 2467 keV, which was thought to have negative parity in the previous one-neutron knockout measurement, was assigned as the 2^+_2 state. Analyses on the multi-nucleon removal reactions provided additional support on the high-spin yrast nature of the states observed at 3379 keV, 4162 keV, and 4183 keV. This is in line with the interpretation that the 3379-keV state corresponds to the 4^+ state as a member of the ground-state band. With the updated level scheme for ^{30}Mg, the systematic trend of the observed negative-parity states along the even-even $N = 18$ isotones was discussed. A decrease of the excitation energies of the negative-parity states going from Si ($Z = 14$) to Mg ($Z = 12$) was confirmed. Even though the drop is not as steep as those proposed in the previous studies, this was interpreted in terms of the reduction of the $N = 20$ gap and thus an early structural change approaching the island of inversion.

The knockout cross sections associated with each state and therefore spectroscopic factors have also been deduced. The spectroscopic factors for populating negative-parity states in ^{30}Mg were found to be large, and this can be attributed to an intruder-dominated configuration in the ground state of ^{31}Mg. Additionally, sizable spectroscopic factors originating from the knockout from the $2p_{3/2}$ orbital point to a significant occupation of this orbital in ^{31}Mg. These new experimental results offered more insights into the structural evolution approaching the island

of inversion.

The resulting level scheme and spectroscopic factors were then compared to large-scale shell-model calculations. The overall level structure, including the location of the negative-parity states, is remarkably well reproduced by the calculations without much sensitivity to the shell-model interaction being used. However, the complete reproduction of the observed spectroscopic factors remains a challenge to the current shell model. While the calculation using the EEdf1 interaction agrees with the experimental spectroscopic factors associated with knockout from the fp shell, the ones associated with the sd shell tend to be in better agreement with the SDPF-M interaction. The importance of the proper accounting of the $N = 20$ and $N = 28$ gap sizes in reproducing the experimental spectroscopic factors has been suggested. This new experimental information will serve as a benchmark for theoretical models towards the full description of the nuclear structure in and around the island of inversion.

To get more insight into the pictures brought by these interactions, the intrinsic nuclear shapes were visualized by T-plots. Despite the similarity in the calculated level structure, it turned out that the SDPF-M and EEdf1 interactions give very different pictures of shape coexistence in ^{30}Mg. The result obtained with the SDPF-M interaction is closer to the conventional picture, while the EEdf1 interaction presents substantial shape mixing and fluctuation in the 0^+ states. This poses a further challenge to nuclear theories towards a complete understanding of the transition into the island of inversion.

The obvious experimental next step would be in-beam γ-ray spectroscopy of ^{28}Ne ($Z = 10$, $N = 18$) and ^{32}Mg ($Z = 12, N = 20$) by neutron knockout, to further track the structural evolution towards more exotic nuclei. Detailed spectroscopy of even-odd nuclei in this region would be equally important. In the present experiment, the pandemonium effect inherent to γ-tagged measurements on collective even-even nuclei is suggested to be the cause of the overestimated spectroscopic factors of the low-lying states. As transfer reactions with the missing-mass method are free from this effect, the (p, d) reactions on ^{31}Mg could be exploited to better constrain the low-lying spectroscopic factors. Spectroscopic factors from the ^{30}Mg(d, p) reaction are expected to shed more light on the transition into the island of inversion. To further elucidate shape-coexistence in ^{30}Mg, an improved Coulomb excitation measurement would be beneficial. The existing Coulomb excitation experiments on ^{30}Mg reported only the population of the first 2^+ state [58]. In principle, low-energy multiple Coulomb excitation can populate not only the first 2^+ but also many other states by multi-step excitation. It also provides $E2$ matrix elements and spectroscopic quadrupole moments, which are essential for discussing the shape transitions within a nucleus.

Bibliography

[1] W. M. Elsasser. Sur le principe de pauli dans les noyaux. *Journal de physique et Le Radium*, 4:549, 1933.

[2] S. Wong. *Introductory Nuclear Physics*. Wiley, 1999.

[3] Meng Wang, G. Audi, F. G. Kondev, W. J. Huang, S. Naimi, and Xing Xu. The AME2016 atomic mass evaluation (II). tables, graphs and references. *Chinese Physics C*, 41(3):030003, 2017.

[4] Evaluated Nuclear Structure Data File. `https://www.nndc.bnl.gov/ensdf/`.

[5] Maria Goeppert Mayer. On closed shells in nuclei. II. *Physical Review*, 75:1969–1970, 1949.

[6] Otto Haxel, J. Hans D. Jensen, and Hans E. Suess. On the "magic numbers" in nuclear structure. *Physical Review*, 75:1766–1766, 1949.

[7] O. Sorlin and M.-G. Porquet. Nuclear magic numbers: New features far from stability. *Progress in Particle and Nuclear Physics*, 61(2):602–673, 2008.

[8] I. Talmi and I. Unna. Order of levels in the shell model and spin of Be^{11}. *Physical Review Letters*, 4:469–470, 1960.

[9] A. Navin, D. W. Anthony, T. Aumann, T. Baumann, D. Bazin, Y. Blumenfeld, B. A. Brown, T. Glasmacher, P. G. Hansen, R. W. Ibbotson, P. A. Lofy, V. Maddalena, K. Miller, T. Nakamura, B. V. Pritychenko, B. M. Sherrill, E. Spears, M. Steiner, J. A. Tostevin, J. Yurkon, and A. Wagner. Direct evidence for the breakdown of the $N = 8$ shell closure in ^{12}Be. *Physical Review Letters*, 85:266–269, 2000.

[10] B. Bastin, S. Grévy, D. Sohler, O. Sorlin, Zs. Dombrádi, N. L. Achouri, J. C. Angélique, F. Azaiez, D. Baiborodin, R. Borcea, C. Bourgeois, A. Buta, A. Bürger, R. Chapman, J. C. Dalouzy, Z. Dlouhy, A. Drouard, Z. Elekes, S. Franchoo, S. Iacob, B. Laurent, M. Lazar, X. Liang, E. Liénard, J. Mrazek, L. Nalpas, F. Negoita, N. A. Orr, Y. Penionzhkevich, Zs. Podolyák, F. Pougheon, P. Roussel-Chomaz, M. G. Saint-Laurent, M. Stanoiu, I. Stefan, F. Nowacki, and A. Poves. Collapse of the $N = 28$ shell closure in ^{42}Si. *Physical Review Letters*, 99:022503, 2007.

[11] R. Kanungo, C. Nociforo, A. Prochazka, T. Aumann, D. Boutin, D. Cortina-Gil, B. Davids, M. Diakaki, F. Farinon, H. Geissel, R. Gernhäuser, J. Gerl, R. Janik, B. Jonson, B. Kindler, R. Knöbel, R. Krücken, M. Lantz, H. Lenske, Y. Litvinov, B. Lommel, K. Mahata,

P. Maierbeck, A. Musumarra, T. Nilsson, T. Otsuka, C. Perro, C. Scheidenberger, B. Sitar, P. Strmen, B. Sun, I. Szarka, I. Tanihata, Y. Utsuno, H. Weick, and M. Winkler. One-neutron removal measurement reveals ^{24}O as a new doubly magic nucleus. *Physical Review Letters*, 102:152501, 2009.

[12] E. K. Warburton, J. A. Becker, and B. A. Brown. Mass systematics for $A = 29$–44 nuclei: The deformed $A \sim 32$ region. *Physical Review C*, 41:1147–1166, 1990.

[13] E. Caurier, F. Nowacki, and A. Poves. Merging of the islands of inversion at $N = 20$ and $N = 28$. *Physical Review C*, 90:014302, 2014.

[14] G. Neyens, M. Kowalska, D. Yordanov, K. Blaum, P. Himpe, P. Lievens, S. Mallion, R. Neugart, N. Vermeulen, Y. Utsuno, and T. Otsuka. Measurement of the spin and magnetic moment of ^{31}Mg: Evidence for a strongly deformed intruder ground state. *Physical Review Letters*, 94:022501, 2005.

[15] R. Klapisch, C. Thibault-Philippe, C. Detraz, J. Chaumont, R. Bernas, and E. Beck. Half-life of ^{11}Li, of ^{27}Na, and of the new isotopes ^{28}Na, ^{29}Na, ^{30}Na, and ^{31}Na produced in high-energy nuclear reactions. *Physical Review Letters*, 23:652–655, 1969.

[16] C. Thibault, R. Klapisch, C. Rigaud, A. M. Poskanzer, R. Prieels, L. Lessard, and W. Reisdorf. Direct measurement of the masses of ^{11}Li and $^{26–32}$Mg with an on-line mass spectrometer. *Physical Review C*, 12:644–657, 1975.

[17] C. Détraz, M. Langevin, D. Guillemaud, M. Epherre, G. Audi, C. Thibault, and F. Touchard. Mapping of the onset of a new region of deformation: The masses of ^{31}Mg and ^{32}Mg. *Nuclear Physics A*, 394(3):378–386, 1983.

[18] N. A. Orr, W. Mittig, L. K. Fifield, M. Lewitowicz, E. Plagnol, Y. Schutz, Zhan Wen Long, L. Bianchi, A. Gillibert, A. V. Belozyorov, S. M. Lukyanov, Yu. E. Penionzhkevich, A. C. C. Villari, A. Cunsolo, A. Foti, G. Audi, C. Stephan, and L. Tassan-Got. New mass measurements of neutron-rich nuclei near $N = 20$. *Physics Letters B*, 258(1):29–34, 1991.

[19] C. Détraz, D. Guillemaud, G. Huber, R. Klapisch, M. Langevin, F. Naulin, C. Thibault, L. C. Carraz, and F. Touchard. Beta decay of $^{27\text{-}32}$Na and their descendants. *Physical Review C*, 19:164–176, 1979.

[20] H. Iwasaki, T. Motobayashi, H. Sakurai, K. Yoneda, T. Gomi, N. Aoi, N. Fukuda, Zs. Fülöp, U. Futakami, Z. Gacsi, Y. Higurashi, N. Imai, N. Iwasa, T. Kubo, M. Kunibu, M. Kurokawa, Z. Liu, T. Minemura, A. Saito, M. Serata, S. Shimoura, S. Takeuchi, Y. X. Watanabe, K. Yamada, Y. Yanagisawa, and M. Ishihara. Large collectivity of ^{34}Mg. *Physics Letters B*, 522(3):227–232, 2001.

[21] Y. Yanagisawa, M. Notani, H. Sakurai, M. Kunibu, H. Akiyoshi, N. Aoi, H. Baba, K. Demichi, N. Fukuda, H. Hasegawa, Y. Higurashi, M. Ishihara, N. Iwasa, H. Iwasaki, T. Gomi, S. Kanno, M. Kurokawa, Y. U. Matsuyama, S. Michimasa, T. Minemura, T. Mizoi, T. Nakamura, A. Saito, M. Serata, S. Shimoura, T. Sugimoto, E. Takeshita, S. Takeuchi, K. Ue, K. Yamada, K. Yoneda, and T. Motobayashi. The first excited state

of ^{30}Ne studied by proton inelastic scattering in reversed kinematics. *Physics Letters B*, 566(1):84–89, 2003.

[22] T. Motobayashi, Y. Ikeda, K. Ieki, M. Inoue, N. Iwasa, T. Kikuchi, M. Kurokawa, S. Moriya, S. Ogawa, H. Murakami, S. Shimoura, Y. Yanagisawa, T. Nakamura, Y. Watanabe, M. Ishihara, T. Teranishi, H. Okuno, and R. F. Casten. Large deformation of the very neutron-rich nucleus ^{32}Mg from intermediate-energy coulomb excitation. *Physics Letters B*, 346(1):9–14, 1995.

[23] X. Campi, H. Flocard, A. K. Kerman, and S. Koonin. Shape transition in the neutron rich sodium isotopes. *Nuclear Physics A*, 251(2):193–205, 1975.

[24] B. H. Wildenthal and W. Chung. Collapse of the conventional shell-model ordering in the very-neutron-rich isotopes of na and mg. *Physical Review C*, 22:2260–2262, 1980.

[25] J. R. Terry, B. A. Brown, C. M. Campbell, J. M. Cook, A. D. Davies, D.-C. Dinca, A. Gade, T. Glasmacher, P. G. Hansen, B. M. Sherrill, H. Zwahlen, D. Bazin, K. Yoneda, J. A. Tostevin, T. Otsuka, Y. Utsuno, and B. Pritychenko. Single-neutron knockout from intermediate energy beams of ^{30,32}Mg: Mapping the transition into the "island of inversion". *Physical Review C*, 77:014316, 2008.

[26] Kris Heyde and John L. Wood. Shape coexistence in atomic nuclei. *Review of Modern Physics*, 83:1467–1521, 2011.

[27] W. Schwerdtfeger, P. G. Thirolf, K. Wimmer, D. Habs, H. Mach, T. R. Rodriguez, V. Bildstein, J. L. Egido, L. M. Fraile, R. Gernhäuser, R. Hertenberger, K. Heyde, P. Hoff, H. Hübel, U. Köster, T. Kröll, R. Krücken, R. Lutter, T. Morgan, and P. Ring. Shape coexistence near neutron number $N = 20$: First identification of the $E0$ decay from the deformed first excited $J^\pi = 0^+$ state in ^{30}Mg. *Physical Review Letters*, 103:012501, 2009.

[28] K. Wimmer, T. Kröll, R. Krücken, V. Bildstein, R. Gernhäuser, B. Bastin, N. Bree, J. Diriken, P. Van Duppen, M. Huyse, N. Patronis, P. Vermaelen, D. Voulot, J. Van de Walle, F. Wenander, L. M. Fraile, R. Chapman, B. Hadinia, R. Orlandi, J. F. Smith, R. Lutter, P. G. Thirolf, M. Labiche, A. Blazhev, M. Kalkühler, P. Reiter, M. Seidlitz, N. Warr, A. O. Macchiavelli, H. B. Jeppesen, E. Fiori, G. Georgiev, G. Schrieder, S. Das Gupta, G. Lo Bianco, S. Nardelli, J. Butterworth, J. Johansen, and K. Riisager. Discovery of the shape coexisting 0^+ state in ^{32}Mg by a two neutron transfer reaction. *Physical Review Letters*, 105:252501, 2010.

[29] F. Rotaru, F. Negoita, S. Grévy, J. Mrazek, S. Lukyanov, F. Nowacki, A. Poves, O. Sorlin, C. Borcea, R. Borcea, A. Buta, L. Cáceres, S. Calinescu, R. Chevrier, Zs. Dombrádi, J. M. Daugas, D. Lebhertz, Y. Penionzhkevich, C. Petrone, D. Sohler, M. Stanoiu, and J. C. Thomas. Unveiling the intruder deformed 0_2^+ state in ^{34}Si. *Physical Review Letters*, 109:092503, 2012.

[30] N. A. Smirnova, B. Bally, K. Heyde, F. Nowacki, and K. Sieja. Shell evolution and nuclear forces. *Physics Letters B*, 686(2):109–113, 2010.

[31] Takaharu Otsuka, Toshio Suzuki, Rintaro Fujimoto, Hubert Grawe, and Yoshinori Akaishi. Evolution of nuclear shells due to the tensor force. *Physical Review Letters*, 95:232502, 2005.

[32] Takaharu Otsuka, Alexandra Gade, Olivier Sorlin, Toshio Suzuki, and Yutaka Utsuno. Evolution of nuclear structure in exotic nuclei driven by nuclear forces, 2018. arXiv:1805.06501.

[33] Takaharu Otsuka, Rintaro Fujimoto, Yutaka Utsuno, B. Alex Brown, Michio Honma, and Takahiro Mizusaki. Magic numbers in exotic nuclei and spin-isospin properties of the *nn* interaction. *Physical Review Letters*, 87:082502, 2001.

[34] Takaharu Otsuka, Toshio Suzuki, Michio Honma, Yutaka Utsuno, Naofumi Tsunoda, Koshiroh Tsukiyama, and Morten Hjorth-Jensen. Novel features of nuclear forces and shell evolution in exotic nuclei. *Physical Review Letters*, 104:012501, 2010.

[35] B. H. Wildenthal. Empirical strengths of spin operators in nuclei. *Progress in Particle and Nuclear Physics*, 11:5–51, 1984.

[36] B. A. Brown and B. H. Wildenthal. Status of the nuclear shell model. *Annual Review of Nuclear and Particle Science*, 38(1):29–66, 1988.

[37] Yutaka Utsuno, Takaharu Otsuka, Takahiro Mizusaki, and Michio Honma. Varying shell gap and deformation in $N \sim 20$ unstable nuclei studied by the monte carlo shell model. *Physical Review C*, 60:054315, 1999.

[38] T. T. S. Kuo and G. E. Brown. Reaction matrix elements for the 0f-1p shell nuclei. *Nuclear Physics A*, 114(2):241–279, 1968.

[39] D. J. Millener and D. Kurath. The particle-hole interaction and the beta decay of ^{14}B. *Nuclear Physics A*, 255(2):315–338, 1975.

[40] F. Nowacki and A. Poves. New effective interaction for $0\hbar\omega$ shell-model calculations in the sd-pf valence space. *Physical Review C*, 79:014310, 2009.

[41] Naofumi Tsunoda, Takaharu Otsuka, Noritaka Shimizu, Morten Hjorth-Jensen, Kazuo Takayanagi, and Toshio Suzuki. Exotic neutron-rich medium-mass nuclei with realistic nuclear forces. *Physical Review C*, 95:021304, 2017.

[42] R. Rodríguez-Guzmán, J. L. Egido, and L. M. Robledo. Correlations beyond the mean field in magnesium isotopes: angular momentum projection and configuration mixing. *Nuclear Physics A*, 709(1):201–235, 2002.

[43] Tomás R. Rodríguez and J. Luis Egido. New beyond-mean-field theories: Examination of the potential shell closures at $N = 32$ or 34. *Physical Review Letters*, 99:062501, 2007.

[44] T. Rodriguez and J. L. Egido. private communication.

[45] Nobuo Hinohara, Koichi Sato, Kenichi Yoshida, Takashi Nakatsukasa, Masayuki Matsuo, and Kenichi Matsuyanagi. Shape fluctuations in the ground and excited 0^+ states of ^{30,32,34}Mg. *Physical Review C*, 84:061302, 2011.

[46] H. Iwasaki, T. Motobayashi, H. Akiyoshi, Y. Ando, N. Fukuda, H. Fujiwara, Zs. Fülöp, K. I. Hahn, Y. Higurashi, M. Hirai, I. Hisanaga, N. Iwasa, T. Kijima, A. Mengoni, T. Minemura, T. Nakamura, M. Notani, S. Ozawa, H. Sagawa, H. Sakurai, S. Shimoura, S. Takeuchi, T. Teranishi, Y. Yanagisawa, and M. Ishihara. Low-lying intruder 1^- state in ^{12}Be and the melting of the $N = 8$ shell closure. *Physics Letters B*, 491(1):8–14, 2000.

[47] A. N. Deacon, J. F. Smith, S. J. Freeman, R. V. F. Janssens, M. P. Carpenter, B. Hadinia, C. R. Hoffman, B. P. Kay, T. Lauritsen, C. J. Lister, D. O'Donnell, J. Ollier, T. Otsuka, D. Seweryniak, K.-M. Spohr, D. Steppenbeck, S. L. Tabor, V. Tripathi, Y. Utsuno, P. T. Wady, and S. Zhu. Cross-shell excitations near the "island of inversion": Structure of ^{30}Mg. *Physical Review C*, 82:034305, 2010.

[48] B. Fernández-Domínguez, B. Pietras, W. N. Catford, N. A. Orr, M. Petri, M. Chartier, S. Paschalis, N. Patterson, J. S. Thomas, M. Caamaño, T. Otsuka, A. Poves, N. Tsunoda, N. L. Achouri, J.-C. Angélique, N. I. Ashwood, A. Banu, B. Bastin, R. Borcea, J. Brown, F. Delaunay, S. Franchoo, M. Freer, L. Gaudefroy, S. Heil, M. Labiche, B. Laurent, R. C. Lemmon, A. O. Macchiavelli, F. Negoita, E. S. Paul, C. Rodríguez-Tajes, P. P. Roussel-Chomaz, M. Staniou, M. J. Taylor, L. Trache, and G. L. Wilson. Re-examining the transition into the $N = 20$ island of inversion: Structure of ^{30}Mg. *Physics Letters B*, 779:124–129, 2018.

[49] Vandana Tripathi, S. L. Tabor, P. Bender, C. R. Hoffman, Sangjin Lee, K. Pepper, M. Perry, P. F. Mantica, J. M. Cook, J. Pereira, J. S. Pinter, J. B. Stoker, D. Weisshaar, Y. Utsuno, and T. Otsuka. Excited intruder states in ^{32}Mg. *Physical Review C*, 77:034310, 2008.

[50] D. Guillemaud-Mueller, C. Detraz, M. Langevin, F. Naulin, M. de Saint-Simon, C. Thibault, F. Touchard, and M. Epherre. β-decay schemes of very neutron-rich sodium isotopes and their descendants. *Nuclear Physics A*, 426(1):37–76, 1984.

[51] P. Baumann, Ph. Dessagne, A. Huck, G. Klotz, A. Knipper, Ch. Miehé, M. Ramdane, G. Walter, G. Marguier, H. Gabelmann, C. Richard-Serre, K. Schlösser, and A. Poves. Beta decay of ^{30}Na: Experiment and theory. *Physical Review C*, 39:626–635, 1989.

[52] G. Klotz, P. Baumann, M. Bounajma, A. Huck, A. Knipper, G. Walter, G. Marguier, C. Richard-Serre, A. Poves, and J. Retamosa. Beta decay of ^{31,32}Na and ^{31}Mg: Study of the $N = 20$ shell closure. *Physical Review C*, 47:2502–2516, 1993.

[53] H. Mach, L. M. Fraile, O. Tengblad, R. Boutami, C. Jollet, W. A. Płóciennik, D. T. Yordanov, M. Stanoiu, M. J. G. Borge, P. A. Butler, J. Cederkäll, Ph. Dessagne, B. Fogelberg, H. Fynbo, P. Hoff, A. Jokinen, A. Korgul, U. Köster, W. Kurcewicz, F. Marechal, T. Motobayashi, J. Mrazek, G. Neyens, T. Nilsson, S. Pedersen, A. Poves, B. Rubio, E. Ruchowska, and the ISOLDE Collaboration. New structure information on ^{30}Mg, ^{31}Mg and ^{32}Mg. *European Physical Journal A*, 25(1):105–109, 2005.

[54] C. M. Mattoon, F. Sarazin, G. Hackman, E. S. Cunningham, R. A. E. Austin, G. C. Ball, R. S. Chakrawarthy, P. Finlay, P. E. Garrett, G. F. Grinyer, B. Hyland, K. A. Koopmans, J. R. Leslie, A. A. Phillips, M. A. Schumaker, H. C. Scraggs, J. Schwarzenberg, M. B. Smith, C. E. Svensson, J. C. Waddington, P. M. Walker, B. Washbrook, and E. Zganjar. β decay of ^{32}Na. *Physical Review C*, 75:017302, 2007.

[55] T. Shimoda, K. Tajiri, K. Kura, A. Odahara, M. Suga, Y. Hirayama, N. Imai, H. Miyatake, M. Pearson, C. D. P. Levy, K. P. Jackson, R. Legillon, C. Petrache, T. Fukuchi, N. Hamatani, T. Hori, M. Kazato, Y. Kenmoku, T. Masue, H. Nishibata, T. Suzuki, A. Takashima, and R. Yokoyama. Nuclear structure explored by β-delayed decay spectroscopy of spin-polarized radioactive nuclei at TRIUMF ISAC-1. *Hyperfine Interactions*, 225(1):183–191, 2014.

[56] B. V. Pritychenko, T. Glasmacher, P. D. Cottle, M. Fauerbach, R. W. Ibbotson, K. W. Kemper, V. Maddalena, A. Navin, R. Ronningen, A. Sakharuk, H. Scheit, and V. G. Zelevinsky. Role of intruder configurations in ^{26,28}Ne and ^{30,32}Mg. *Physics Letters B*, 461(4):322–328, 1999.

[57] V. Chisté, A. Gillibert, A Lépine-Szily, N. Alamanos, F. Auger, J. Barrette, F. Braga, M. D.-Gil Cortina, Z. Dlouhy, V. Lapoux, M. Lewitowicz, R. Lichtenthäler, R. Liguori Neto, S. M. Lukyanov, M. MacCormick, F. Marie, W. Mittig, F. de Oliveira Santos, N. A. Orr, A. N. Ostrowski, S. Ottini, A. Pakou, Yu. E. Penionzhkevich, P. Roussel-Chomaz, and J. L. Sida. Electric and nuclear transition strength in ^{30,32}Mg. *Physics Letters B*, 514(3):233–239, 2001.

[58] O. Niedermaier, H. Scheit, V. Bildstein, H. Boie, J. Fitting, R. von Hahn, F. Köck, M. Lauer, U. K. Pal, H. Podlech, R. Repnow, D. Schwalm, C. Alvarez, F. Ames, G. Bollen, S. Emhofer, D. Habs, O. Kester, R. Lutter, K. Rudolph, M. Pasini, P. G. Thirolf, B. H. Wolf, J. Eberth, G. Gersch, H. Hess, P. Reiter, O. Thelen, N. Warr, D. Weisshaar, F. Aksouh, P. Van den Bergh, P. Van Duppen, M. Huyse, O. Ivanov, P. Mayet, J. Van de Walle, J. Äystö, P. A. Butler, J. Cederkäll, P. Delahaye, H. O. U. Fynbo, L. M. Fraile, O. Forstner, S. Franchoo, U. Köster, T. Nilsson, M. Oinonen, T. Sieber, F. Wenander, M. Pantea, A. Richter, G. Schrieder, H. Simon, T. Behrens, R. Gernhäuser, T. Kröll, R. Krücken, M. Münch, T. Davinson, J. Gerl, G. Huber, A. Hurst, J. Iwanicki, B. Jonson, P. Lieb, L. Liljeby, A. Schempp, A. Scherillo, P. Schmidt, and G. Walter. "safe" coulomb excitation of ^{30}Mg. *Physical Review Letters*, 94:172501, 2005.

[59] S. Takeuchi, N. Aoi, T. Motobayashi, S. Ota, E. Takeshita, H. Suzuki, H. Baba, T. Fukui, Y. Hashimoto, K. Ieki, N. Imai, H. Iwasaki, S. Kanno, Y. Kondo, T. Kubo, K. Kurita, T. Minemura, T. Nakabayashi, T. Nakamura, T. Okumura, T. K. Onishi, H. Sakurai, S. Shimoura, R. Sugou, D. Suzuki, M. K. Suzuki, M. Takashina, M. Tamaki, K. Tanaka, Y. Togano, and K. Yamada. Low-lying states in ^{32}Mg studied by proton inelastic scattering. *Physical Review C*, 79:054319, 2009.

[60] M. Shamsuzzoha Basunia. Nuclear data sheets for $A = 30$. *Nuclear Data Sheets*, 111(9):2331–2424, 2010.

[61] A. G. Artukh, V. V. Avdeichikov, G. F. Gridnev, V. L. Mikheev, V. V. Volkov, and J. Wilczyński. New isotopes ^{29,30}Mg, ^{31,32,33}Al, ^{33,34,35,36}Si, ^{35,36,37,38}P, ^{39,40}S and ^{41,42}Cl produced in bombardment of a ^{232}Th target with 290 MeV ^{40}Ar ions. *Nuclear Physics A*, 176(2):284–288, 1971.

[62] E. Roeckl, P. F. Dittner, C. Détraz, R. Klapisch, C. Thibault, and C. Rigaud. Decay properties of the neutron-rich isotopes, ^{11}Li and $^{27–31}$Na. *Physical Review C*, 10:1181–1188, 1974.

[63] I. Paschopoulos, Eckhardt Müller, H. J. Körner, I. C. Oelrich, K. E. Rehm, and H. J. Scheerer. Energy levels of ^{27}Na and masses of ^{29,30}Mg observed in ^{18}O-induced transfer reactions on ^{26}Mg. *Physical Review C*, 18:1277–1281, 1978.

[64] H. Morinaga and P. C. Gugelot. Gamma rays following (α, xn) reactions. *Nuclear Physics*, 46:210–224, 1963.

[65] T. Shibata, H. Ejiri, J. Chiba, S. Nagamiya, K. Nakai, R. Anholt, H. Bowman, J. G. Ingersoll, E. A. Rauscher, and J. O. Rasmussen. In-beam nuclear gamma-ray studies of relativistic heavy ion reactions. *Nuclear Physics A*, 308(3):513–531, 1978.

[66] M. de Jong, A. V. Ignatyuk, and K.-H. Schmidt. Angular momentum in peripheral fragmentation reactions. *Nuclear Physics A*, 613(4):435–444, 1997.

[67] M. Belleguic, M. J. Lopez-Jimenez, M. Stanoiu, F. Azaiez, M. G. Saint-Laurent, O. Sorlin, N. L. Achouri, J. C. Angélique, C. Borcea, C. Bourgeois, J. M. Daugas, C. Donzaud, F De Oliveira-Santos, Z. Dlouhy, J. Duprat, S. Grevy, D. Guillemaud-Mueller, S. Leenhardt, M. Lewitowicz, W. Mittig, A. C. Mueller, N. Orr, Yu. E. Penionzhkevich, M. G. Porquet, F. Pougheon, P. Roussel-Chomaz, J. E. Sauvestre, H. Savajols, and Yu. Sobolov. In-beam gamma spectroscopy of very neutron-rich nuclei at GANIL. *Physica Scripta*, T88(1):122, 2000.

[68] Alexandra Gade and Thomas Glasmacher. In-beam nuclear spectroscopy of bound states with fast exotic ion beams. *Progress in Particle and Nuclear Physics*, 60(1):161–224, 2008.

[69] J. A. Tostevin. Single-nucleon knockout reactions at fragmentation beam energies. *Nuclear Physics A*, 682(1):320–331, 2001.

[70] P. G. Hansen and J. A. Tostevin. Direct reactions with exotic nuclei. *Annual Review of Nuclear and Particle Science*, 53(1):219–261, 2003.

[71] C. A. Bertulani and A. Gade. MOMDIS: a glauber model computer code for knockout reactions. *Computer Physics Communications*, 175(5):372–380, 2006.

[72] Jim Al-Khalili and Filomena Nunes. Reaction models to probe the structure of light exotic nuclei. *Journal of Physics G: Nuclear and Particle Physics*, 29(11):R89–R132, 2003.

[73] I. J. Thompson and F. M. Nunes. *Nuclear Reactions for Astrophysics*. Cambridge University Press, New Yor, 2009.

[74] B. Alex Brown. New skyrme interaction for normal and exotic nuclei. *Physical Review C*, 58:220–231, 1998.

[75] A. Gade, P. Adrich, D. Bazin, M. D. Bowen, B. A. Brown, C. M. Campbell, J. M. Cook, T. Glasmacher, P. G. Hansen, K. Hosier, S. McDaniel, D. McGlinchery, A. Obertelli, K. Siwek, L. A. Riley, J. A. Tostevin, and D. Weisshaar. Reduction of spectroscopic strength: Weakly-bound and strongly-bound single-particle states studied using one-nucleon knockout reactions. *Physical Review C*, 77:044306, 2008.

[76] H. Esbensen. Momentum distributions in stripping reactions of single-nucleon halo nuclei. *Physical Review C*, 53:2007–2010, 1996.

[77] A. E. L. Dieperink and T. de Forest. Center-of-mass effects in single-nucleon knock-out reactions. *Physical Review C*, 10:543–549, 1974.

[78] J. A. Tostevin and A. Gade. Systematics of intermediate-energy single-nucleon removal cross sections. *Physical Review C*, 90:057602, 2014.

[79] Vijay R. Pandharipande, Ingo Sick, and Peter K. A. deWitt Huberts. Independent particle motion and correlations in fermion systems. *Review of Modern Physics*, 69:981–991, 1997.

[80] Jenny Lee, J. A. Tostevin, B. A. Brown, F. Delaunay, W. G. Lynch, M. J. Saelim, and M. B. Tsang. Reduced neutron spectroscopic factors when using potential geometries constrained by hartree-fock calculations. *Physical Review C*, 73:044608, 2006.

[81] A. Gade and B. M. Sherrill. NSCL and FRIB at Michigan State University: Nuclear science at the limits of stability. *Physica Scripta*, 91(5):053003, 2016.

[82] Y. Blumenfeld, T. Nilsson, and P Van Duppen. Facilities and methods for radioactive ion beam production. *Physica Scripta*, T152:014023, 2013.

[83] W. Gelletly, David J. Morrissey, and Bradley M. Sherrill. Radioactive nuclear beam facilities based on projectile fragmentation. *Philosophical Transactions of the Royal Society of London A: Mathematical, Physical and Engineering*, 356(1744):1985–2006, 1998.

[84] H. Nishibata, T. Shimoda, A. Odahara, S. Morimoto, S. Kanaya, A. Yagi, H. Kanaoka, M. R. Pearson, C. D. P. Levy, and M. Kimura. Shape coexistence in the $N = 19$ neutron-rich nucleus ^{31}Mg explored by β-γ spectroscopy of spin-polarized ^{31}Na. *Physics Letters B*, 767:81–85, 2017.

[85] D. J. Morrissey. The coupled cyclotron project at the NSCL. *Nuclear Physics A*, 616(1):45–55, 1997.

[86] A. S. Goldhaber and H. H. Heckman. High energy interactions of nuclei. *Annual Review of Nuclear and Particle Science*, 28(1):161–205, 1978.

[87] D. J. Morrissey, B. M. Sherrill, M. Steiner, A. Stolz, and I. Wiedenhoever. Commissioning the A1900 projectile fragment separator. *Nuclear Instruments and Methods in Physics Research Section B: Beam Interactions with Materials and Atoms*, 204:90–96, 2003.

[88] A. Stolz, T. Baumann, T. N. Ginter, D. J. Morrissey, M. Portillo, B. M. Sherrill, M. Steiner, and J. W. Stetson. Production of rare isotope beams with the NSCL fragment separator. *Nuclear Instruments and Methods in Physics Research Section B: Beam Interactions with Materials and Atoms*, 241(1):858–861, 2005.

[89] K.-H. Schmidt, E. Hanelt, H. Geissel, G. Münzenberg, and J. P. Dufour. The momentum-loss achromat — a new method for the isotopical separation of relativistic heavy ions. *Nuclear Instruments and Methods in Physics Research Section A: Accelerators, Spectrometers, Detectors and Associated Equipment*, 260(2):287–303, 1987.

[90] D. Bazin, J. A. Caggiano, B. M. Sherrill, J. Yurkon, and A. Zeller. The S800 spectrograph. *Nuclear Instruments and Methods in Physics Research Section B: Beam Interactions with Materials and Atoms*, 204:629–633, 2003.

[91] T. R. Baugher. *Neutron-rich Chromium and Manganese Isotopes and the Role of the* $0g_{9/2}$ *and* $1d_{5/2}$ *Neutron Orbitals in the Region Below* ^{68}Ni. PhD thesis, Michigan State University, 2014.

[92] J. Yurkon, D. Bazin, W. Benenson, D. J. Morrissey, B. M. Sherrill, D. Swan, and R. Swanson. Focal plane detector for the S800 high-resolution spectrometer. *Nuclear Instruments and Methods in Physics Research Section A: Accelerators, Spectrometers, Detectors and Associated Equipment*, 422(1):291–295, 1999.

[93] M. Berz, K. Joh, J. A. Nolen, B. M. Sherrill, and A. F. Zeller. Reconstructive correction of aberrations in nuclear particle spectrographs. *Physical Review C*, 47:537–544, 1993.

[94] Kyoko Makino and Martin Berz. Cosy infinity version 9. *Nuclear Instruments and Methods in Physics Research Section A: Accelerators, Spectrometers, Detectors and Associated Equipment*, 558(1):346–350, 2006.

[95] I. Y. Lee, R. M. Clark, M. Cromaz, M. A. Deleplanque, M. Descovich, R. M. Diamond, P. Fallon, A. O. Macchiavelli, F. S. Stephens, and D. Ward. GRETINA: A gamma ray energy tracking array. *Nuclear Physics A*, 746:255–259, 2004.

[96] I-Yang Lee. Gamma-ray tracking detectors: physics opportunities and status of GRETINA. *Nuclear Physics A*, 834(1):743c–746c, 2010.

[97] Paul Fallon, Alexandra Gade, and I-Yang Lee. GRETINA and its early science. *Annual Review of Nuclear and Particle Science*, 66(1):321–339, 2016.

[98] D. Weisshaar, D. Bazin, P. C. Bender, C. M. Campbell, F. Recchia, V. Bader, T. Baugher, J. Belarge, M. P. Carpenter, H. L. Crawford, M. Cromaz, B. Elman, P. Fallon, A. Forney, A. Gade, J. Harker, N. Kobayashi, C. Langer, T. Lauritsen, I. Y. Lee, A. Lemasson, B. Longfellow, E. Lunderberg, A. O. Macchiavelli, K. Miki, S. Momiyama, S. Noji, D. C. Radford, M. Scott, J. Sethi, S. R. Stroberg, C. Sullivan, R. Titus, A. Wiens, S. Williams, K. Wimmer, and S. Zhu. The performance of the γ-ray tracking array GRETINA for γ-ray spectroscopy with fast beams of rare isotopes. *Nuclear Instruments and Methods in Physics Research Section A: Accelerators, Spectrometers, Detectors and Associated Equipment*, 847:187–198, 2017.

[99] S. Paschalis, I. Y. Lee, A. O. Macchiavelli, C. M. Campbell, M. Cromaz, S. Gros, J. Pavan, J. Qian, R. M. Clark, H. L. Crawford, D. Doering, P. Fallon, C. Lionberger, T. Loew, M. Petri, T. Stezelberger, S. Zimmermann, D. C. Radford, K. Lagergren, D. Weisshaar, R. Winkler, T. Glasmacher, J. T. Anderson, and C. W. Beausang. The performance of the gamma-ray energy tracking in-beam nuclear array GRETINA. *Nuclear Instruments and Methods in Physics Research Section A: Accelerators, Spectrometers, Detectors and Associated Equipment*, 709:44–55, 2013.

[100] Zhong He. Review of the shockleyramo theorem and its application in semiconductor gamma-ray detectors. *Nuclear Instruments and Methods in Physics Research Section A: Accelerators, Spectrometers, Detectors and Associated Equipment*, 463(1):250–267, 2001.

[101] W. F. Mueller, J. A. Church, T. Glasmacher, D. Gutknecht, G. Hackman, P. G. Hansen, Z. Hu, K. L. Miller, and P. Quirin. Thirty-two-fold segmented germanium detectors to identify γ-rays from intermediate-energy exotic beams. *Nuclear Instruments and Methods in Physics Research Section A: Accelerators, Spectrometers, Detectors and Associated Equipment*, 466(3):492–498, 2001.

[102] L. A. Riley. UCGretina.

[103] S. Agostinelli, J. Allison, K. Amako, J. Apostolakis, H. Araujo, P. Arce, M. Asai, D. Axen, S. Banerjee, G. Barrand, F. Behner, L. Bellagamba, J. Boudreau, L. Broglia, A. Brunengo, H. Burkhardt, S. Chauvie, J. Chuma, R. Chytracek, G. Cooperman, G. Cosmo, P. Degtyarenko, A. Dell'Acqua, G. Depaola, D. Dietrich, R. Enami, A. Feliciello, C. Ferguson, H. Fesefeldt, G. Folger, F. Foppiano, A. Forti, S. Garelli, S. Giani, R. Giannitrapani, D. Gibin, J. J. Gómez, Cadenas, I. González, G Gracia Abril, G. Greeniaus, W. Greiner, V. Grichine, A. Grossheim, S. Guatelli, P. Gumplinger, R. Hamatsu, K. Hashimoto, H. Hasui, A. Heikkinen, A. Howard, V. Ivanchenko, A. Johnson, F. W. Jones, J. Kallenbach, N. Kanaya, M. Kawabata, Y. Kawabata, M. Kawaguti, S. Kelner, P. Kent, A. Kimura, T. Kodama, R. Kokoulin, M. Kossov, H. Kurashige, E. Lamanna, T Lampén, V. Lara, V. Lefebure, F. Lei, M. Liendl, W. Lockman, F. Longo, S. Magni, M. Maire, E. Medernach, K. Minamimoto, P. Mora de Freitas, Y. Morita, K. Murakami, M. Nagamatu, R. Nartallo, P. Nieminen, T. Nishimura, K. Ohtsubo, M. Okamura, S. O'Neale, Y. Oohata, K. Paech, J. Perl, A. Pfeiffer, M. G. Pia, F. Ranjard, A. Rybin, S. Sadilov, E. Di Salvo, G. Santin, T. Sasaki, N. Savvas, Y. Sawada, S. Scherer, S. Sei, V. Sirotenko, D. Smith, N. Starkov, H. Stoecker, J. Sulkimo, M. Takahata, S. Tanaka, E. Tcherniaev, E. Safai, Tehrani, M. Tropeano, P. Truscott, H. Uno, L. Urban, P. Urban, M. Verderi, A. Walkden, W. Wander, H. Weber, J. P. Wellisch, T. Wenaus, D. C. Williams, D. Wright, T. Yamada, H. Yoshida, and D. Zschiesche. Geant4—a simulation toolkit. *Nuclear Instruments and Methods in Physics Research Section A: Accelerators, Spectrometers, Detectors and Associated Equipment*, 506(3):250–303, 2003.

[104] *UPDATE OF X RAY AND GAMMA RAY DECAY DATA STANDARDS FOR DETECTOR CALIBRATION AND OTHER APPLICATIONS*. International Atomic Energy Agency, Vienna, 2017.

[105] J. Anderson, R. Brito, D. Doering, T. Hayden, B. Holmes, J. Joseph, H. Yaver, and S. Zimmermann. Data acquisition and trigger system of the Gamma Ray Energy Tracking In-Beam Nuclear Array (GRETINA). *IEEE Transactions on Nuclear Science*, 56(1):258–265, 2009.

[106] M. Cromaz, V. J. Riot, P. Fallon, S. Gros, B. Holmes, I. Y. Lee, A. O. Macchiavelli, C. Vu, H. Yaver, and S. Zimmermann. A digital signal processing module for gamma-ray tracking detectors. *Nuclear Instruments and Methods in Physics Research Section A: Accelerators, Spectrometers, Detectors and Associated Equipment*, 597(2):233–237, 2008.

[107] S. Zimmermann, J. T. Anderson, D. Doering, J. Joseph, C. Lionberger, T. Stezelberger, and H. Yaver. Implementation and performance of the electronics and computing system of the Gamma Ray Energy Tracking In-Beam Nuclear Array (GRETINA). *IEEE Transactions on Nuclear Science*, 59(5):2494–2500, 2012.

[108] K. Wimmer and E. Lunderberg. GrROOT.

[109] S. R. Stroberg, A. Gade, J. A. Tostevin, V. M. Bader, T. Baugher, D. Bazin, J. S. Berryman, B. A. Brown, C. M. Campbell, K. W. Kemper, C. Langer, E. Lunderberg, A. Lemasson, S. Noji, F. Recchia, C. Walz, D. Weisshaar, and S. J. Williams. Single-particle structure of silicon isotopes approaching ^{42}Si. *Physical Review C*, 90:034301, 2014.

[110] Steven Ragnar Stroberg. *Single-particle structure of neutron-rich silicon isotopes and the breakdown of the $N = 28$ shell closure*. PhD thesis, Michigan State University, 2014.

[111] V. Vaquero, A. Jungclaus, J. L. Rodríguez-Sánchez, J. A. Tostevin, P. Doornenbal, K. Wimmer, S. Chen, E. Nácher, E. Sahin, Y. Shiga, D. Steppenbeck, R. Taniuchi, Z. Y. Xu, T. Ando, H. Baba, F. L. Bello, Garrote, S. Franchoo, A. Gargano, K. Hadynska-Klek, A. Kusoglu, J. Liu, T. Lokotko, S. Momiyama, T. Motobayashi, S. Nagamine, N. Nakatsuka, M. Niikura, R. Orlandi, T. Saito, H. Sakurai, P. A. Söderström, G. M. Tveten, Zs. Vajta, and M. Yalcinkaya. Inclusive cross sections for one- and multi-nucleon removal from Sn, Sb, and Te projectiles beyond the $N = 82$ shell closure. *Physics Letters B*, 795:356–361, 2019.

[112] A. Gade, J. A. Tostevin, V. Bader, T. Baugher, D. Bazin, J. S. Berryman, B. A. Brown, D. J. Hartley, E. Lunderberg, F. Recchia, S. R. Stroberg, Y. Utsuno, D. Weisshaar, and K. Wimmer. One-neutron pickup into ^{49}Ca: Bound neutron $g_{9/2}$ spectroscopic strength at $N = 29$. *Physical Review C*, 93:031601, 2016.

[113] Satoru Momiyama. *Collapse of the $N = 28$ shell closure: single-particle structure of ^{43}S*. PhD thesis, The University of Tokyo, 2018.

[114] K. Yoneda, H. Sakurai, T. Gomi, T. Motobayashi, N. Aoi, N. Fukuda, U. Futakami, Z. Gacsi, Y. Higurashi, N. Imai, N. Iwasa, H. Iwasaki, T. Kubo, M. Kunibu, M. Kurokawa, Z. Liu, T. Minemura, A. Saito, M. Serata, S. Shimoura, S. Takeuchi, Y. X. Watanabe, K. Yamada, Y. Yanagisawa, K. Yogo, A. Yoshida, and M. Ishihara. Deformation of ^{34}Mg studied via in-beam γ-ray spectroscopy using radioactive-ion projectile fragmentation. *Physics Letters B*, 499(3):233–237, 2001.

[115] H. L. Crawford, P. Fallon, A. O. Macchiavelli, A. Poves, V. M. Bader, D. Bazin, M. Bowry, C. M. Campbell, M. P. Carpenter, R. M. Clark, M. Cromaz, A. Gade, E. Ideguchi, H. Iwasaki, C. Langer, I. Y. Lee, C. Loelius, E. Lunderberg, C. Morse, A. L. Richard, J. Rissanen, D. Smalley, S. R. Stroberg, D. Weisshaar, K. Whitmore, A. Wiens, S. J. Williams, K. Wimmer, and T. Yamamato. Rotational band structure in ^{32}mg. *Physical Review C*, 93:031303, 2016.

[116] J. C. Hardy, L. C. Carraz, B. Jonson, and P. G. Hansen. The essential decay of pandemonium: A demonstration of errors in complex beta-decay schemes. *Physics Letters B*, 71(2):307–310, 1977.

[117] A. Gade, R. V. F. Janssens, J. A. Tostevin, D. Bazin, J. Belarge, P. C. Bender, S. Bottoni, M. P. Carpenter, B. Elman, S. J. Freeman, T. Lauritsen, S. M. Lenzi, B. Longfellow, E. Lunderberg, A. Poves, L. A. Riley, D. K. Sharp, D. Weisshaar, and S. Zhu. Structure of ^{70}Fe: Single-particle and collective degrees of freedom. *Physical Review C*, 99:011301, 2019.

[118] G. Huber, F. Touchard, S. Büttgenbach, C. Thibault, R. Klapisch, H. T. Duong, S. Liberman, J. Pinard, J. L. Vialle, P. Juncar, and P. Jacquinot. Spins, magnetic moments, and isotope shifts of $^{21-31}$Na by high resolution laser spectroscopy of the atomic D_1 line. *Physical Review C*, 18:2342–2354, 1978.

[119] Hiroki Nishibata. *Variety of nuclear structures in neutron-rich nuclei* ^{30}Mg *and* ^{31}Mg *investigated by spin-polarized* Na *beams*. PhD thesis, Osaka University, 2016.

[120] M. Shamsuzzoha Basunia. Nuclear data sheets for A = 28. *Nuclear Data Sheets*, 114(10):1189–1291, 2013.

[121] Noritaka Shimizu. Nuclear shell-model code for massive parallel computation, "KSHELL", 2013. arXiv:1310.5431.

[122] P. Himpe, G. Neyens, D. L. Balabanski, G. Bélier, J. M. Daugas, F. de Oliveira Santos, M. De Rydt, K. T. Flanagan, I. Matea, P. Morel, Yu. E. Penionzhkevich, L. Perrot, N. A. Smirnova, C. Stodel, J. C. Thomas, N. Vermeulen, D. T. Yordanov, Y. Utsuno, and T. Otsuka. g factor of the exotic $N = 21$ isotope ^{34}Al: probing the $N = 20$ and $N = 28$ shell gaps at the border of the "island of inversion". *Physics Letters B*, 658(5):203–208, 2008.

[123] Z. Y. Xu, H. Heylen, K. Asahi, F. Boulay, J. M. Daugas, R. P. de Groote, W. Gins, O. Kamalou, Á. Koszorús, M. Lykiardopoulou, T. J. Mertzimekis, G. Neyens, H. Nishibata, T. Otsuka, R. Orset, A. Poves, T. Sato, C. Stodel, J. C. Thomas, N. Tsunoda, Y. Utsuno, M. Vandebrouck, and X. F. Yang. Nuclear moments of the low-lying isomeric 1^+ state of ^{34}Al: Investigation on the neutron 1p1h excitation across $N = 20$ in the island of inversion. *Physics Letters B*, 782:619–626, 2018.

[124] R. Kanungo, C. Nociforo, A. Prochazka, Y. Utsuno, T. Aumann, D. Boutin, D. Cortina-Gil, B. Davids, M. Diakaki, F. Farinon, H. Geissel, R. Gernhäuser, J. Gerl, R. Janik, B. Jonson, B. Kindler, R. Knöbel, R. Krücken, M. Lantz, H. Lenske, Y. Litvinov, K. Mahata, P. Maierbeck, A. Musumarra, T. Nilsson, T. Otsuka, C. Perro, C. Scheidenberger, B. Sitar, P. Strmen, B. Sun, I. Szarka, I. Tanihata, H. Weick, and M. Winkler. Structure of ^{33}Mg sheds new light on the $N = 20$ island of inversion. *Physics Letters B*, 685(4):253–257, 2010.

[125] Yusuke Tsunoda, Takaharu Otsuka, Noritaka Shimizu, Michio Honma, and Yutaka Utsuno. Novel shape evolution in exotic ni isotopes and configuration-dependent shell structure. *Physical Review C*, 89:031301, 2014.

[126] T. Otsuka, M. Honma, T. Mizusaki, N. Shimizu, and Y. Utsuno. Monte carlo shell model for atomic nuclei. *Progress in Particle and Nuclear Physics*, 47(1):319–400, 2001.

Acknowledgments

I would like to show my appreciation to those who helped me along the way through my time as a PhD student at the University of Tokyo.

First of all, I would like to thank my supervisor, Prof. Nobuaki Imai, for his continuous support and encouragement throughout my PhD life at the Center for Nuclear Study. He gave me freedom to do anything that I was interested in, so I was able to fully enjoy my five years here. I am also thankful for his generosity, friendliness, and positive attitude that helped me greatly when I went astray. This will never be forgotten.

Prof. Kathrin Wimmer has been the supervisor of this thesis work. I am indebted to her for giving me the opportunity to work on the present data. It would have been impossible for me to complete my PhD without her support. I have been astonished by her wide knowledge of nuclear physics and expertise in experiment and theory as well. She also taught me many important things as a scientist, and I was particularly impressed by her critical thinking and attitude towards making things productive and efficient. She was willing to spare much time for discussions during her busy life, and when I lost my way she always guided me in the right direction. I am delighted to be able to work with such a great supervisor.

I would like to thank the members of the DONUTS group. I thank Prof. Shin'ichiro Michimasa for giving me a number of comments in our weekly meeting (and I owe him a professional soldering machine). I was impressed by his sincere attitude towards nuclear physics. Dr. Masanori Dozono has been my role model since my undergraduate days. I am indebted to him for his support during my PhD, especially for his help with preparing many applications for fundings. Without his assistance, I would not have been able to get any of them. I thank Ms. Rieko Tsunoda for her assistance in various experiments. She also brought her cheerfulness to our lab. I hope I can work with these people again in the near future.

I am also grateful to the members of the NUSPEQ group. I am thankful to Prof. Susumu Shimoura. He is always open-minded and willing to share his expertise. It seems he would know everything about nuclear physics, so I was always overwhelmed by his knowledge. Many thanks to Prof. Shinsuke Ota, whom I regard as a true expert in nuclear physics experiments. He has outstanding skills in both hardware and software. Since my first year at CNS, he has guided me through data acquisition systems and electronics. I would like to thank my senior colleagues, Mr. Motonobu Takaki, Dr. Rin Yokoyama, and Dr. Motoki Kobayashi. It was very delightful to work with great people like you.

During my PhD, I met so many wonderful people. I would like to thank Mr. Shoichiro Masuoka and Mr. Keita Kawata for their friendship, funny stories, and fond memories. We participated in many experiments together. The experiements were sometimes enjoyable but mostly tough. They are truly my comrades. I thank Dr. Daisuke Suzuki, Mr. Shumpei Koyama, Mr. Takeshi Saito, and Prof. Megumi Niikura. The experience at GANIL with them will remain one of my fondest memories. I thank Mr. Shusuke Takada, who used to work at RIKEN. He is

my senior colleague and at the same time one of my oldest friends. I was very fortunate to have a friend with whom I can share my feelings.

Many thanks to my roommates. I am grateful to Mr. Hiroshi Tokieda for his kindness and offering me lots of practical advice. Thanks go to Dr. Beliuskina Olga, a former member of the DONUTS group. She was a kind of English teacher during my first year at CNS. Thanks also go to Dr. Daiki Sekihata for lending me a special keyboard. I am typing this very text with his keyboard.

I thank the collaborators of the experiment e12003, whose contribution led to its success. I acknowledge the support from the theoreticians Prof. Noritaka Shimizu, Dr. Naofumi Tsunoda, Prof. Yutaka Utsuno, Prof. Nobuo Hinohara, and Prof. Ikuko Hamamoto for the valuable discussions. I would like to thank Dr. Hiroki Nishibata, who has also been studying ^{30}Mg, for sparing much time for the discussions.

This thesis work was supported by the ALPS program of the University of Tokyo and the JSPS fellowship. Prof. Hiroyoshi Sakurai was my advisor in the ALPS program. I would like to thank him for his encouragement. I thank the secretaries, Ms. Yukino Kishi, Mrs. Ikuko Yamamoto, and Mrs. Takako Endo, for their support during my PhD.

I thank the members of the thesis committee, Prof. Masaya Ishino, Prof. Tadashi Koseki, Prof. Kenji Fukushima, Prof. Kyoichiro Ozawa, and Prof. Hidetoshi Yamaguchi. With their comments and criticism, this thesis was improved very much.

I unfortunately must ommit many people from my list of acknowledgments, but I am grateful to those unnamed for their encouragement, assistance, teaching, and friendship. Lastly, I would like to express gratitude to my family for their understanding and long-standing support.